TOWARDS UNDERSTANDING DARK MATTER STRUCTURES

by

KASPER BORELLO SCHMIDT

MASTER THESIS
at

Dark Cosmology Centre

Niels Bohr Institute
University of Copenhagen
June 27th 2008

SUPERVISOR:

STEEN H. HANSEN
Dark Cosmology Center
University of Copenhagen

Acknowledgements

Kasper Borello Schmidt
kschmidt@dark-cosmology.dk

Abstract

One of the biggest mysteries in modern astrophysics is the appearance and characteristics of the peculiar dark matter (DM) structures. Several relations for DM structures have been identified and are generally accepted as fundamental. Assuming that these relations are valid we will with this work contribute to the continuing unravel of the 'DM mystery'.

Recent numerical simulations show that the angular momentum of DM structures is quite small. We suggest a generalized collisionless Jeans equation (CJE) including a new rotational term, appearing when adding a small bulk rotation to a DM system. This is done under the assumption of a reasonable parameterization of the distortion of the DM particle ensemble velocity distribution function. Conjecturing that the (new) rotational supplement to the Jeans equation is proportional to the (old) mass term, we find analytically a clear connection, which we compare with recent high resolution DM structure simulations. This new suggested relation is shown to be in good agreement with these simulations. We also present a new relation between the velocity anisotropy and the rotation, which is shown to be in fair agreement with numerical findings. The spin parameter arising from the new rotation term in the CJE is shown to increase as a function of radius, in agreement with recent studies.

Furthermore we derive (another) form of the CJE, assuming a general phase space density to be a power law in radius. We write a Monte Carlo code which analyzes recent high resolution simulations to find the most probable values of the unknowns in this new CJE. Using the results from this we show how the form of the general phase space density is closely related to the size of the exponent in the assumed radial dependence. We quantify this via a set of linear relations which are able to reproduce the results of Dehnen & McLaughlin (2005) as a special example. Furthermore these relations are able to predict the radial dependence for various types of phase space densities and suggest that no generally preferred value of the different optimized parameters exist for DM structures. Finally we quantify the outer density slopes in DM structures using this new CJE. We are not able to quantify the inner slopes because of uncertainty in the optimization of some of the unknown parameters.

Contents

List of Tables

List of Figures

1   Introduction

People have always been curious and eager to explain everything around them. Indeed the universe and astronomy in general have always fascinated humanity. We have for quite a few centuries tried to describe and understand the world that surrounds us. In much the same way, the work presented in this thesis, is a small peek into unknown terrain, the 'terrain of dark matter structures'. For the last couple of decades the astrophysical society has been on the hunt for the peculiar dark matter (DM) particles, and has been trying to understand how the DM behaves. We have come quite a long way, but the DM is still one of the biggest mysteries in modern astrophysics. DM has through the years been debated quite a lot, and questions like

  a) what is it made of?

  b) how do we measure it?

  c) what are its characteristics?

  d) etc.

have been put forth. In the next few pages I will give a very brief overview of some of the answers to these questions, i.e., things which are known and generally accepted as the truth today, about the behavior and characteristics of the peculiar DM structures of the universe.[1] After introducing the DM in general I will give my contribution to the unravel of the DM mysteries, by describing and discussing my work during the last 12 months. This work will mainly concentrate on the theoretical description of the DM structures. By investigating how DM structures behave when angular momentum is added, and by investigating the 'main equation' of DM structures, the Jeans equation, I hope to contribute to the understanding and knowledge about DM structures as an astrophysical phenomenon.

1.1   Dark Matter Constituents and the CDM

In general DM can be divided into three different kinds of DM; the non-luminous massive objects, the hot dark matter (HDM) and the cold dark matter (CDM). The non-luminous matter are objects like black holes, white dwarfs, neutron stars, planets etc. The HDM is in principle ordinary neutrinos, which decoupled from the early universe when they were still relativistic (i.e., hot). The CDM is particles that decoupled as non-relativistic (i.e., cold) and were therefore able to preserve the density fluctuations of the early universe on all scales.

  The work presented here is based on the CDM picture and we will therefore describe this in a bit more detail. The CDM consists of various kinds of exotic particles referred to as weakly interacting massive particles (WIMPs). CDM particles are often referred to as collisionless particles. This is simply because by nature they

---

[1]For a more detailed description of DM in general please refer to e.g. Binney & Tremaine (1987), Kolb & Turner (1994) and Longair (1998).

don't interact with 'ordinary' luminous matter. It has been suggested, however, that annihilation processes between WIMPs might be observable. People have tried to build detectors that can observe these events for the last decade or so, and still are.

When the CDM particles decoupled from the early universe they were, as mentioned, non-relativistic. Therefore free streaming was not an issue (Longair, 1998) and the CDM particle density perturbations were not destroyed. Since then DM became dynamically dominant and in the epochs after decoupling the density perturbations steadily grew bigger. At some point these perturbations were sufficiently large to start collapsing under their own gravity, and started forming the DM landscape we see traces of today. The baryons fell into this DM potential landscape and grew to minor structures, which later combined to galaxies and clusters as we know them. Thus the DM structures, as well as the baryonic structures, follow the so-called bottom-up structure formation scheme, where small structures formed first and then later developed/merged into larger structures.

1.2   Indirect Observations

Part of the answer to the question of how to measure the DM is the use of indirect measurements/observations. The most famous, which was also one of the first real evidences for the existence of the DM is the galaxy rotation curve. In the quest for estimating the mean density of the Universe, people figured out that if they were able to measure the mean mass of a galaxy, and combine this with the number of galaxies in the Universe, they would get a mean density using the present Hubble volume. To estimate the mass of the galaxies the easiest way, people used Kepler's third law. This required knowledge about the rotation curve of the galaxies. Achieving this people realized that the rotation curves didn't behave as expected. Where they were suppose to fall off as the amount of luminous matter decreased in the outskirts of the galaxies, they didn't. This indicated that the rotation was supported by more than the luminous matter in the outer parts of the galaxies. Hence the phenomenon of non-luminous, i.e., dark matter was established. Today the rotation curve method has been shown to be a quite strong estimate of the density profiles and DM particle distributions in DM halos.

Another way of measuring the DM (indirectly) is by analyzing and estimating its gravitational effects on, and interactions with, observable baryonic matter. This can be done in various ways. Probably the most convincing way is through gravitational lensing. Several studies have been performed to estimate the mass content of galaxies, clusters and other lensing objects. By comparing lensing models estimating the density contours with the observable luminous matter, it becomes clear that in order to create the observed lensed images much more mass than just the luminous is needed. This 'missing' mass can't be explained by dust and gas clouds and lensing is therefore another powerful tool for estimating, 'measuring' and arguing for the existence of DM.

One of the most obvious and interesting places to look for dark matter both indirectly and directly (trying to get a glimpse of the observable parts/leftovers from

WIMP annihilation processes) is the Bullet Cluster where DM has been separated from the baryonic matter through the merging of two clusters (e.g. Markevitch et al. (2008) and Randall et al. (2008)).

1.3   The Characteristics of Dark Matter Structures

Regarding the characteristics of DM and DM structures, much is still to be learned. Nevertheless we have today unraveled some of the DM mystery, and are still increasing our knowledge. One of the most basic and important characteristics of DM structures is their collisionless nature. Since DM particles by nature are themselves collisionless, the DM structures are also collisionless. Again the Bullet cluster is one of the best examples of this property (which is the opposite for ordinary baryonic matter). The Bullet cluster is as mentioned the result of the merging of two clusters. From lensing one can show that the DM halos are intact and have passed right through one-another, whereas the baryonic matter has clearly been affected by the violent collision of the structures. That DM structures are collisionless enables a relatively simple theoretical description of them. In general DM structures consist of an ensemble of particles bound together by their mutual gravity. This ensemble can be treated purely statistically, and making assumptions about the ensemble appearance and taking advantage of its collisionless nature gives a good theoretical framework when dealing with DM structures. This approach is described in more detail in Sec. 2.1.

Furthermore people have through the years come up with various relations between the characteristic parameters of DM structures. Among these are a relation between the density ρ and the radius r, a suggested relation between the phase space density of DM structures and their radial extent, a correlation between the density slope, γ, and the velocity anisotropy, β, and last but not least people have observed a relation between the specific angular momentum, i.e., the rotation of DM structures and their masses. I will introduce these basic DM structure relations in the following subsections.

1.3.1   The Dark Matter Density Profile $\rho(r)$

One of the first major relations discovered between DM structure parameters, is the rather strong relation between the density and the radius of the structure. In general the density profile of a DM structure is a power law in radius, such that

$$\rho \sim r^{-\gamma(r)} \qquad \text{or} \qquad \gamma(r) = -\frac{d\ln\rho}{d\ln r} \qquad (1.1)$$

where γ is some function depending on r. It has been shown that the profile is steepest in the outer regions where γ seems to be larger than the density slope of an isothermal structure, i.e., $\gamma = 2$, whereas in the inner region DM structures become shallower and have $\gamma < 2$. Since this relation was realized people have tried to come up with universal forms of the radius dependency in the density slope. The

two most famous of these are the Hernquist model (Hernquist, 1990) and the NFW profile (Navarro et al., 1996, 1997). Both of these density profiles can be written in the form

$$\rho(r) \propto \frac{1}{r \left(1 - \frac{r}{r_s}\right)^m} \tag{1.2}$$

where r_s is some scale radius of the structure. For $m = 3$ one has the Hernquist profile, and for $m = 2$ the equation turns into the NFW profile. These relations have been compared with simulated data several times through the years. In general Eq. (1.2) is a good approximation of the density profile of DM structures (Moore et al., 1999) even though the particular examples of the Hernquist and NFW profile are known to come short when compared to recent simulations.

1.3.2   The Phase Space Density Power Law

As a supplement to the relation between the ordinary density and the radius people use a relation between the radius and the so-called phase space density. The phase space density of (simulated) DM structures has been recognized to behave as a (strict) power law in radius over almost 2.5 orders of magnitude in mass (Taylor & Navarro, 2001). The phase space density-radius relation, which is often written as

$$\frac{\rho}{\sigma^3} \propto r^{-\alpha} \tag{1.3}$$

is therefore well suited for comparison when investigating DM structures of very different sizes. Above σ refers to the velocity dispersion of the given DM structure, i.e., the velocity dispersion of the DM particle ensemble. Compared to the density relation presented in the previous subsection, α is here independent on the radius r. People have also used phase space like relations when describing the fundamental behavior of DM structures trying to understand the underlying physics. Such approaches are e.g. Hansen (2004), Austin et al. (2005) and Dehnen & McLaughlin (2005). The origin of the phase space density relation has, however, not yet been fully understood. The Dehnen & McLaughlin (2005) paper has served as an inspiration for the evaluation of the Jeans equation part of the thesis, and will be described in more detail in Sec. 3.1.

1.3.3   Density Slope and Velocity Anisotropy

Furthermore a relation between the density slope γ and the velocity anisotropy β of the DM structures has been suggested. The velocity anisotropy is defined as (Binney & Tremaine, 1987)

$$\beta = 1 - \frac{\sigma_\theta^2 + \sigma_\phi^2}{2\sigma_r^2} \tag{1.4}$$

where σ is the velocity dispersion. As argued by Dehnen & McLaughlin (2005) the basic equation describing DM structures naturally suggests a linear relation between

β and γ (see Sec. 3.1), i.e.,

$$\gamma \sim \beta \; . \tag{1.5}$$

Hansen & Moore (2006) furthermore show how such a relation 'magically pops out' when comparing the velocity anisotropy and density slope in completely different simulated structures. This result is astonishingly well established because of its selection by the underlying equations of DM structures and the agreement with simulations of various kinds.

1.3.4 Angular Momentum

In general the origin of the angular momentum of DM structures is not agreed upon. Through the years there has been a debate on whether the angular momentum was generated by tidal torque effects or by the merging of various structures. The first scenario, i.e., that angular momentum is a consequence of the linear tidal torque between small density fluctuations in the early universe when the galaxies were originally formed, is supported by for instance D'Onghia & Navarro (2007). The other scenario states that it is the merging history of the structure, i.e., the number and characteristics of mergers between protogalaxies forming the final structure, which is responsible for the total angular momentum. This scenario is supported by for instance Vitvitska et al. (2002). Other people, such as Maller et al. (2002), compare the two scenarios to illustrate their pros et cons, and hopefully move the discussion a step closer to a solution, but none has been found so far.

On the other hand people widely agree on *how to describe* the angular momentum, when it has been established. When dealing with the rotation of DM structures the so-called spin parameter, λ , is very often used as a common reference point, which enables authors to compare their results and work with those of other people. The spin parameter was introduced by Peebles (1969). He defined it as

$$\lambda \equiv \frac{L|E|^{1/2}}{GM^{5/2}} \; . \tag{1.6}$$

Here L, E, M and G are the angular momentum, the binding energy of the system, the total mass of the system and the Newtonian gravitational constant respectively. In this way the spin parameter roughly corresponds to the ratio between the overall angular momentum of the object and the angular momentum this object needs to sustain rotational support

More recently Bullock et al. (2001) have introduced a new form of the spin parameter, which they refer to as

$$\lambda' = \frac{J}{\sqrt{2GM^3 r}} \; . \tag{1.7}$$

We will use this form when comparing our results with the work of others via the spin parameter in Sec. 2.6.3. When looking at Eq. (1.6) and (1.7) it's obvious that one of the reasons why most people are very fond of using the spin parameter in

their work, is its close connection to important factors of (DM) structures, like the mass, energy, radius and of course rotation of the system. Another thing that makes the spin parameter rather handy to work with is the fact that λ has the ability of being (almost) constant in time, under the assumptions that the system is more or less isolated and that there is no dissipation present (assuring that E and L are both conserved). The spin parameter is of the order 0.05 (Vitvitska et al. (2002)), which means that in general the systematic rotation in DM structures is small and that the rotational support is negligible.

Bullock et al. (2001) use their definition of the spin parameter to investigate the relation between angular momentum and the mass of simulated structures. They found a relation on the form

$$j(M) \propto M^s \tag{1.8}$$

with $s = 1.3 \pm 0.3$, between the specific angular momentum, j, and the mass of the CDM structures they were considering. We will in Sec. 2 show that our approach can replicate the results of Bullock et al. (2001) under the assumption that the azimuthal velocity dispersion is constant in radius.

2 Rotation of DM Structures

In this section, the rotation of dark matter structures will be investigated from a mainly theoretical point of view. To start with, the general scheme of angular momentum of DM structures, including a derivation of the collisionless Jeans equation, will be described to put the work into context. We will then argue that through a distortion of the DM particle ensemble velocity distribution function, an added bulk rotation results in a more or less linear perturbation of the velocity dispersion in the rotational direction. Combining this with the usual Jeans equation gives a new general Jeans equation containing a term concerning the added rotation. We investigate this new general Jeans equation by comparing the suggested rotational term with recent high resolution simulations of galaxies and clusters of galaxies. Conjecturing that the (new) subdominant rotation term is proportional to the (old) mass term, we see a clear connection when our suggested fundamental relations are compared to the simulations. In a similar way we also find that a relation between the rotation and the velocity anisotropy β of the system seems to agree with simulations.

We also suggest a new form of the spin parameter introduced in Sec. 1.3.4 containing the subdominant rotation term. This new spin parameter is shown to grow as a function of structure radius and be (more or less) constant taken at the virial mass. Both these results agree with recent studies of DM structure angular momentum.

2.1 Theoretical Framework

In general nothing ensures that a given particle ensemble in a DM halo is spherically distributed. Nevertheless a spherical distribution of particles makes the approach of describing the structure theoretically relatively simple and much easier, than if we were dealing with a (more correct) triaxial picture. Luckily the spherical picture is actually quite close to the true (triaxial/prolate) picture. In general the axial ratio of DM structures is believed to be at least of the order 0.5. For instance Altay et al. (2006) and Lee et al. (2005) have axial ratios of the order 0.55. Fig. 16 in Algood et al. (2006) sums up various recent studies of the sphericity of DM structures, and shows that the axis ratio is between 0.5 and 0.9 for all of the shown analyses. Thus as a first approach to get new insight into the nature of the rotation of DM structures, assuming a spherically distributed particle ensemble is justifiable to some extent. We will therefore assume this in order to be able to investigate the problem analytically. Furthermore we will assume that the DM halo is relaxed and in dynamical equilibrium, i.e., we want an ensemble from which no DM particles can escape and which is not affected by the surroundings.

If we then use the velocity distribution function f to describe the ensemble we know from statistics that for collisionless matter like DM, $\frac{df}{dt} = 0$. This is the essence of the general collisionless Boltzmann equation (CBE). The CBE basically describes how the statistical distribution of particles behaves in phase space, i.e., how the distribution function f changes in time and in position and momentum space. That the equation is collisionless indicates that we have neither sources nor sinks in

position and momentum space. Thus DM particles can't suddenly disappear/appear by for instance annihilation processes, and discontinuities in the particle trajectories are forbidden, which could for instance happen if two particles collided and therefore suddenly changed directions.

If the particle ensemble is assumed to be spherically distributed, as in our case, and since the DM particles are collisionless, we have the *spherical* CBE

$$
\begin{aligned}
0 \;=\;& \frac{\partial f}{\partial t} + v_r \frac{\partial f}{\partial r} + \frac{v_\theta}{r} \frac{\partial f}{\partial \theta} + \frac{v_\phi}{r \sin\theta} \frac{\partial f}{\partial \phi} + \left(\frac{v_\theta^2 + v_\phi^2}{r} - \frac{\partial \Phi}{\partial r} \right) \frac{\partial f}{\partial v_r} \\
&+ \frac{1}{r} \left(v_\phi^2 \cot\theta - v_r v_\theta - \frac{\partial \Phi}{\partial \theta} \right) \frac{\partial f}{\partial v_\theta} \\
&- \frac{1}{r} \left(v_\phi(v_r + v_\theta \cot\theta) + \frac{1}{\sin\theta} \frac{\partial \Phi}{\partial \phi} \right) \frac{\partial f}{\partial v_\phi} \;.
\end{aligned}
\tag{2.1}
$$

Here Φ is the gravitational potential of the structure, and v_r, v_θ and v_ϕ are the DM particle velocities in phase space. This equation is used when deriving the single most important equation when dealing with the behavior and nature of DM structures in general, and DM halos in particular, namely the Jeans equation. We will derive the Jeans equation in the following subsection. For the exact steps in getting the spherical CBE in Eq. (2.1), please refer to App. A.

2.1.1   Deriving The Jeans Equation

In this section we will derive the general spherical collisionless Jeans equation for the DM particle ensemble. This is the single most important equation when dealing with DM structures. The derivation is simply done by taking the first (radial) moment of the spherical CBE, Eq. (2.1), under the assumptions that the gravitational potential Φ only varies in the radial direction, that the thermal velocities are independent of each other, that the system is in a steady state and that there is no bulk (rotational) motion.

The first (radial) moment of the CBE is given by

$$
\int \text{CBE} \cdot v_r \; d^3\overline{v} \;.
\tag{2.2}
$$

Using the assumption that $\frac{\partial \Phi}{\partial \theta} = 0$ and $\frac{\partial \Phi}{\partial \phi} = 0$ and by plugging in the CBE, this gives

$$
\begin{aligned}
0 \;=\;& \frac{\partial}{\partial t} \int v_r f d^3\overline{v} + \frac{\partial}{\partial r} \int v_r^2 f d^3\overline{v} + \frac{1}{r} \frac{\partial}{\partial \theta} \int v_r v_\theta f d^3\overline{v} \\
&+ \frac{1}{r \sin\theta} \frac{\partial}{\partial \phi} \int v_\phi v_r f d^3\overline{v} + \int \left(\frac{v_r v_\theta^2}{r} \frac{\partial f}{\partial v_r} + \frac{v_r v_\phi^2}{r} \frac{\partial f}{\partial v_r} - v_r \frac{\partial \Phi}{\partial r} \frac{\partial f}{\partial v_r} \right) d^3\overline{v} \\
&+ \frac{\cot\theta}{r} \int v_r v_\phi^2 \frac{\partial f}{\partial v_\theta} d^3\overline{v} - \frac{1}{r} \int v_r^2 v_\theta \frac{\partial f}{\partial v_\theta} d^3\overline{v} \\
&- \frac{1}{r} \int v_\phi v_r^2 \frac{\partial f}{\partial v_\phi} d^3\overline{v} - \frac{\cot\theta}{r} \int v_r v_\theta v_\phi \frac{\partial f}{\partial v_\phi} d^3\overline{v}
\end{aligned}
\tag{2.3}
$$

Here we have also used that the partial derivatives with respect to the different components, r, θ, ϕ and t can be taken outside the integrals $\int d^3\overline{v}$. This is justified since these components are all velocity independent in phase space. Introducing the density of the system $\rho = \int f d^3\overline{v}$ and the mean particle velocity $\langle v_i \rangle = \frac{1}{\rho}\int f v_i d^3\overline{v}$, where i represents the three spherical components r, θ and ϕ, we can rewrite the above equation into

$$
\begin{aligned}
0 = {} & \frac{\partial}{\partial t}\langle v_r \rangle \rho + \frac{\partial}{\partial r}\langle v_r^2 \rangle \rho + \frac{1}{r}\frac{\partial}{\partial \theta}\langle v_r v_\phi \rangle \rho + \frac{1}{r\sin\theta}\frac{\partial}{\partial \phi}\langle v_r v_\phi \rangle \rho \\
& + \frac{1}{r}\int v_r v_\theta^2 \frac{\partial f}{\partial v_r}d^3\overline{v} + \frac{1}{r}\int v_r v_\phi^2 \frac{\partial f}{\partial v_r}d^3\overline{v} - \frac{\partial \Phi}{\partial r}\int v_r \frac{\partial f}{\partial v_r}d^3\overline{v} \\
& + \frac{\cot\theta}{r}\left[\int v_r v_\phi^2 \frac{\partial f}{\partial v_\theta}d^3\overline{v} - \int v_r v_\phi v_\theta \frac{\partial f}{\partial v_\phi}d^3\overline{v}\right] \\
& - \frac{1}{r}\left[\int v_r^2 v_\theta \frac{\partial f}{\partial v_\theta}d^3\overline{v} + \int v_\phi v_r^2 \frac{\partial f}{\partial v_\theta}d^3\overline{v}\right] .
\end{aligned}
\tag{2.4}
$$

Now, using integration by parts and the above definition for the mean velocity, gives

$$
\begin{aligned}
\int v_i v_j v_k \frac{\partial f}{\partial v_i}d^3\overline{v} &= \int v_j dv_j \int v_k dv_k \int v_i \frac{\partial f}{\partial v_i}dv_i \\
&= \int v_j dv_j \int v_k dv_k \left([v_i f]_{-v_{i,\max}}^{+v_{i,\max}} - \int f dv_i\right) \\
&= \int v_j dv_j \int v_k dv_k [v_i f]_{-v_{i,\max}}^{+v_{i,\max}} - \rho\langle v_j v_k \rangle .
\end{aligned}
\tag{2.5}
$$

Here i, j and k represents the spherical components r, θ and ϕ. The $\pm v_{i,\max}$ limits are some maximum/minimum velocity. Since the velocity distribution function for the DM particle ensemble goes to zero for large velocities we then have

$$
\int v_i v_j v_k \frac{\partial f}{\partial v_i}d^3\overline{v} = -\rho\langle v_j v_k \rangle .
\tag{2.6}
$$

This enables us to evaluate the integrals containing three velocity factors in Eq. (2.4) one by one.

$$
\begin{aligned}
\frac{1}{r}\int v_r v_\theta^2 \frac{\partial f}{\partial v_r}d^3\overline{v} &= -\frac{\rho}{r}\langle v_\theta^2 \rangle \\
\frac{1}{r}\int v_r v_\phi^2 \frac{\partial f}{\partial v_r}d^3\overline{v} &= -\frac{\rho}{r}\langle v_\phi^2 \rangle \\
\frac{\cot\theta}{r}\int v_r v_\phi^2 \frac{\partial f}{\partial v_\theta}d^3\overline{v} &= \frac{\cot\theta}{r}\int v_r dv_r \int v_\phi^2 dv_\phi \int \frac{\partial f}{\partial v_\theta}dv_\theta \\
&= 0 \quad \text{since} \int df = 0
\end{aligned}
$$

$$
\tag{2.7}
$$

$$\frac{\cot\theta}{r}\int v_r v_\phi v_\theta \frac{\partial f}{\partial v_\phi}d^3\overline{v} = -\frac{\cot\theta}{r}\rho\langle v_r v_\theta\rangle$$

$$\frac{1}{r}\int v_r^2 v_\theta \frac{\partial f}{\partial v_\theta}d^3\overline{v} = -\frac{1}{r}\rho\langle v_r^2\rangle$$

$$\frac{1}{r}\int v_\phi v_r^2 \frac{\partial f}{\partial v_\phi}d^3\overline{v} = -\frac{1}{r}\rho\langle v_r^2\rangle .$$

These expressions can be plugged back into Eq. (2.4), giving

$$
\begin{aligned}
0 = & \frac{\partial}{\partial t}\rho\langle v_r\rangle + \frac{\partial}{\partial r}\rho\langle v_r^2\rangle + \frac{1}{r}\frac{\partial}{\partial\theta}\langle v_r v_\theta\rangle\rho \\
& + \frac{1}{r\sin\theta}\frac{\partial}{\partial\phi}\langle v_\phi v_r\rangle\rho - \frac{\rho}{r}\langle v_\theta^2\rangle - \frac{\rho}{r}\langle v_\phi^2\rangle + \rho\frac{\partial\Phi}{\partial r} \\
& + 0 + \frac{\cot\theta}{r}\rho\langle v_r v_\theta\rangle + \frac{\rho}{r}\langle v_r^2\rangle + \frac{\rho}{r}\langle v_r^2\rangle .
\end{aligned}
\tag{2.8}
$$

The three spherical velocities v_r, v_θ and v_ϕ are independent, which can be expressed as $\langle v_i v_j\rangle = \delta_{ij}\langle v_i^2\rangle$ with $\delta_{ij} = 0$ for $i \neq j$ and 1 for $i = j$. Furthermore we are considering a steady state ensemble, i.e., any variation in time is 0. Taking all of this into account and realizing that $\langle v_i^2\rangle$ is just the velocity dispersion (which we will for simplicity write as σ_i^2) we end up with the spherical collisionless Jeans equation for the steady state (henceforth CJE) for a given potential Φ

$$\frac{\partial\rho\sigma_r^2}{\partial r} + \frac{\rho}{r}\left(2\sigma_r^2 - \sigma_\theta^2 - \sigma_\phi^2\right) = -\rho\frac{\partial\Phi}{\partial r} . \tag{2.9}$$

As mentioned earlier the given potential is in our framework simply the gravitational potential arising from the mutual gravitational attraction between the DM particles. The spherical Poisson equation can be written so it relates the potential and the density,

$$4\pi G\rho = \nabla^2\Phi = \frac{1}{r^2}\frac{\partial}{\partial r}r^2\frac{\partial\Phi}{\partial r} . \tag{2.10}$$

Here we have again used the assumption that $\frac{\partial\Phi}{\partial\theta} = 0$ and $\frac{\partial\Phi}{\partial\phi} = 0$ to get the last equality. Combining Eq. (2.9) with this form of Poisson's equation (and changing ∂ to d) we get

$$\frac{d}{dr}r^2\left(-\frac{1}{\rho}\frac{d\rho\sigma_r^2}{dr} - \frac{1}{r}\left(2\sigma_r^2 - \sigma_\theta^2 - \sigma_\phi^2\right)\right) = 4\pi G\rho r^2 \tag{2.11}$$

which is another way of writing the CJE. Integrating Eq. (2.11) to obtain the total mass on the RHS and using that $d\ln z = \frac{dz}{z}$ gives yet another form of the CJE, namely

$$\boxed{\sigma_r^2\frac{d\ln(\rho\sigma_r^2)}{d\ln r} + \left(2\sigma_r^2 - \sigma_\theta^2 - \sigma_\phi^2\right) = -\frac{GM}{r} .} \tag{2.12}$$

Here σ_θ^2, σ_r^2 and σ_ϕ^2 are as mentioned the velocity dispersions, ρ is the density of the DM structure, M is the total mass within a given radius r, and G is Newtons

gravitational constant. Hence this equation relates some of the most important factors when dealing with collisionless matter. We have now established a theoretical framework of DM structures, which can be used when explaining the effects on a DM system when adding a small bulk rotation as we will do in the following section(s).

2.2   Adding Rotation

Now that the theoretical framework has been established, and we have derived the relevant equations we are able to investigate the angular momentum of the DM structure in general. To do that we add a small bulk rotation $v_{\rm rot}(r)$ to the azimuthal thermal velocity v_ϕ. So instead of an all-thermal velocity, we make it a combination of both thermal and bulk motion. We explicitly write the velocity in the following way

$$v_\phi(v_{\rm rot} = 0) \rightarrow \tilde{v}_\phi(v_{\rm rot}) \ . \tag{2.13}$$

The obvious way to add rotation to a system is by giving every particle an initial kick, i.e., assuming $\tilde{v}_\phi = v_\phi + v_{\rm rot}$. Giving such an initial kick to every particle would simply result in a shift of the velocity distribution function (DF) of the DM particles, corresponding to the amount of rotation added. Since we assume that our system is in dynamical equilibrium this is not a good approach. It will enable the most energetic particles, i.e., particles close to the system escape velocity to escape the gravitational potential created by the ensemble. A system where particles are able to escape is definitely not in equilibrium. We must therefore come up with another way to implement the added rotation into the DF of the DM particle ensemble, f. The idea is to distort the DF into a new DF, $\tilde{f}$, in a suitable way, such that the structure is still in equilibrium. As shown in Sec. 2.6 such a distortion seems to agree well with high resolution simulations. We will therefore now argue for such a distortion and how it can be added to the theoretical framework just established.

Expressing the distortion by $f - \tilde{f}$ and assuming that the difference in the two DFs is small and governed by the added size of the rotation, we have

$$f - \tilde{f} \propto P(v_{\rm rot})f \ . \tag{2.14}$$

Here P is some unknown function depending on the added bulk rotation. Thus for a certain form of P we here make sure that the dynamical equilibrium is maintained. As mentioned above, simply shifting the DF by $v_{\rm rot}$ while leaving the shape of the DF virtually unchanged would allow energetic particles to escape. Adding rotation will in principle affect all particles equally. It's not very likely that this will make a low velocity particle escape the system, hence the needed distortion of the DF for such particles is rather small. On the other hand the probability that the rotation might enable the most energetic particles to escape is much larger. We therefore need the distortion to be relatively stronger for higher velocities. To fulfill this demand we simply multiply Eq. (2.14) with a v_ϕ-dependent function, called Q (where Q is 'strongest' for large velocities), such that

$$f - \tilde{f} \propto P(v_{\rm rot})\, Q(v_\phi)f \ . \tag{2.15}$$

In general we must have that the overall density of the system is not affected by the added bulk rotation, i.e., $\rho = \tilde{\rho}$. The density is statistically defined as

$$\tilde{\rho} = \int \tilde{f} \, d^3v \;\; = \;\; \int f - (f - \tilde{f}) d^3v = \rho - \int (f - \tilde{f}) \, d^3v \; . \qquad (2.16)$$

Ensuring that the density is unaffected by the added rotation is easily done by restricting $(f - \tilde{f})$ to be an odd function when integrated over the velocities, such that the last integral vanishes. Hence we have that Q must be an odd function in v_ϕ. Assuming that the dependence of v_ϕ in Q is a simple power law enables us to write the distortion of the DF like

$$f - \tilde{f} = \xi P(v_{\rm rot}) \; \left(\frac{v_\phi}{\sqrt{\sigma_\phi^2}} \right)^\gamma f \; . \qquad (2.17)$$

Here ξ and γ are some unknown positive constants, where γ is restricted to the values $2n + 1$ for $n = 0, 1, 2, \ldots$ to preserve the density. Fractional powers would result in a complex result since negative values of v_ϕ are allowed, and can therefore not be used. The v_ϕ part of this form will in principle give problems for $v_\phi \to \infty$, causing the distortion of the DF to become infinite and hence $\tilde{f}$ to become negative. But since $\tilde{f}(v_\phi)$ is nearly zero for $v_\phi \sim \pm 4\sqrt{\sigma_\phi^2}$, this is not a practical problem. However, for a more formal derivation one naturally cannot allow the new DF $\tilde{f}$ to become negative, and must take care of this. But as a first approach this defect can (and will) be ignored.

In principle the suggested distortion of the DF in Eq. (2.17) can be tested with high resolution N-body simulations by considering the two tangential velocity DFs and simply looking at the differences between the velocity DF in the directions parallel and perpendicular to the direction in which the rotation has been added, i.e., perpendicular and parallel to the angular momentum vector of the system. Such measurements might be difficult since the relevant contours (in potential energy) are not perfectly spherical, and the definition of what is radial and tangential is debatable. Nevertheless we will in Sec. 2.4 look for the suggested distortion of the DF in a 'real' high resolution galaxy simulation containing gas, stars, DM, etc., and as mentioned it seems that a distortion of the DF is indeed present in the simulation.

We have now quantified the distortion of the DF. The goal is to insert this distortion into the Jeans equation (Eq. (2.12)) via the azimuthal velocity dispersion σ_ϕ^2. Before perturbing the velocity we have by definition that the velocity dispersion for that system is given by

$$\sigma_\phi^2 = \frac{1}{\rho} \int f \left(v_\phi - \langle v_\phi \rangle \right)^2 \, d^3v = \frac{1}{\rho} \int f v_\phi^2 \, d^3v \qquad (2.18)$$

since $\langle v_\phi \rangle = 0$. By definition the velocity dispersion is the integral over the DF multiplied with the difference between the individual particle velocities and the mean velocity of the system. Since the mean velocity after adding rotation becomes equal

to the added rotation itself, the new perturbed velocity dispersion must take the form

$$\tilde{\sigma}_\phi^2 = \frac{1}{\rho} \int \tilde{f} \left(v_\phi - v_{\text{rot}}\right)^2 \, d^3v \; . \tag{2.19}$$

Combining this expression for the velocity dispersion after adding the small bulk rotation with the fact that $\tilde{f} = f - (f - \tilde{f})$ gives

$$\tilde{\sigma}_\phi^2 = \frac{1}{\rho} \int f \left(v_\phi^2 + v_{\text{rot}}^2 - 2v_{\text{rot}}v_\phi\right) \, d^3v - \frac{1}{\rho} \int (f - \tilde{f}) \left(v_\phi^2 + v_{\text{rot}}^2 - 2v_{\text{rot}}v_\phi\right) \, d^3v \tag{2.20}$$

Since $\int f d^3v = \rho \neq 0$, the DF f is by definition an even function in velocity space, and since $(f - \tilde{f})$ is odd to conserve the density, the only non vanishing integrals in the above expression are

$$\tilde{\sigma}_\phi^2 = \frac{1}{\rho} \int f v_\phi^2 \, d^3v + \frac{v_{\text{rot}}^2}{\rho} \int f \, d^3v + \frac{2v_{\text{rot}}}{\rho} \int (f - \tilde{f}) v_\phi \, d^3v \tag{2.21}$$

Since it is known from numerical cosmological simulations that the rotational energy is less than a few percent of the thermal energy (Bullock et al., 2001), i.e., $v_{\text{rot}}^2 \ll \sigma_\phi^2$ it is justified to ignore the higher order terms in v_{rot}. This combined with Eq. (2.18) implies that

$$\tilde{\sigma}_\phi^2 \approx \sigma_\phi^2 + \frac{2v_{\text{rot}}}{\rho} \int (f - \tilde{f}) v_\phi \, d^3v \tag{2.22}$$

We see that the new azimuthal velocity dispersion can be expressed as the unperturbed velocity dispersion plus a rotation term. Now using the expression for the distortion given in Eq. (2.17) implies that

$$\tilde{\sigma}_\phi^2 = \sigma_\phi^2 + 2\xi v_{\text{rot}} P(v_{\text{rot}})(\sigma_\phi^2)^{-\frac{\gamma}{2}} \frac{1}{\rho} \int v_\phi^\gamma v_\phi f \, d^3v \; . \tag{2.23}$$

We are then left with evaluating an integral on the form

$$\frac{1}{\rho} \int v_\phi^k f \, d^3v \tag{2.24}$$

where $k = \gamma + 1$. If this integral becomes 0 the effect of adding rotation will vanish (since the ignored v_{rot}^2 is insignificant compared to σ_ϕ^2) which we must prevent. We will therefore demand that k takes the form $2m+2$ for $m = 0, 1, 2, \ldots$. Since $\gamma = 2n+1$ for $n = 0, 1, 2, \ldots$ this is always the case. Recognizing that the integral in Eq. (2.24) is just the expression for the k'th moment, α_k, for v_ϕ centered around the mean $\langle v_\phi \rangle = 0$ gives

$$\frac{1}{\rho} \int v_\phi^k f \, d^3v = \alpha_k (\sigma_\phi^2)^{k/2} \quad \text{with} \quad k = 2n + 2 \quad \text{for} \quad n = 0, 1, 2, \ldots \tag{2.25}$$

Combining this with the expression for the new velocity dispersion in Eq. (2.23) finally gives

$$\tilde{\sigma}_\phi^2 = \sigma_\phi^2 + 2\,\xi\,v_{\text{rot}}\,\alpha_{\gamma+1}\,P(v_{\text{rot}})\,\sqrt{\sigma_\phi^2} \; . \tag{2.26}$$

The only thing we need now is to quantify the $v_{\rm rot}$ dependency of the distortion of the DF. As mentioned above, we will show in Sec. 2.6 that intermediate and high resolution simulations of DM structures suggest a more or less constant dependency on $v_{\rm rot}$, i.e., a more or less 'flat' distortion with respect to $v_{\rm rot}$.

2.3   The $v_{\rm rot}$ Dependency in the DF Distortion in K15

The easiest way to quantify $P(v_{\rm rot})$ is by evaluating the quantity

$$P(v_{\rm rot}) \sim \frac{\tilde{\sigma}_\phi^2 - \sigma_\phi^2}{v_{\rm rot}\sqrt{\sigma_\phi^2}} \; . \tag{2.27}$$

In order to do this we were kindly provided some of the data from the high resolution N-body/gas dynamical simulated large disc galaxy 'K15' (Sommer-Larsen, 2006; Hansen & Sommer-Larsen, 2006).

This simulation is a significantly improved version of the TreeSPH code used previously for galaxy formation simulations (Sommer-Larsen et al., 2003). This simulation is based on a flat ΛCDM model with $(\Omega_M, \Omega_\Lambda) = (0.3, 0.7)$. It defines a grid with (DM and gas) particles. These particles are then given the characteristics of a given power spectrum, and are then followed in time as gravity is 'turned on'. The simulation takes many of the important factors of galaxy formation into account such as SN feedback, gas recycling (tracing 10 elements), atomic radiative cooling, etc. It consist of both cold and warm gas, DM, disk and bulge stars and stellar satellites. The galaxy K15 contains about 3×10^5 gas and DM particles and it has $m_{\rm gas} = m_{\rm stars} = 7.3 \times 10^5 M_\odot/h$ and $m_{\rm DM} = 4.2 \times 10^6 M_\odot/h$ where $h = 0.65$. Furthermore the gravitational (spline) softening lengths adopted are $\epsilon_{\rm gas} = \epsilon_{\rm stars} = 380$ and $\epsilon_{\rm DM} = 680 \, {\rm pc}/h$.[2]

Calculating the velocity dispersions for the DM particles in K15 and plotting P as given in Eq. (2.27) as a function of the actual $v_{\rm rot}$ in the structure for the trustable regions, i.e., from around 10 kpc (where the most of the gas disc vanishes) out to the virial radius, results in Fig. 2.1. Here we see a clear linear dependence. Combining that $P(v_{\rm rot}) = C_1 + C_2 v_{\rm rot}$ where the Cs are constants, with the expression in Eq. (2.26) gives

$$\tilde{\sigma}_\phi^2 = \sigma_\phi^2 + 2\,\xi\,\alpha_{\gamma+1}\,v_{\rm rot}\,\sqrt{\sigma_\phi^2}\,(C_1 + C_2 v_{\rm rot})\,. \tag{2.28}$$

Since we have assumed from the beginning that the added bulk rotation is just a small perturbation to the system, it is reasonable to ignore it in the linear relation and we therefore get

$$\tilde{\sigma}_\phi^2 = \sigma_\phi^2 + 12\,\eta\,\alpha_{\gamma+1}\,v_{\rm rot}\,\sqrt{\sigma_\phi^2}\,. \tag{2.29}$$

Here we have defined a new constant $\eta = \frac{C_1 \xi}{6}$ which will be dealt with in Sec. 2.6. As mentioned α is just the moment corresponding to the chosen value of γ (where

---

[2]For further information on the simulation please refer to Sommer-Larsen (2006) and Hansen & Sommer-Larsen (2006).

$Q \sim v_\phi^\gamma$), i.e., a constant. And since the above result only relies on the restrictions on γ it implies that the choice of γ doesn't result in loss of generality. Thus we are free to chose any value of γ when investigating the above equation. We will chose $\gamma = 3$ since we are then able to estimate the size of the moment. The fourth moment, i.e., the kurtosis of a Gaussian DF is 3, and since we expect the DFs of DM structures to be Gaussian like, using $\gamma = 3$ will make it easier to compare with simulations.

We then finally have the expression for the velocity dispersion, which we will use in the next sections when implementing the rotational effect into the Jeans equation and comparing this with DM simulations, namely

$$\tilde{\sigma}_\phi^2 = \sigma_\phi^2 + \eta \, 12 \, \alpha_4 \, v_{\rm rot} \, \sqrt{\sigma_\phi^2} \, . \tag{2.30}$$
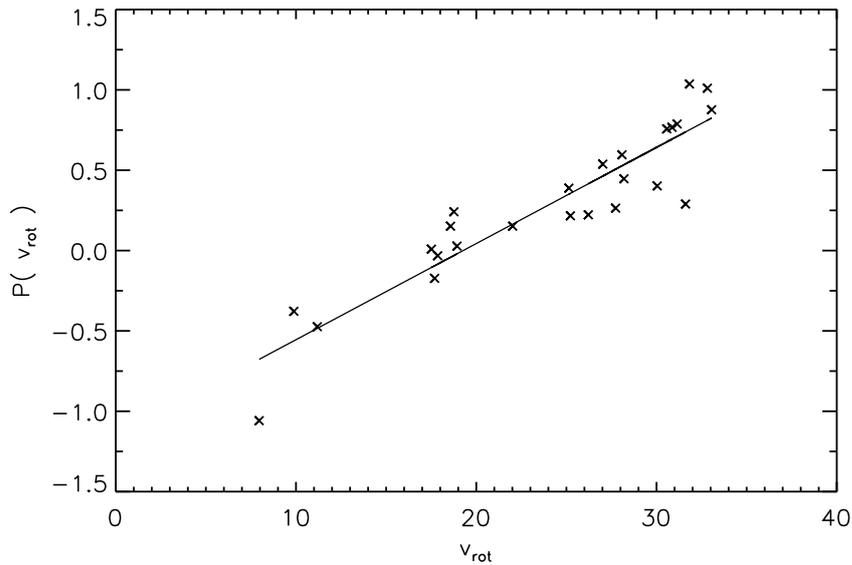
Figure 2.1: The v_{rot} dependence in the DF distortion quantified by the function P given in Eq. (2.27). The linear fit to the data is given by $(0.06 \pm 0.01) \times v_{rot} - (1.15 \pm 0.13)$ (full line).

2.4   The Suggested DF Distortion in K15

Before implementing the perturbed velocity dispersion into the Jeans equation, it would as mentioned earlier be interesting to see if the suggested distortion of the DF could be found in 'real' simulated galaxies.

Measuring the angular momentum direction in each bin of the structure K15, after aligning the potential contours so that their centers are the same, one can

look at the velocity distributions in the radial direction and the tangential directions perpendicular and parallel to the angular momentum vector. This will give 3 velocity DFs, of which only one contains rotation. If the suggested distortion of the DF caused by rotation should be present we would expect to see that when plotting the tangential DF for the velocities containing rotation (red dashed line in Fig. 2.2) and comparing with the tangential DF not containing rotation (blue dot-dashed line in Fig. 2.2). In Fig. 2.2 we have shown an example of the DFs of one of the bins in K15. We clearly see that the DF containing rotation is distorted whereas the two wings of both the radial and the non rotating tangential DF are remarkably symmetric. The plots for all the other trustable bins of K15 look the same. Thus if we consider a high resolution simulation of a 'real' galaxy containing gas, stars, DM etc., we clearly see a distortion of the DF containing the rotation of the galaxy. This supports our assumption of the existence of a $f - \tilde{f}$. However, more work needs to be done to show whether the actual form of the observed distortion equals the suggested one or not.
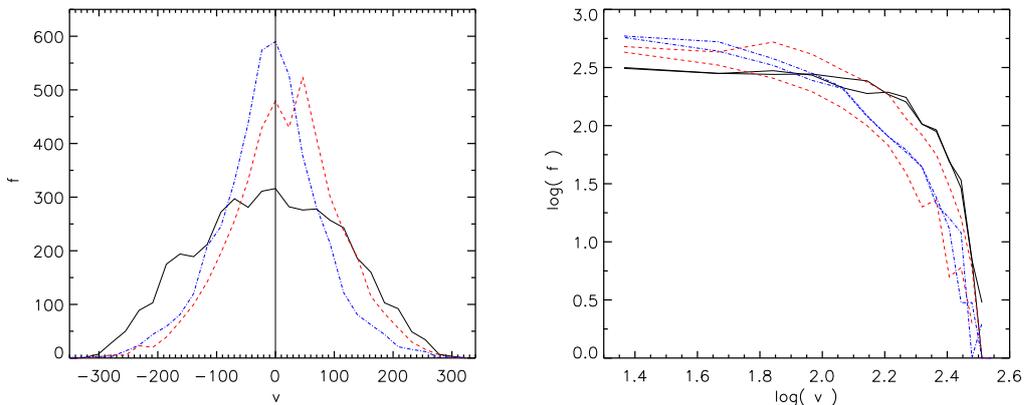
(a) *DFs for a bin of the galaxy K15.*

(b) *The left wings of the DFs mirrored and plotted with the right wings to ease comparison.*

Figure 2.2: The velocity DFs for one of the potential bins in the galaxy K15 in the radial direction (black full line) and the tangential direction perpendicular to (red dashed line) and parallel to (blue dot-dashed line) the angular momentum vector for the considered bin. We clearly see that the DF containing rotation, i.e., is perpendicular to the angular momentum vector is distorted as suggested. In Fig. 2.2a we see the actual DFs and in Fig. 2.2b we have mirrored the 'negative wing' of the DFs and plotted them in log so that the distortion is more easily seen. It is indeed remarkable how alike the wings of the non rotating and the radial DFs are.

2.5   The New Jeans Equation

Combining the expression for the azimuthal velocity dispersion after the small bulk rotation has been added to the system, Eq. (2.30), with the CJE on the form given in Eq. (2.12), leaves us with a new Jeans equation containing four terms. The 3 normal ones, dealing with the density, mass and velocity dispersion profile, and one new term describing the effect that rotation has on the system

$$\sigma_r^2 \frac{d\ln(\rho\sigma_r^2)}{d\ln r} + 2\beta\sigma_r^2 - \eta\,12\,\alpha_4\,v_{\rm rot}\sqrt{\sigma_\phi^2} = -\frac{GM}{r} \ . \tag{2.31}$$

Here β is the velocity anisotropy from Eq. (1.4), where it is assumed that $\sigma_\theta^2 = \sigma_\phi^2$. This just states that the thermal velocity moments in the tangential directions are equal, irrespective of the magnitude of the (small) bulk rotation.

   The dominating terms in Eq. (2.31) are the derivative of the density-dispersion term and the mass term. Assuming (for now) that the velocity anisotropy $\beta = 0$, and conjecturing that the rotation term, which is just a minor perturbation of the Jeans equation, must follow the profile of the dominating term, we can get a relation between the rotation, i.e., the specific angular momentum $j(r)$ and the total mass of the DM structure, which reads

$$\boxed{v_{\rm rot}\sqrt{\sigma_\phi^2} \sim \frac{GM}{r} \ .} \tag{2.32}$$

In principle many other solutions than the conjecture of the small term following the dominant one used above, are allowed to exist, but these would all imply some degree of compensation or fine-tuning between the various terms. We therefore suspect that there is a more physical explanation for why the $v_{\rm rot}\sqrt{\sigma_\phi^2}$ term is proportional to $\frac{GM}{r}$ than our conjecture, but none has been found so far.

   In the above argumentation leading to relation (2.32) there are no assumptions or knowledge about the merging history of our ensemble. Therefore our derivation possibly favors the tidal torque scenario (Sec. 1.3.4), i.e., Eq. (2.32) suggests that the angular momentum of DM structures is formed from velocity perturbations in the early universe, which provide the initial seed angular momentum, and is then grown through tidal forces between the dark matter structures (Peebles, 1969; Doroshkevich, 1970). Furthermore we see that when $M(< r) \to 0$, $v_{\rm rot} \to 0$. This indicates that the innermost bins/particles of the DM structure rotate very little.

   However, if we for instance imagine that every time a major merger happens the angular momentum profile is reset to follow our suggested rotational contribution, the above might also apply to the scenario, that the total angular momentum is a consequence of the DM structure merger history. Under all circumstances the different structures may have fairly different magnitudes of the angular momentum, and Eq. (2.32) expresses only that the radial *profile* of the angular momentum is always the same. The absolute *magnitude* is unknown, and may vary from structure to structure.

In a similar way we can look at the relationship between the $\beta \neq 0$ and the rotational term. We find from Eq. (2.31) that this connection is

$$v_{\text{rot}} \sqrt{\sigma_\phi^2} \sim \sigma_r^2 \beta \ .$$

(2.33)

This conjecture implies that if β goes to 0, the rotation term should go to 0 as well. The case $\beta < 0$ does not occur in the equilibrated part of the DM halo structure and has therefore no relevance to the problem at hand.[3] Since we are here suggesting a relation between the two minor terms in Eq. (2.31), relation (2.33) might not be as strong as the relation (2.32).

It is now straightforward to compare these predictions with the results from numerical simulations.

2.6   Comparing With Data

So far we have argued that there might be relations between the new rotational supplement to the Jeans equation and the mass and anisotropy of DM structures. To test that these relations are in fact interesting we compare the relations with recent high resolution numerical simulations of DM galaxies and clusters. Furthermore we use these structures to replicate plots of the evolution of the spin parameter (see Sec. 1.3.4) and to compare a new version of the spin parameter λ' containing our suggested rotational perturbation, with previous work.

2.6.1   The Simulation Data Files

To test whether our suggested relations are valid in simulations, we used 10 intermediately resolved numerical simulations of DM galaxy halos and clusters (Macciò et al., 2007), one high resolution cluster, C_{HR}.W3, and one high resolution galaxy, the 'Via Lactea' simulation (Diemand et al., 2007). As with the K15 galaxy we didn't perform these simulations ourselves. However, for consistency we will now give a short description of them.

The 10 intermediately resolved simulations have been performed using the PKD-GRAV treecode by Joachim Stadel and Thomas Quinn (Stadel, 2001). The initial conditions are generated with the GRAFIC2 package (Bertschinger, 2001). The starting redshifts z_i are set to the time when the standard deviation of the smallest density fluctuations resolved within the simulation box reaches 0.2 (the smallest scale resolved within the initial conditions is defined as twice the intra-particle distance). All the halos were identified using a spherical overdensity algorithm (Macciò et al., 2007). The cluster-like halos have been extracted from a 63.9 Mpc/h simulation containing 600^3 particles, with a mass resolution of $m_p = 8.98 \times 10^7 M_\odot/h$. The masses

---

[3]In the data presented in Sec. 2.6 as well as in the work by Dehnen & McLaughlin (2005), we do in fact see $\beta < 0$ points. However these points must be considered to be positive within errors in these regions, because of numerical resolution or softening.

of the clusters used for this study are 2.1, 1.8, and 1.6 $\times 10^{14} M_\odot/h$. The galaxy sized halos have been obtained by re-simulating halos found in the previous simulation at high resolution. The simulated halos are in the mass range $0.9 - 2.5 \times 10^{12} M_\odot/h$ and have a mass resolution of $m_p = 4.16 \times 10^5 M_\odot/h$. That gives a minimum number of particles per halo of about 2.5×10^6 particles. The high resolution cluster $C_{HR}.W3$ is based on the PKDGRAV as well and has 11 million particles within its virial radius and a mass of $M = 1.81 \times 10^{14} M_\odot/h$. The 'Via Lactea' (which is also based on the PKDGRAV code) simulation includes 234 million particles with a force resolution of 90 pc. The simulation includes one highly equilibrated structure of mass $M_{halo} = 1.77 \times 10^{12} M_\odot$, containing about 84 million particles (Diemand et al., 2007). This structure did not experience any major mergers since $z = 1$. All quantities are extracted in spherical bins.

Using the raw data from the structures which we were given, we created a data file also containing the velocity anisotropy, β, and the logarithmic density slope γ for each structure. We defined γ numerically as

$$-\gamma(j)_{\text{num}} = \frac{\log \rho(i+1) - \log \rho(i)}{\log r(i+1) - \log r(i)} \tag{2.34}$$

where i refers to the bin number in the structure and j refers to the radius to which γ is assigned, defined as $r_j = r_i + 0.5(r(i+1) - r(i))$.

In Table 2.1 we have collected some of the relevant values for the various structures, which will be used when evaluating the relations from the new Jeans equation, and furthermore when we investigate the Jeans equation itself in Sec. 3.

2.6.2   Results of Comparison

To start with we have plotted the relation between the rotation term and the mass term, Eq. (2.32), in Fig. 2.3. The diamonds, triangles, crosses and squares represent the galaxy and cluster sized halos from Macciò et al. (2007), the high resolution cluster $C_{HR}.W3$ and the Diemand et al. (2007) 'Via Lactea' high resolution simulation respectively. Each symbol represents the value for the given bin of the structure. Thus the 10th mass point represents the accumulated mass in the first 10 bins of the structure. In Fig. 2.3 we see a clear linear relation between our suggested rotation term and the actual total mass of the structure. This means that the generalized Jeans equation (Eq. (2.31)) determines the radial behavior of the rotation, i.e., the specific angular momentum $j(r)$ of the DM structure at hand. This explains why Bullock et al. (2001) find a strong relation between the angular momentum and the mass of similar structures, since our relation resembles the results of Bullock et al. (2001) mentioned in the introduction for a constant azimuthal velocity dispersion σ_ϕ^2. For each structure we have adjusted the normalization η_M for the mass relation, according to the values listed in Table 2.1. The error in the normalization $d\eta_M$ resembles a 'by-eye-fit' of the interval of η_M that makes the relation fit the best.

One might argue that this clear relation is just a coincidence, and would pop out for all relations having the right units. This we have tested and found not to

Simulation	η_β	$d\eta_\beta$	η_M	$d\eta_M$	$r_{\rm vir}$ [kpc]	$M_{\rm vir}$ [$M_\odot$]	$\sqrt{\sigma^2_{\phi,{\rm vir}}}$ [km/s]
'Via Lactea'	0.26	0.05	0.32	0.15	359	5.98e+11	89.1
G0.W1	0.25	0.10	0.70	0.40	260	1.24e+12	79.1
G1.W1	0.20	0.10	0.60	0.30	288	1.54e+12	97.7
G1.W3	0.28	0.08	0.65	0.33	333	1.89e+12	77.6
G2.W1	0.17	0.04	0.45	0.20	339	2.63e+12	128
G2.W3	0.32	0.08	0.80	0.35	288	1.11e+12	61.2
G3.W1	0.22	0.05	0.63	0.25	296	1.76e+12	94.4
G4.W3	0.31	0.07	0.85	0.45	218	5.96e+11	59.0
C1.W3	0.07	0.04	0.22	0.15	1440	2.13e+14	550
C2.W1	0.07	0.04	0.23	0.10	1440	2.12e+14	484
C3.W1	0.18	0.07	0.45	0.25	1600	1.89e+14	444
C_{HR}.W3	0.24	0.06	0.80	0.60	1671	3.23e+14	557

Table 2.1: Our free parameter η from Figs. 2.3 and 2.4, its errors and the mass and azimuthal velocity dispersion taken at the virial radius $r_{\rm vir}$, for the simulated DM structures. The errors on η_β and $\eta_{\rm mass}$ represent the interval in which the values give the best fit to the relation. For instance the 'Via Lactea' fits the mass relation in Fig. 2.3 reasonably well for $0.17 < \eta_{\rm mass} < 0.47$, i.e., 0.32 ± 0.15. All the structures are based on the PKDGRAV tree code. The 'Via Lactea' and the GX.XX are galaxy sized structures and the CX.XX are cluster sized structures. The XX.W1 is based on a WMAP 1-year data cosmology ($h = 0.71$ and $\Omega_m = 0.268$), whereas XX.W3 is based on a WMAP 3-year data cosmology ($h = 0.73$ and $\Omega_m = 0.238$). For more information on the structures, refer to Sec. 2.6.1 or see Diemand et al. (2007) and Macciò et al. (2007).
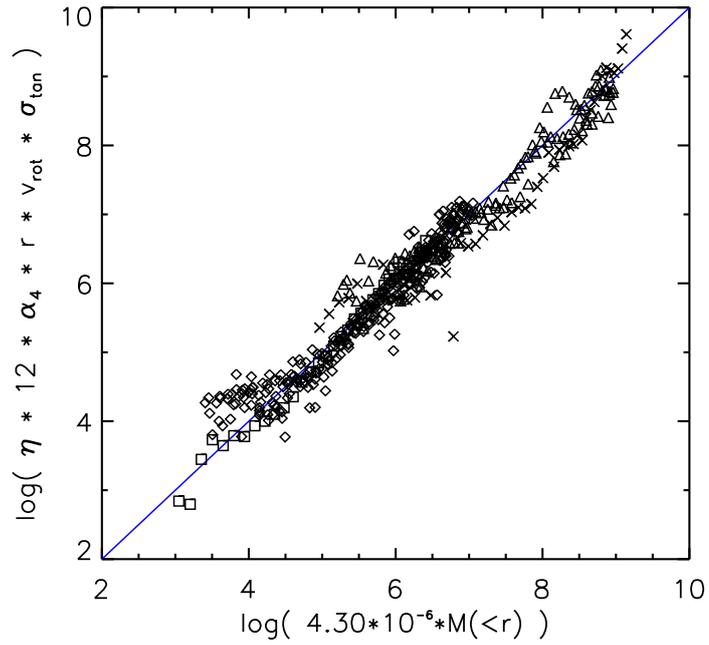
Figure 2.3: The suggested connection between the mass (r.h.s. of the new Jeans equation, Eq. (2.31)) on the x-axis, and the new rotational term (full line) on the y-axis. The diamonds, triangles, crosses and squares represent the galaxy sized halos and the cluster sized halos from the simulations by Macciò et al. (2007), the high resolution $C_{HR}.W3$ cluster and the Diemand et al. (2007) "Via Lactea" high resolution simulation respectively. This illustrates that the Jeans equation determines the radial behavior of the rotation, i.e., the specific angular momentum $j(r)$. We use SI units and $\alpha_4 = 3$. The factor $4.30 \cdot 10^{-6}$ includes the gravitational constant G, and is the correction needed to have the quantities in SI units. The η for each structure corresponds to the ones listed in Table 2.1.

be so. If we don't ignore the higher order terms when expressing the perturbed velocity anisotropy $\tilde{\sigma}_\phi^2$ we would get a relation between $v_{\rm rot}^2 r$ and the mass term when plugging this into the Jeans equation. This however doesn't have the correct behavior when compared to the simulation. This has also been shown by Højsgaard et al. (2007). We are therefore convinced that ignoring higher order terms in $v_{\rm rot}$ is indeed justified.
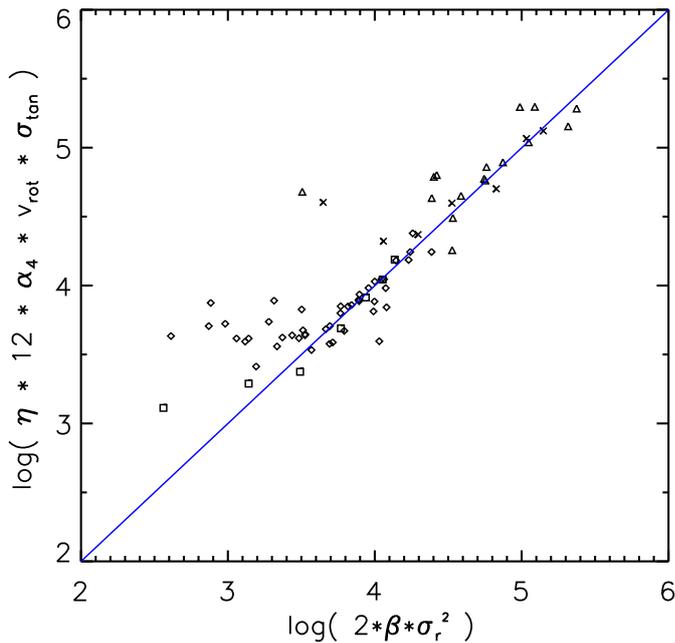
Figure 2.4: The relation between the thermal velocity anisotropy β and the rotation-term (solid line) in Eq. (2.33). The diamonds, triangles, crosses and squares represent the galaxy sized halos and the cluster sized halos from the simulations by Macciò et al. (2007), the high resolution $C_{HR}.W3$ cluster and the Diemand et al. (2007) "Via Lactea" high resolution simulation respectively. In plotting the data we have cut off the structures so that all the points can be considered to be equilibrated. We have determined the cutoff-points by excluding the (outer) part of the structures, where the velocity anisotropy, is not a (roughly) monotonically increasing function of radius and where γ clearly shows disturbances in the density indicating that the structure is not fully equilibrated. Furthermore we have re-binned the data to reduce scatter, so that each point now contains roughly 1/7 of the structure. We again use SI units, $\alpha_4 = 3$ and different η for each structure as listed in Table 2.1.

Likewise we can test the prediction of a linear relationship between the velocity anisotropy and the bulk rotation (Eq. (2.33)) against the data. In Fig. 2.4 we have plotted these quantities for the simulated structures. Again we see a correlation

between the actual data and our predicted relationship. In this figure we have in contrast to Fig. 2.3 rebinned the data to reduce the scatter in the plot, so each point now contains roughly 1/7 of the structure. Furthermore we have cut off the outer bins of the structures where the velocity anisotropy β was no longer a monotonically increasing function of radius and where the density profile γ indicated that the structures were not yet fully equilibrated. Plotting the structures without making an outer cut to smoothen the velocity anisotropy doesn't change the picture but only enhances the scatter. Structures with non monotonic β profiles are most likely not equilibrated yet and are therefore not suitable to test our suggested relations. Nevertheless we suggest that structures with for instance gas cooling (which might change the β profile) also obey our relations in a similar way to the findings that β strictly follows the density slope in Hansen & Moore (2006).

The relationship between $\sigma_r^2 \beta$ and $v_{\rm rot}\sqrt{\sigma_\phi^2}$ supports the idea that the Jeans equation determines the radial behavior of the rotation of the DM structures.
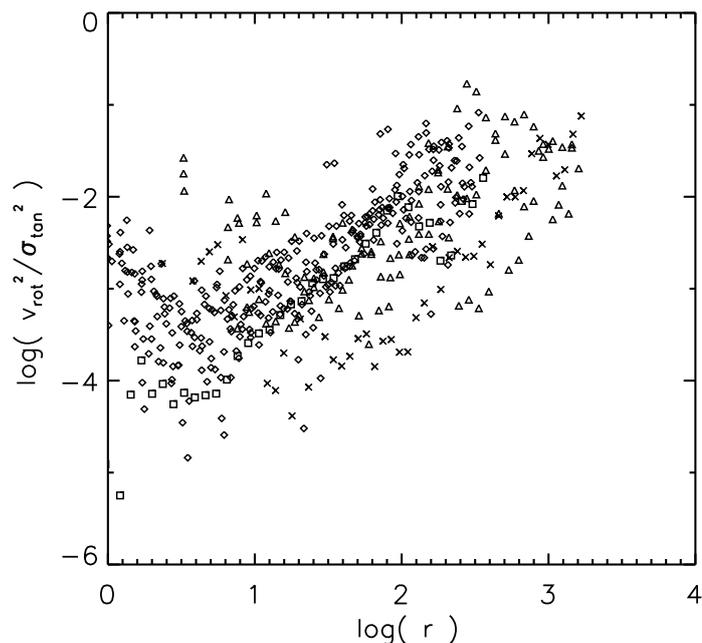
Figure 2.5: The fraction of the kinetic energy in rotation for the structures in Table 2.1 as a function of radius. The symbols are the same as in Figs. 2.3 and 2.4. Here the radius is given in kpc. That the kinetic energy in rotation drops by two orders of magnitude supports the prediction that the rotational term goes to zero for β approaching zero.

We see that the rotation term goes to 0 as β goes to 0, exactly as predicted. In fact, if we plot the fraction of the kinetic energy in rotation, i.e., $v_{\rm rot}^2/\sigma_\phi^2$ as a function

of radius as done in Fig. 2.5, we see that for all the structures the energy drops by two orders of magnitude, from $\sim 10^{-2}$ in the outskirts, down below $\sim 10^{-4}$ for the inner-most bins. Since β is in general monotonically increasing as a function of radius, the fact that the rotation becomes so small in the inner parts of the structure supports our prediction of the rotation term going towards 0 for small β.
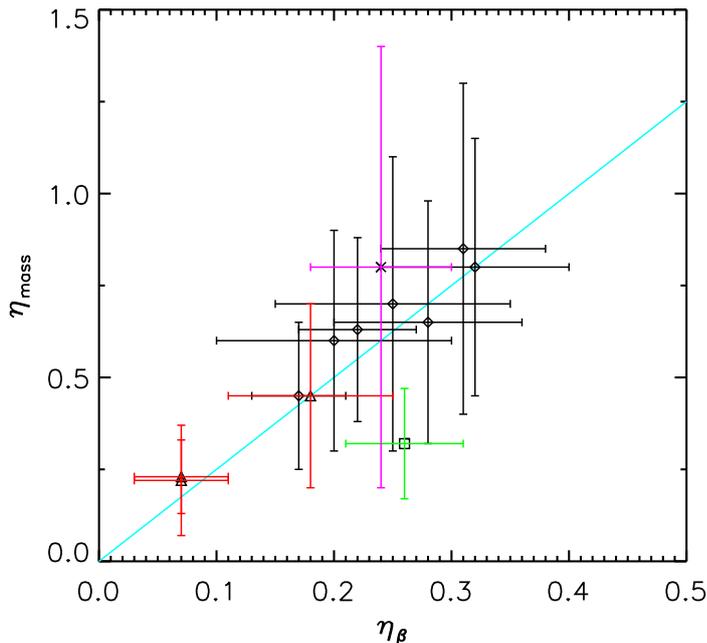
Figure 2.6: The free parameter η_{mass} obtained from the relation plotted in Fig. 2.3 and η_β obtained from the relation in Fig. 2.4, plotted against each other. The solid guide-the-eye line represents the relation $\eta_{mass} = 2.5\eta_\beta$. The error bars represent the interval in which the η values give the best fit to the prediction. For instance the 'Via Lactea' (square) fits the mass relation in Fig. 2.3 reasonably well for $0.17 < \eta_{mass} < 0.47$, i.e., 0.32 ± 0.15 as written in Table. 2.1. The symbols are the same as in Fig. 2.3.

In Figs. 2.3 and 2.4 the only free parameter in our prediction, η, has been fitted for each structure. These values of η corresponding to the relations in Eqs. (2.32) and (2.33) together with the estimated errors are shown in Table 2.1. As mentioned the errors are an indication of an 'by-eye-estimate' of the range in which η can lie according to the relations. Plotting these values and their errors gives Fig. 2.6. Here we see a tendency of η_M being a bit larger than η_β. Since the three triangles and the cross are cluster like structures and the rest are galaxy like structures we notice that there might be a connection between η and the mass of the structures. In Fig. 2.7 we plot η_β (since it has the smallest error bars, percentage-wise) against the

estimated virial mass of each structure (see Table 2.1). Here we see that our free
parameter anti-correlates slightly with the mass of the structure. So according to
our predictions the effect an added bulk rotation has on a system is anti-correlated
with the virial mass of that system. We have not been able come up with any
acceptable explanation to why this is so. It might be that this is just because the
linear appearance of $P(v_{\mathrm{rot}})$ scales differently for different sizes of structures, or that
the distortion of the DFs is smaller in general for massive structures. Honestly we
don't now but it would definitely be interesting to collect more data similar to the
K15 data, to see if there are any trends as a function of mass in plots like the ones
in Figs. 2.1 and 2.2.
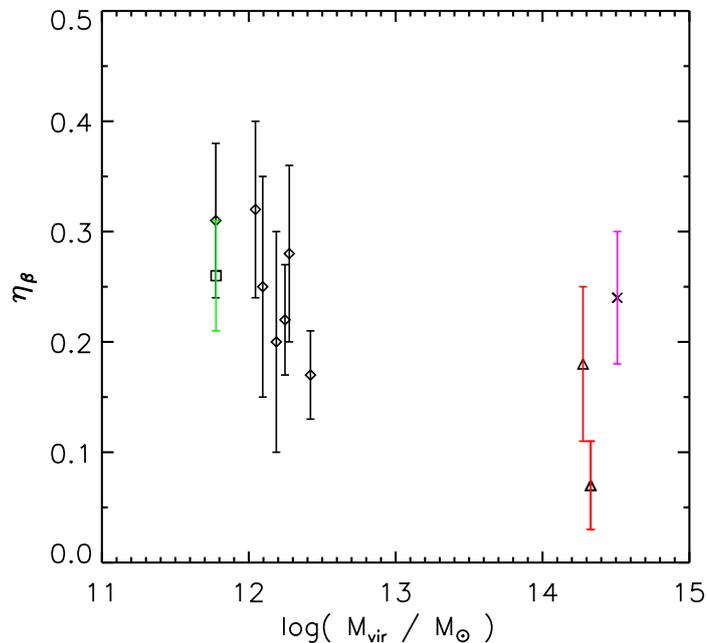
*Figure 2.7: The free parameter η_β plotted against the virial mass of each structure
(listed in Table 2.1). The symbols are the same as in Fig. 2.3. The slight decrease
as a function of mass indicates that the rotational effect on a system is relatively
smaller for massive systems.*

After having tested our theoretically suggested relations from the previous section
with the simulations from Macciò et al. (2007), we also held them up against the
recent high resolution numerical simulation 'Via Lactea' by Diemand et al. (2007),
to make sure that the results are not just a coincidence caused by a lack of numerical
resolution. The 'Via Lactea' is one of the most highly resolved structures available
today. We have plotted the high resolution data as squares in Figs. 2.3-2.7 for
comparison. In Fig. 2.8 we have plotted the 'Via Lactea' alone, without any cutoffs

or re-binning. In this figure we are still using the values of η from Table 2.1. We see that our relations are also confirmed when comparing with the best resolved data available today. Due to numerical softening we can safely trust the radius outside 1 kpc of this galaxy. On the other hand the outermost 6-10 points should be considered with care since they are potentially not fully equilibrated yet. It is points like these we have cut off in Fig. 2.4. That the structure is not yet fully equilibrated in the outer regions/bins is easily seen when considering the radial derivative of the density profile γ.

(a) *The v_{rot}-M relation.*   (b) *The v_{rot}-β relation.*
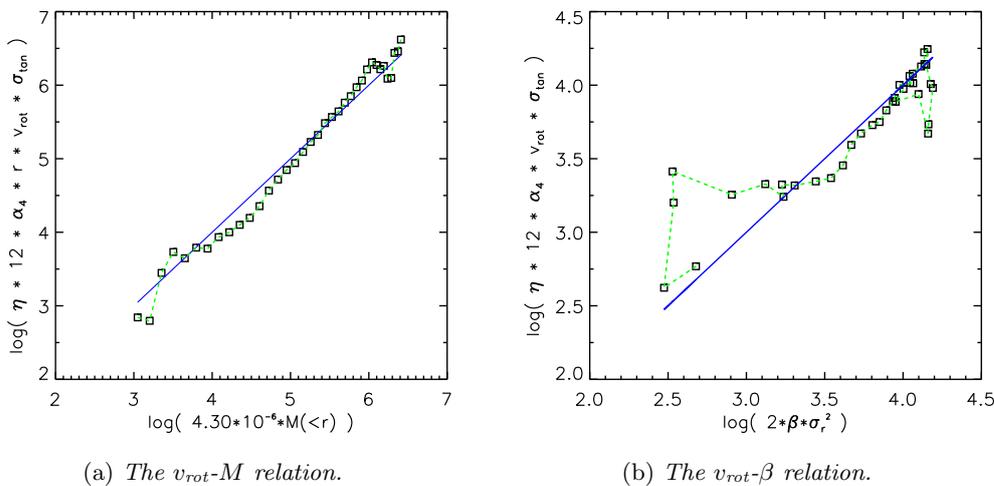
Figure 2.8: The same plots as in Figs. 2.3 and 2.4 containing only the data from the Diemand et al. (2007) "Via Lactea" high resolution simulation. We have only plotted the numerically simulated points (squares) in the resolved region, i.e., outside $r = 1$ kpc, and out to $r = r_{200}$. The outermost 6 to 10 points (top right corner) are possibly not yet fully equilibrated (clearly visible when considering $\frac{d\ln\rho}{d\ln r}$ as a function of radius) and might therefore be ignored. We use SI units, and $\alpha_4 = 3$. In Fig. 2.8a $\eta = 0.32$. The factor $4.30 \cdot 10^{-6}$ includes the gravitational constant G, and is the correction needed to have the quantities in SI units. In Fig. 2.8b $\eta = 0.26$. The two ηs and their estimated errors are listen in Table 2.1 alongside the η-values for the other simulations.

We have thus compared the angular momentum of the intermediate resolution structures, the highly resolved $C_{HR}.W3$ cluster, and the 'Via Lactea' simulation with our relations, and see strong correlations between the rotation, mass and velocity anisotropy of the DM systems.

2.6.3   The Effect on the Spin Parameter

As mentioned earlier people often use the spin parameter when describing the angular momentum and rotation of (DM) structures in general. Combining our suggested

relation between the mass and the angular momentum with the spin parameter as defined by Bullock et al. (2001) in Eq. (1.7), we can achieve a new form of the spin parameter in the following way

$$
\begin{aligned}
\lambda' &= \frac{Mrv_{\text{rot}}}{\sqrt{2GM^3 r}} = \frac{1}{\sqrt{2}} \frac{v_{\text{rot}}}{\sqrt{\frac{GM}{r}}} = \frac{1}{\sqrt{2}} \frac{GM}{\eta \, 12 \, \alpha_4 \sigma_\phi^2 \, r \sqrt{\frac{GM}{r}}} \\
&= \frac{1}{\sqrt{2} \, \eta \, 12 \, \alpha_4} \frac{v_c}{\sqrt{\sigma_\phi^2}} \; .
\end{aligned}
\tag{2.35}
$$

Here the ordinary circular velocity is defined as $v_c^2 = \frac{GM}{r}$. We are therefore able to describe the spin parameter only as a function of the total mass and σ_ϕ^2, without any dependence on the bulk rotation v_{rot}. In general the size of the value λ' from Eq. (2.35) (as shown in Fig. 2.9 and 2.10) agrees with the empirical mean spin value of 0.05 (Vitvitska et al., 2002). In Fig. 2.9 we have plotted Eq. (2.35) for the simulated structures. This figure agrees fairly well with Fig. 5 of Ascasibar & Gottlöber (2008). If we estimate a gradient of our plot we get approximately between 1/4 and 1/5 (depending on the chosen structure), whereas an estimated gradient on Fig. 5 in Ascasibar & Gottlöber (2008) is closer to 1/6. Thus Eq. (2.32) appears to roughly explain the observed tendency of an increase in the spin parameter as a function of radius in DM structures. If we instead of having the v_{rot} dependence, had a v_{rot}^2 dependence in the suggested rotational supplement, we would get a constant spin parameter. And since this is clearly not in agreement with the work by Ascasibar & Gottlöber (2008), we take this as another indication that ignoring higher order terms in v_{rot} is justified.

Furthermore it has been suggested that the spin parameter doesn't depend on the virial mass of the structures (Macciò et al., 2007). To test this we plot in Fig. 2.10, the values of λ' from Eq. (2.35) taken at the virial radius of the structures. To calculate λ'_{vir} we used the values given in Table 2.1. Here we see the indication of a slight increase in spin as the virial mass of the structure grows. The linear fit in Fig. 2.10 (full line) has an inclination of 0.09 ± 0.04. One possible explanation for the indication of a mass dependence might be the fact that the spin is taken at r_{vir}. As pointed out by Ascasibar & Gottlöber (2008) the use of r_{vir} (compared to their R_{max}) might be too 'non-conservative' when estimating the various properties of equilibrated structures. On the other hand it is not surprising to have a slight increase in spin, since the spin parameter as defined in Eq. (2.35) basically resembles a relation between η_{mass} and M_{vir} similar to the one shown for η_β in Fig. 2.7. Nevertheless, because of the large scatter and error-bars in our points we must conclude that there is no (significant) dependence between our spin parameter and the virial mass of the structures. This is in agreement with the lower part of Fig. 3 in Macciò et al. (2007), which also shows that a relatively large scatter in the λ'_{vir} of DM structures is usual.
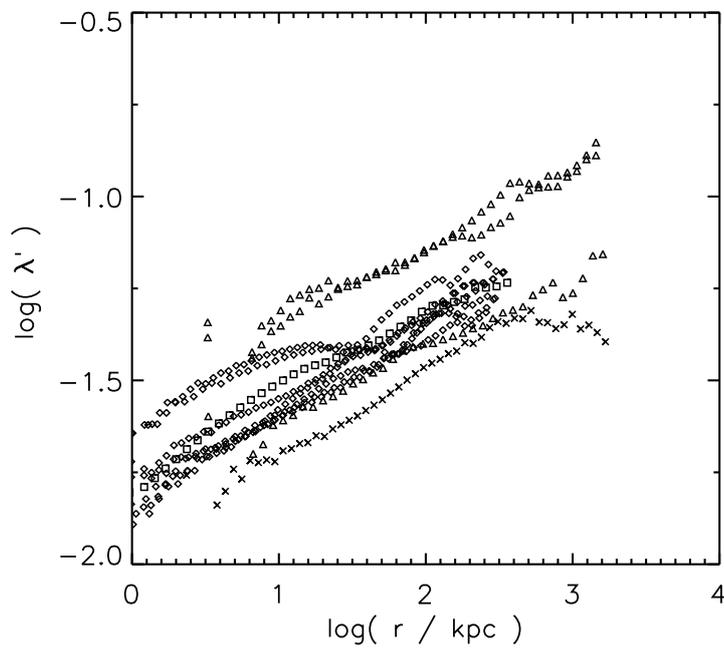
Figure 2.9: The spin parameter λ' as defined in Eq. (2.35) plotted as a function of radius. The symbols are the same as in Fig. 2.3. We see that depending on the structure used as reference the spin parameter grows with a gradient between 1/4 and 1/5 as a function of radius. This is in agreement with the work by Ascasibar & Gottlöber (2008).
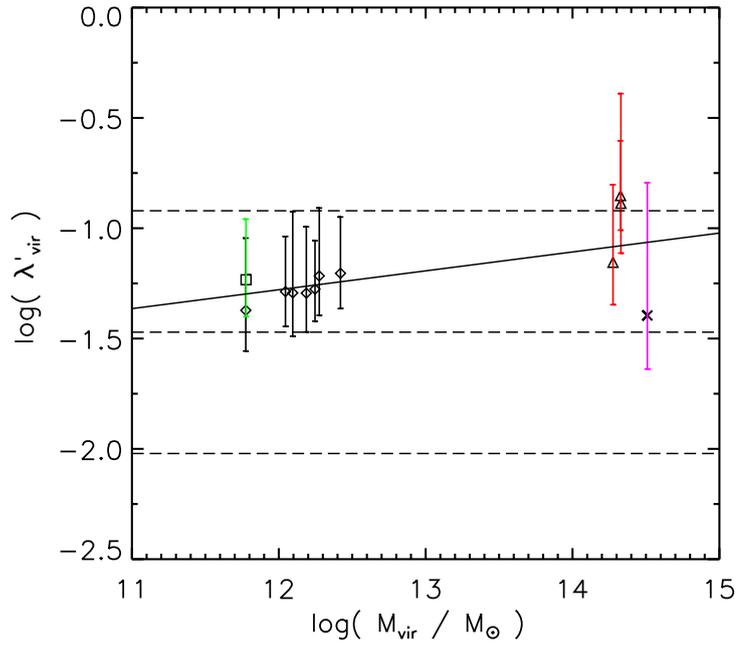
Figure 2.10: The spin parameter defined in Eq. (2.35) at the virial radius for the structures in Table 2.1. The linear fit to the points (full line) is given by $(0.09 \pm 0.04) \times \log(M_{\mathrm{vir}}/M_\odot) - (2.31 \pm 0.51)$. The errors correspond to the error in η_{mass} (see Table 2.1) used when calculating λ'_{vir}. Because of the scatter and the relatively large errors we can't conclude that the mass dependence is significant. The dotted lines represents the mean (0.034 ± 0.001) and 2σ scatter (0.55 ± 0.01) from Macciò et al. (2007), which are in agreement with the results of Bullock et al. (2001). The symbols are the same as in Fig. 2.3.

2.7 Conclusion

To sum up the conclusions in the 'rotation'-part of the work, we have investigated the spherical collisionless steady state Jeans equation when including angular momentum. This added bulk motion leads to a new, more general, CJE containing a new subdominant rotational term. This is achieved by assuming that the velocity distribution function of the DM particle ensemble is distorted by the added bulk rotation, and that this distortion can be represented by a distortion of the velocity dispersion when adding rotation. A distortion of the DF is shown to be visible when plotting the DFs of 'real' simulated galaxies like the K15 created by Sommer-Larsen et al. (2003). Furthermore we assume that higher order terms in $v_{\rm rot}$ are ignorable since $v_{\rm rot}^2 \ll \sigma_\phi^2$. The new subdominant term in the Jeans equation enables us to suggest relations between the rotation, i.e., the angular momentum of DM structures and their mass and velocity anisotropy respectively. The analytically suggested relations are

$$v_{\rm rot}\sqrt{\sigma_\phi^2} \sim -\frac{GM}{r} \qquad \text{and} \qquad v_{\rm rot}\sqrt{\sigma_\phi^2} \sim \sigma_r^2\beta \ . \tag{2.36}$$

We have tested our relations against recent intermediate and high resolution simulations of galaxies and clusters. Both the mass and velocity anisotropy relation are in good agreement with the findings of these numerical simulations as illustrated in Figs. 2.3 and 2.4.

Since the relations are derived with no assumption about the formation of the DM structures and no knowledge of their merger history, they demonstrate that irrespective of how and where the DM structures have formed the behavior of their angular momentum is governed by the new Jeans equation (Eq. (2.31)). This could also be an indication that the tidal-torque scenario which tries to explain the origin of DM angular momentum is favored by this approach. Only if one would imagine that mergers reset the angular momentum profile to the one suggested here, our relations would support the merging history scenario.

We have also derived a new form of the spin parameter (Eq. (2.35)) using our relation between the angular momentum and the mass of the structure. This spin parameter is shown to increase slowly as a function of radius, which is in agreement with recent work by Ascasibar & Gottlöber (2008). Furthermore our mass relation indicate that there is no (significant) increase in the spin parameter at the virial mass of the structures, i.e., no dependence between $\lambda'_{\rm vir}$ and $M_{\rm vir}$. This is also in agreement with recent studies (Macciò et al., 2007).

The main work and results from this section have been summed up in Schmidt et al. (2008) and has been submitted to ApJ.

3 Investigation of the Jeans Equation

In this section we will describe the second part of the work. This is inspired by the work of Dehnen & McLaughlin (2005) (and Austin et al. (2005)) on the spherical Jeans equation. The purpose of the presented work is to get new insight into the Jeans equation in general, and to extend the analysis of Dehnen & McLaughlin (2005) to a more general case. This we will do by deriving a new even more general equation for the behavior of DM structures (Eq. (3.11)), resulting in the huge task of understanding and analyzing this new equation. This we will try to do by 'attacking' the equation from different angles. On one hand we will try to understand the crucial parameters by optimizing them through a Monte Carlo code. On the other we will analyze the equation analytically, trying to get a handle on the behavior and the convergences of it. To set our work into context, and to introduce the general idea of some of it, we will start with a brief summery of the approach taken in Dehnen & McLaughlin (2005).

3.1 The Work by Dehnen and McLaughlin

The paper Dehnen & McLaughlin (2005) (henceforth DM05) is divided into three major parts. In the first part DM05 take the (not completely accurate) approach of describing a DM structure with an isotropic velocity distribution. Secondly they consider the (more correct) case of a DM structure with a velocity anisotropy (as defined in Eq. (1.4)) different from 0, and finally they compare their results with recent simulations of different structures. We will here concentrate on the second part which we will try to improve (make more general) in the following sections.

DM05 assumes as a starting point that the phase space density for the DM structures goes as a power law in radius, i.e., they assume that

$$\frac{\rho}{\sigma_r^\epsilon} = \frac{\rho_0}{\sigma_{r,0}^\epsilon} \left(\frac{r}{r_0}\right)^{-\alpha} . \tag{3.1}$$

This is a phase space density (like) relation similar to Eq. (1.3). Here ϵ is some positive constant. For the isotropic case ϵ is often put equal to 3. The σ_r refers to the velocity dispersion in the radial direction and the subscript '$_0$' refers to some suitable reference value of the given parameter. Combining this *ansatz* with the CJE (Eq. (2.12)) gives an equation relating the density slope and r of the DM structure. Deriving this equation (Eq. (22) in DM05) DM05 use the logarithmic density slope γ defined (from Eq. (1.1)) as

$$-\gamma \equiv \frac{d \ln \frac{\rho}{\rho_0}}{d \ln \frac{r}{r_0}} . \tag{3.2}$$

Furthermore assuming a linear relationship between the velocity anisotropy and γ, i.e., $\beta = \beta_0 + b_{\mathrm{DM}}\gamma$ makes the equation take the form

$$\gamma' - \frac{2}{\epsilon}(\gamma - \gamma_a)(\gamma - \gamma_b) = \frac{\epsilon}{2 + \epsilon - 2b_{\mathrm{DM}}} \left(\frac{4\pi G \rho_0 r_0^2}{\sigma_{r,0}^2}\right) \left(\frac{\rho}{\rho_0}\right)^{1-2/\epsilon} \left(\frac{r}{r_0}\right)^{2-2\alpha/\epsilon} , \tag{3.3}$$

where

$$\gamma_a = \frac{2\alpha}{2+\epsilon} + \frac{2\epsilon}{2+\epsilon}\beta_0 \qquad \text{and} \qquad \gamma_b = \alpha + \frac{\epsilon}{2} \; . \tag{3.4}$$

It is a generalization of Eq. (3.3) we will derive and investigate in the following sections. The linear relationship between β and γ is according to DM05 naturally suggested by the Jeans equation itself since it makes ugly terms cancel in their calculations.

Taking the derivative of Eq. (3.3) enables DM05 to estimate a critical value for the α parameter. Similarly they argue that the only acceptable solution in the isotropic case is $\alpha_{\text{crit}} = 1.9\overline{4}$. In the anisotropic case DM05 get

$$\alpha_{\text{crit}} = \frac{(10-\epsilon)(2+\epsilon)}{2(6+\epsilon)} - \frac{2(\epsilon-2)}{6+\epsilon}\beta_0 \; . \tag{3.5}$$

Substituting this expression into the other equations described in DM05, they are able to give analytical expressions for the velocity anisotropy, the density profile, the density slope, the radial velocity dispersion profile, the mass profile, the circular velocity profile, and finally the gravitational potential $\Phi(r)$ arising from the given DM structure. In the third and final part of their work they compare these analytical equations with 10 simulated CDM structures. When comparing with simulations they assume that all halos follow the same relation, $\rho/\sigma_r^\epsilon \propto r^{\alpha_{\text{crit}}}$, with a single value of ϵ. Under this (rather crude assumption) they find that their predicted relations, fit the simulated halos quite well. Using $\epsilon = 3$ and $\beta_0 = -0.1$ they predict that in the isotropic case $\alpha_{\text{crit}} = 1.9\overline{6}$.

3.2   Generalizing the Approach by Dehnen and McLaughlin

Our approach to the investigation of the Jeans equation is similar to the approach by DM05, but more general in the sense that we don't restrict ourselves by assuming that the velocity dispersion in the *ansatz* Eq. (3.1) is only radial. We instead use a general velocity dispersion on the form

$$\sigma_D^\epsilon = \sigma_r^\epsilon \left(1 + D\beta\right)^{\epsilon/2} \; . \tag{3.6}$$

Here β is the velocity anisotropy of the DM ensemble defined in Eq. (1.4). Hence we allow the velocity dispersion σ_D to be a combination of all three spherical components, σ_r, σ_ϕ and σ_θ. In this context, what DM05 did, was to set $D = 0$. If we instead have that $D = -\frac{2}{3}$, σ_D would take the form $\sigma_D = \sigma_{\text{tot}} = (\frac{1}{3}(\sigma_r^2 + \sigma_\phi^2 + \sigma_\theta^2))^{1/2}$. Other examples are given in Table 3.4 page 54. Similar to DM05 we also assume that the velocity dispersion is dependent on r and ρ in such a way that the phase space density goes as a power law in radius. Compared to the phase space density used by DM05 in Eq. (3.1) we are thus left with a more general expression on the form

$$\frac{\rho}{\sigma_D^\epsilon} = \frac{\rho_0}{\sigma_{D,0}^\epsilon} \left(\frac{r}{r_0}\right)^{-\alpha} \; . \tag{3.7}$$

Here the zeros still refer to some suitable normalization constants. In general we therefore have that

$$\rho/\sigma_D^\epsilon \propto r^{-\alpha} \ . \tag{3.8}$$

Combining Eq. (3.7) with the definition of σ_D in Eq. (3.6) gives us an expression for the radial velocity dispersion which can be plugged into the CJE in the form of Eq. (2.11) to give

$$
\begin{aligned}
4\pi G\rho r^2 \ = \ & \frac{d}{dr}\left[-\frac{r^2}{\rho}\frac{d}{dr}\left(\frac{\rho^2 \sigma_{D,0}\left(\frac{\rho}{\rho_0}\right)^{1/\epsilon}\left(\frac{r}{r_0}\right)^{\alpha/\epsilon}}{(1+D\beta)^{1/2}} \right)^2 \right. \\
& \left. -2\beta r\left(\frac{\sigma_{D,0}\left(\frac{\rho}{\rho_0}\right)^{1/\epsilon}\left(\frac{r}{r_0}\right)^{\alpha/\epsilon}}{(1+D\beta)^{1/2}} \right)^2 \right]
\end{aligned}
\tag{3.9}
$$

which is yet another form of the CJE. Introducing $x = \frac{r}{r_0}$, $y = \frac{\rho}{\rho_0}$, $f = \frac{2+\epsilon}{\epsilon}$ (not to be confused with the DF from Sec. 2), $g = \frac{2\alpha}{\epsilon}$, $\kappa = \frac{4\pi G\rho_0 r_0^2}{\sigma_{D,0}^2}$ and $\tilde\beta = (1+D\beta)^{-1}$ and using that $\frac{d}{dz} = \frac{d}{z\,d\ln z}$ we are left with

$$-\kappa = \frac{1}{yx^3}\frac{d}{d\ln x}\left[\frac{x}{y}\frac{d}{d\ln x}\left(y^f x^g \tilde\beta \right) \right] + \frac{2}{Dyx^3}\frac{d}{d\ln x}\left[y^{f-1}x^{g+1}(1-\tilde\beta) \right] \tag{3.10}$$

This equation can be reduced and rewritten to an equation relating multiple derivatives of the logarithmic density slope as a function of radius of the DM structure γ, with the density ρ and radius r. We will refer to this equation as the 'master equation' and it can be written as

$$
\boxed{
\begin{aligned}
-\frac{\kappa}{b}y^{1-2/\epsilon}x^{2-2\alpha/\epsilon} = \ & \gamma'' - \gamma'\left[\frac{2}{\epsilon}(\gamma-\gamma_3) + \frac{2+\epsilon}{\epsilon}((\gamma-\gamma_-)+(\gamma-\gamma_+)) \right] \\
& + \frac{2(2+\epsilon)}{\epsilon^2}(\gamma-\gamma_3)(\gamma-\gamma_-)(\gamma-\gamma_+) \qquad \text{with} \\
\gamma_3 = \ & \alpha + \frac{\epsilon}{2} \qquad\qquad\qquad\qquad\qquad\qquad\qquad\quad \text{and} \\
\gamma_\pm = \ & -\frac{a}{2b} + \frac{\alpha-\frac{\epsilon}{D}}{2+\epsilon} \pm \frac{1}{2}\sqrt{\text{DISC}}
\end{aligned}
}
\qquad
\begin{aligned}
& \\
& \\
& (3.11) \\
& (3.12) \\
& (3.13)
\end{aligned}
$$

Here DISC is the discriminant from solving a 2nd order polynomial in γ. The γ_3 equals the γ_b of DM05. This equation is the generalization of Eq. (3.3) (Eq. (24) in DM05), where the velocity dispersion is allowed to be a combination of all three spherical components in the phase space density, Eq. (3.8). For the expression of DISC and the exact calculations going from Eq. (3.10) to Eq. (3.11) please refer to App. B. Getting to this expression we assume a linear relation between the density slope of the DM structure and the velocity anisotropy, such that

$$\tilde\beta = \frac{1}{1+D\beta} = a + b\gamma \ , \text{ for } D \neq 0 \ . \tag{3.14}$$

This relation corresponds to the relation $\beta = \beta_0 + b_{\mathrm{DM}}\gamma$ in DM05.

Following DM05 and Austin et al. (2005) it will come in handy to calculate the derivative of the master equation with respect to the radius. If we for simplicity let [1] represent the expression

$$\frac{2}{\epsilon}(\gamma - \gamma_3) + \frac{2+\epsilon}{\epsilon}\left((\gamma - \gamma_-) + (\gamma - \gamma_+)\right) \tag{3.15}$$

with γ_3 and $\gamma_\pm$ defined in Eq. (3.12) and (3.13) respectively, we have that

$$0 = \frac{d}{d\ln x}\left[y^{2/\epsilon-1}x^{2\alpha/\epsilon-2}\left(\gamma'' - \gamma'[1] + \frac{2(2+\epsilon)}{\epsilon^2}(\gamma - \gamma_3)(\gamma - \gamma_+)(\gamma - \gamma_-)\right)\right]. \tag{3.16}$$

Performing the differentiation then gives

$$
\begin{aligned}
0 &= \left(\left(\frac{2\alpha}{\epsilon}\right) - \gamma\left(\frac{2}{\epsilon} - 1\right)\right)y^{2/\epsilon-1}x^{2\alpha/\epsilon-2} \times \\
&\quad \left(\gamma'' - \gamma'[1] + \frac{2(2+\epsilon)}{\epsilon^2}(\gamma - \gamma_3)(\gamma - \gamma_+)(\gamma - \gamma_-)\right) \\
&\quad + y^{2/\epsilon-1}x^{2\alpha/\epsilon-2}\frac{d}{d\ln x}\left(\gamma'' - \gamma'[1] + \frac{2(2+\epsilon)}{\epsilon^2}(\gamma - \gamma_3)(\gamma - \gamma_+)(\gamma - \gamma_-)\right) \\
&= \left(\left(\frac{2\alpha}{\epsilon}\right) - \gamma\left(\frac{2}{\epsilon} - 1\right)\right)\left(\gamma'' - \gamma'[1] + \frac{2(2+\epsilon)}{\epsilon^2}(\gamma - \gamma_3)(\gamma - \gamma_+)(\gamma - \gamma_-)\right) \\
&\quad + \gamma''' - \gamma''[1] - \gamma'\frac{d}{d\ln x}[1] + \frac{2(2+\epsilon)}{\epsilon^2}\frac{d}{d\ln x}(\gamma - \gamma_3)(\gamma - \gamma_+)(\gamma - \gamma_-).
\end{aligned}
$$

Using that

$$
\begin{aligned}
\frac{d}{d\ln x}(\gamma - \gamma_3)(\gamma - \gamma_+)(\gamma - \gamma_-) = \\
\gamma'\left[(\gamma - \gamma_+)(\gamma - \gamma_-) + (\gamma - \gamma_3)(\gamma - \gamma_-) + (\gamma - \gamma_3)(\gamma - \gamma_+)\right] \tag{3.17}
\end{aligned}
$$

and

$$\frac{d}{d\ln x}[1] = \frac{2}{\epsilon}\gamma' + \frac{2+\epsilon}{\epsilon}2\gamma' = \frac{2\epsilon+4}{\epsilon}\gamma' \tag{3.18}$$

implies that

$$
\begin{aligned}
0 &= \gamma''' + \gamma''\left[\left(1 - \frac{2}{\epsilon}\right)(\gamma - \gamma_1) - \frac{2}{\epsilon}(\gamma - \gamma_3) + \frac{2+\epsilon}{\epsilon}\left((\gamma - \gamma_+) + (\gamma + \gamma_-)\right)\right] \\
&\quad - \gamma'\left[\frac{2}{\epsilon}(\gamma - \gamma_1)(\gamma - \gamma_3) + \frac{2+\epsilon}{\epsilon}(\gamma - \gamma_1)\left((\gamma - \gamma_+) + (\gamma - \gamma_-)\right) - \frac{2\epsilon+6}{\epsilon}\right. \\
&\quad \left. + \frac{2(2+\epsilon)}{\epsilon^2}\left((\gamma - \gamma_+)(\gamma - \gamma_-) + (\gamma - \gamma_3)(\gamma - \gamma_-) + (\gamma - \gamma_3)(\gamma - \gamma_+)\right)\right] \\
&\quad - \frac{2(2-\epsilon)(2+\epsilon)}{\epsilon^2}(\gamma - \gamma_1)(\gamma - \gamma_3)(\gamma - \gamma_+)(\gamma - \gamma_-) \tag{3.19}
\end{aligned}
$$

with

$$\gamma_1 = \frac{2(\epsilon - \alpha)}{\epsilon - 2} \ . \tag{3.20}$$

The γ_1 is similar to the β defined in Hansen (2004). The Eq. (3.19) corresponds to Eq. (27) in DM05. We will use this equation to estimate a critical α value in Sec. 3.7.

The master equation, Eq. (3.11), describes how the density profile of the DM structure behaves. One interesting approach to get more insight into the characteristics of DM structures in general is to evaluate the limits of the master equation. For instance one could look at what happens when r goes to infinity and 0, i.e., look at the outer and inner regions of the DM structure. Another approach could be to numerically integrate the master equation from the inner regions and outwards to see how the outer slope would then behave, but this would require that one assumed specific values of the parameters a, b, D, α, and ϵ for a given structure, or knew them by other means. A third rather different approach, is to get insight into DM structures by getting a handle on the unknown parameter space $(a, b, D, \alpha, \epsilon)$. This set of parameters gives the exact relations between the phase space density, the density slope, the velocity anisotropy and the radius of DM structures. The final results of such an approach, might enable us to create input for a general numerical integration of Eq. (3.11) and help the evaluation of the limits. Similar to DM05 it might also be interesting to look for a theoretically defined α_{crit}. Creating so-called flow diagrams of Eq. (3.19) and the limits of it might also provide us with vital information on the behavior and characteristics of DM structures. We will describe these different methods in the following sections starting with getting a handle on the parameter set $(a, b, D, \alpha, \epsilon)$.

3.3   Monte Carlo Code - General Idea

To get more insight into DM structures in general via the unknown parameters in the master equation, Eq. (3.11), we decided to create a Monte Carlo (MC) code which could give us a picture of the preferred values in the parameter space $(a, b, D, \alpha, \epsilon)$. By doing this we hope to be able to give an estimate of the 'golden' parameter values which DM structures seem to prefer. However, if such 'golden' values doesn't seem to exist we might be able to identify relations between the parameters themselves or their dependency on redshift and/or mass of the structure.

The general idea of the MC code is based on the principle/concept of temperature annealing. It is well known from particle physics that if you for instance want to freeze a liquid into a solid, the stability of the solid is very dependent on the way you cool the liquid. To get the most stable solid, the lowering of the temperature should in principle enable every atom to find the best equilibrated position, i.e., the position with the lowest energy before it sticks to the rest of the forming solid. If the temperature is lowered too fast this will not happen and the atom will be caught in a position of relatively high energy, and therefore make the final solid less stable. So the principle is to lower the temperature in such a way that when each atom is positioned in the solid 'mesh' the energy is minimized. When the temperature

reaches a given lower limit, you are left with the most 'energetically favorable' solid. This can be translated into the problem we wanted to solve. What we wanted to do was to find the points in our parameter space preferred by the relations (3.8) and (3.14). A way to measure how well a given data set fits a relation is to compare the LHS with the RHS by the χ^2 method, defined in the usual way as

$$\chi^2 = \Sigma_i \left(\frac{f_1(x_i) - f_2(x_i)}{df_2(x_i)} \right)^2 \tag{3.21}$$

where f_1 and f_2 are the two expressions to be compared and $df_2(x_i)$ is the error in f_2. In this way χ^2 will correspond to the energy of the position of the atoms in the 'freezing-solid' picture. Jumping randomly around in the parameter space gives various χ^2 estimates, which can be held up against each other. The idea is then to lower the 'temperature' to freeze out the data that minimizes χ^2. In our problem it is the allowed step size of each jump that corresponds to the temperature. So by slowly decreasing the size of the jumps, the code will slowly converge towards an optimal set of parameters which minimizes the χ^2 of the two relations. In the next section we will go through some of the crucial points in the code.

3.4   MC Code - Step By Step

In this section we will describe the MC code we wrote to optimize the unknown parameters in Eq. (3.11). As just described the overall idea of the code is to jump around in the parameter space and by that minimize χ^2. Doing this of course involves some practical problems. For instance how to tell the code where to start jumping, how the step size is lowered, how to test whether a given parameter set is 'good' or 'bad' etc. We will describe some of these parts of the code in this section, to give an idea of how we built the code and how it works in practice. The MC code programs and subroutines are described in App. C.

3.4.1   Choosing a Starting Point

First of all the code creates an initial point from which it will start off. Using the random number generator `ran1` from Press et al. (1992) with a seed generated from the computer time, the code creates a random starting point, call it $\overline{X}_{start} = (a_{start}, b_{start}, D_{start}, \alpha_{start}, \epsilon_{start})$ when initiated. This starting point is restricted to lie in an already decided volume in the parameter space. The accepted initial ranges for the five parameters are shown in Table 3.1. From DM05 (and Austin et al. (2005)) we knew in what ballpark the parameters might be. This combined with simple trial and error when testing the code, resulted in the chosen range. The only mathematical limit is the lower bound on the D-parameter. If D was initially chosen lower than around -2.5 the code would get caught in a loop and the calculations would stagnate and the preferred parameters would not converge. Having this initial condition the code now starts to jump around in parameter space, in the search for better χ^2 values.

Parameter	Min	Max
a	-10.0	10.0
b	-10.0	10.0
D	-2.5	12.5
α	0.0	4.0
ϵ	0.0	15.0

Table 3.1: The allowed ranges for the five parameters to be optimized by the MC code.

3.4.2   Jumping

The first jump performed by the code is taken from $\overline{X}_{start}$. Each jump is created randomly by adding a random percentage of the allowed range to the point from which the jump is taken. The jump of each parameter looks like

$$p_{new} = p_{old} + t \, \text{RAN} \, (p_{max} - p_{min}) \, . \tag{3.22}$$

Here RAN is a random number between -0.5 and 0.5 (again generated using `ran1` by Press et al. (1992)) and p indicates one of the parameters and its minimum and maximum values listed in Table 3.1. The t indicates the allowed step size of the jump. It's chosen as initial input to the code and is then lowered each time the χ^2 is improved to make the code converge. Thus t in principle corresponds to the temperature in the 'freezing-solid' picture mentioned above. If one for instance chooses $t = 0.7$, p_{new} will be in between $p_{old} - 0.35(p_{max} - p_{min})$ and $p_{old} + 0.35(p_{max} - p_{min})$. One can by simple selection make sure that this jump is inside the original range if needed. Now for each new point the code tests whether the χ^2 of the relation is improved, i.e., lowered or not.

3.4.3   Testing the 'Goodness' of Points

Testing whether a new point is 'good' or 'bad' is just testing whether the χ^2 has improved or not. The test of χ^2 is done using Eq. (3.21). The code is able to perform two tests. One checking the relation between the phase space density and r in Eq. (3.8) and one checking the γ-$\tilde{\beta}$ relation in Eq. (3.14). We used the data from the simulations in Table 2.1 as input to the relations and therefore had no actual estimate of the errors involved. We chose to use an error of 0.05 in the case of the γ-$\tilde{\beta}$ relation (i.e., $df_{2;\gamma-\tilde{\beta}}(x_i) = 0.05$), and an error of $0.05\frac{\rho}{\sigma_r^3}$ in the phase space density relation. We will look at the effects of these choices (which are insignificant) in Sec. 3.5.1.

Since relation (3.14) is an equality the calculation of χ^2 in this case is straight forward. But as one notices the second relation (3.8) is a bit more complicated, since it is just a proportionality. So not only should the code in this case calculate the χ^2, it should also estimate the preferred normalization of the relation. This is

accomplished by calculating χ^2 for three different normalizations. This gives three points in the $(norm, \chi^2)$ space which can be fitted to a parabola. And then by reading off the minimum of this parabola we are able to get the best set $(norm, \chi^2)_{\text{best}}$ for the given set of data and parameters.

Every time a new χ^2 is smaller than the old one, the code saves this data point, and then uses this point to jump from when determining the next point, and so on. Each time the set of parameters is improved the fraction t is lowered by some factor K, i.e.,

$$t_{new} = K \, t_{old} \qquad \text{for} \qquad K < 1 \tag{3.23}$$

Hence K controls how fast the temperature, i.e., the size of the jump is lowered. We used Ks of the order 0.994-0.998. Since there is a probability that the code can be caught in a local χ^2 minimum, and not in the global one as wanted, we implemented a so-called 'Metropolis'-choice (Metropolis et al., 1953; Hansen, 2003). The idea of such a mechanism is to also let some points with larger values of χ^2 be accepted and be the point from which the code jumps so that the code will be able to jump out of local minima. Performing this choice the code tests whether or not the χ^2 of each rejected point fulfills the criteria

$$\exp\left(-C\frac{\chi^2_{new} - \chi^2_{old}}{t}\right) > \text{ RAN} . \tag{3.24}$$

Here RAN is a random number between zero and unity, C is some positive constant and t is the jump size from Eq. (3.22). If the criteria is fulfilled the point will be stored and used to jump from the next time. When starting from these statistically accepted points the code doesn't lower t. Thus as the size of the jumps decreases the probability for accepting a larger χ^2 also decreases since the LHS becomes smaller. But as the size of the jumps is lowered the difference between the χ^2 values also becomes smaller. Since we want the selection of points to converge, we don't want too many statistically accepted points. This is accomplished by tuning the constant C. The factor C depends on how fast the relation converges, that is how fast χ^2 converges, and the size of the 'cooling factor' K. When optimizing relation (3.8) $C = 20$, wheres $C = 1/40$ when optimizing relation (3.14).

Now looping over the jump and testing sequences the code produces a datafile containing the converging parameters, the χ^2, and the normalization factor (when fitting to the phase space density relation). Plotting these files give plots like those in Fig. 3.1. The characteristic parabola form in the top row plots clearly indicates the procedure of the MC code, i.e., a convergence towards a minimum in χ^2. Extracting the lowest χ^2 and the corresponding parameters from the data files, gives the set of parameters that makes the data fit the relations (3.8) and (3.14) in the best way, i.e., $(a_{\text{best}}, b_{\text{best}}, D_{\text{best}}, \alpha_{\text{best}}, \epsilon_{\text{best}})$.
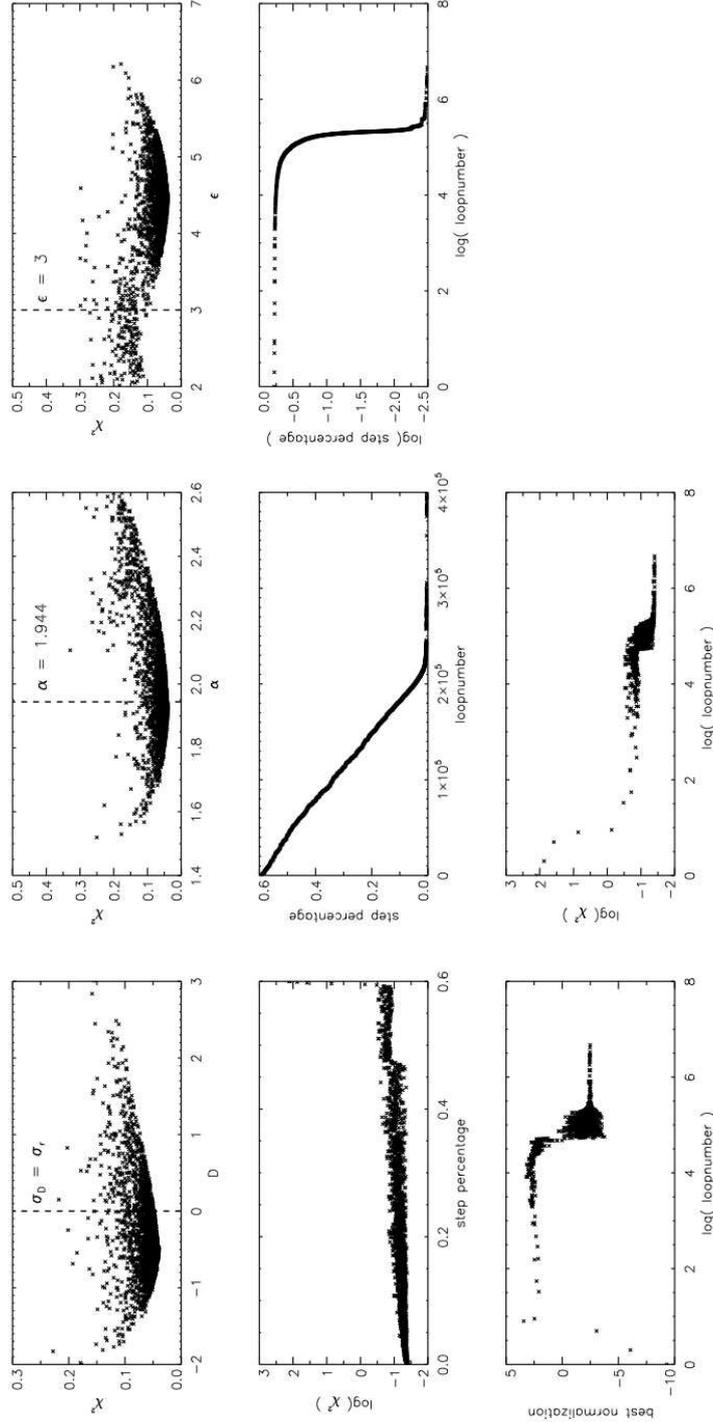
Figure 3.1: An example of the output from running the MC code. Here we have shown the result when running the code optimizing relation (3.8) with the 'Via Lactea' simulation by Diemand et al. (2007). The parabola shapes (top row) clearly illustrate how the code converge towards a preferred value of D, α and ϵ from relation (3.8). In the case of the ϵ parameter we also see the contour/indication of a local minimum around $\epsilon = 2$ which the code have jumped out of to reach lower χ^2 values at $\epsilon \sim 4.5$. The sizes of the jumps are here represented by a 'step percentage' (in principle the t from Eq. (3.22)) which is lowered according to Eq. (3.23) as the code is looping over the jumping phase. It can also be seen that as the step percentage, i.e., t is getting smaller the χ^2 is minimized. Furthermore we see how the norm is converging towards the value -2.45.

3.5   Running MC-code with Recent Cosmological Simulations

Now that we have a code which can optimize the parameters of the master equation, Eq. (3.11), we are able to start plugging in data to get results. The idea is to run the code with various numerical simulations as input, to get an idea of what set of parameters the simulated DM structures favor. As input to the code we used the data files from the simulations described in Sec. 2.6.1. Besides these simulations, which are all at a redshift $z = 0$, we also ran the code with data of some structures at redshifts $z = 0.2, 0.5$ and 1.0 to see if there is any relation between the preferred parameter values and the redshift at which the data is extracted from the simulations (see Sec. 3.5.3). This might also give an indication of whether the amount of relaxation of the structures influences the preferred set of parameters or not.

To make sure that the input structures at $z = 0$ were all (more or less) in dynamical equilibrium we cut off the outermost unrelaxed points in each structure by hand. A good indicator of how relaxed a given structure is, is the density slope γ defined in Eq. (3.2). Since a structure which is not fully relaxed hasn't had time to come into dynamical equilibrium the structure will contain over- and under-densities which will clearly show as 'disturbances' in the otherwise quite monotonic density slope profile. We also removed some of the innermost bins, since some of these might not be trustworthy because of the lack of numerical resolution or numerical softening in the innermost dense regions. We have shown an example of how the structures were cut in Fig. 3.2.

Before we made these cut-offs we tested how it influenced the final optimized parameters. First we concentrated on the difference between cutting the structures only in the outer part, and both in the inner and the outer part. Running the part of the code which uses Eq. (3.8) to estimate D, α and ϵ, with all the galaxy data files, extracting the relevant parameters and plotting them to get an overview, results in Fig. 3.4. Similar figures for the cluster data are shown in Fig. 3.5. Here it is clear that the differences in the estimated parameters are minimal. We have quantified this claim in Table 3.2 and Fig. 3.3.
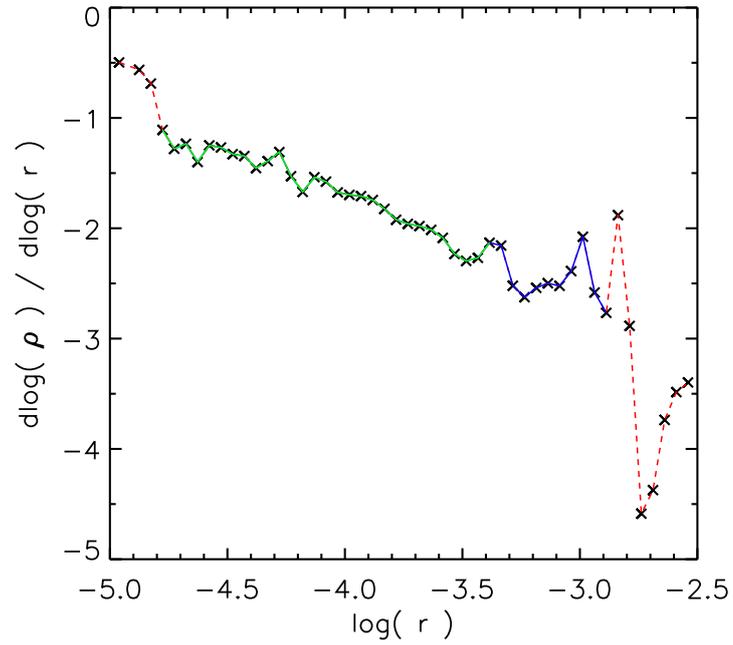
Figure 3.2: An example of how the structures were cut off to ensure trustable dynamically relaxed data. In the figure the profile of the simulation G0.W1 is shown. The red (dashed) line is the whole structure. The blue and green parts combined (full line) is the part of the structure used for calculations, and the green part alone is the part of the structure left when cutting roughly 25 percent extra in the outer part. For further discussion of the cuts please refer to the text.

Structures cut in the inner and outer parts

See Table 3.3.

Structures cut only in the outer parts

Simulation	a_{best}	b_{best}	D_{best}	α_{best}	ϵ_{best}	$norm_{best}$	$\Delta a_{o,io}$	$\Delta b_{o,io}$	$\Delta D_{o,io}$	$\Delta \alpha_{o,io}$	$\Delta \epsilon_{o,io}$	$\Delta norm_{o,io}$
'Via Lactea'	0.77	-0.25	-0.87	1.83	4.47	-2.90	-0.10	-0.12	-0.37	-0.02	-0.003	-0.45
G0.W1	0.83	-0.19	-0.67	1.81	2.96	-1.16	0.05	0.01	-0.07	-0.01	0.11	-0.23
G1.W1	1.00	0.01	0.08	1.90	2.79	-0.49	-0.02	-0.02	-0.10	-0.006	0.03	-0.10
G1.W3	1.08	0.09	0.40	2.03	3.08	-0.22	0.01	0.001	-0.03	-0.01	-0.004	-0.02
G2.W1	1.01	0.93e-3	-0.04	1.87	2.56	-0.27	0.003	0.4e-3	-0.02	-0.08	0.06	-0.12
G2.W3	0.87	-0.14	-0.38	1.83	3.32	-1.49	-0.08	-0.09	-0.23	-0.01	-0.002	-0.34
G3.W1	-0.71	-1.53	-1.45	1.68	1.44	0.10	1.37	0.76	0.04	-0.006	0.14	-0.23
G4.W3	0.32	-0.58	-0.86	1.78	2.32	-0.54	0.11	0.07	0.04	-0.10	0.11	-0.17
C1.W3	0.94	-0.16	-1.24	1.61	1.24	0.20	-0.09	-0.005	0.26	0.004	0.37	-0.22
C2.W1	0.78	-0.24	-0.96	1.80	2.97	-0.36	-0.03	-0.06	-0.028	-0.08	0.04	-0.27
C3.W1	0.88	-0.95	-0.68	1.83	2.98	-0.31	0.003	-0.03	-0.23	-0.04	0.40	-0.38
C_{HR}.W3	0.64	-0.36	-1.04	1.71	2.52	-0.53	-0.04	-0.06	-0.19	-0.04	0.04	-0.18

Structures cut in the inner and cut extra in the outer parts

Simulation	a_{best}	b_{best}	D_{best}	α_{best}	ϵ_{best}	$norm_{best}$	$\Delta a_{io,iox}$	$\Delta b_{io,iox}$	$\Delta D_{io,iox}$	$\Delta \alpha_{io,iox}$	$\Delta \epsilon_{io,iox}$	$\Delta norm_{io,iox}$
G0.W1	0.86	-0.12	-0.34	1.84	2.44	-0.35	0.08	0.08	0.25	0.007	-0.42	0.59
G1.W1	1.04	0.05	0.22	1.89	2.61	-0.26	0.02	0.02	0.04	-0.01	-0.15	0.13
G1.W3	0.74	-0.23	-0.57	1.83	2.36	-0.24	-0.33	-0.32	-1.00	-0.21	-0.72	-0.038
G2.W1	1.04	-0.003	-0.32	1.85	1.76	0.56	0.03	-0.004	-0.30	-0.03	-0.73	0.72
G2.W3	0.96	-0.02	-0.09	1.95	3.80	-1.61	0.03	0.03	0.06	0.04	0.48	-0.46
G3.W1	0.34	-0.55	-1.05	1.76	1.75	0.12	2.42	1.74	0.43	0.73	0.45	-0.22
G4.W3	0.32	-0.61	-1.09	1.74	2.44	-0.91	0.12	0.04	-0.19	-0.05	0.23	-0.54

Table 3.2: The optimized parameters for the simulations at $z = 0$, where the structures have been cut only in the outer part, in the inner and outer part and in the inner part with even more ($\sim$ 25 percent of the remaining structure) removed in the outer part. The structures were run with an error corresponding to $0.05 \frac{\rho}{\sigma_r^3}$ and 0.05 for the phase space density and velocity anisotropy parts of the MC code respectively. The Δ subscripts o,io and io,iox refers to the differences between the structures which were cut in the outer and outer+inner region and the structures which were cut in the inner+outer and inner+extra in the outer region respectively.
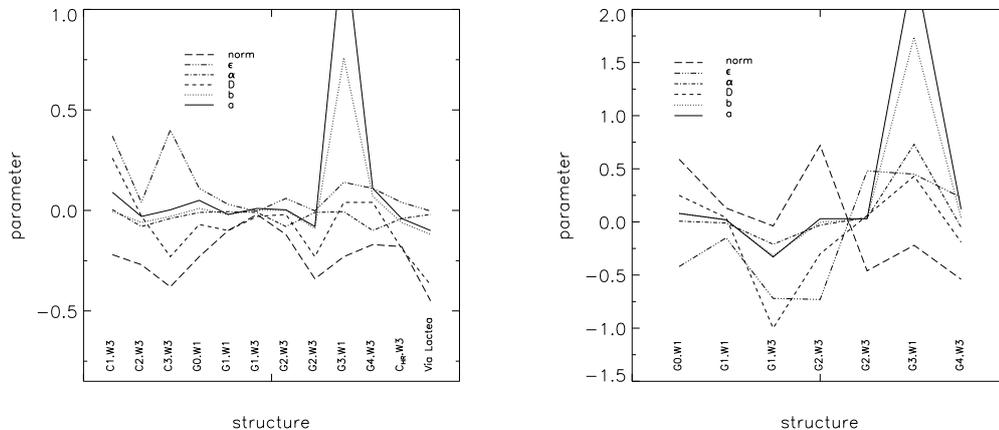
(a) *The Δ values between structures cut only in the outer part and both in the inner and outer parts ($\Delta_{o,io}$ in Table 3.2).*

(b) *The Δ values between structures cut in the inner and outer part and cut in the inner and extra 25 percent in the outer parts ($\Delta_{io,iox}$ in Table 3.2).*

Figure 3.3: The differences in the Δ values from Table 3.2 for the 5 parameters for different cut structures. If one of the lines was significantly above or below 0 this would indicate a systematic difference between the optimized parameters for the two different cut structures used to calculate the Δ values. However, all the Δ values for the different parameters scatter around 0, indicating that no clear effect of cutting the structures in different ways is visible.

Since the dynamical time $t_{\mathrm{dyn}} \sim 1/\sqrt{\rho G}$ it is no surprise that we don't see a significant difference in the obtained parameters when removing the innermost bins, since here the structure would, because of the relatively high density, have had plenty of time to get dynamically relaxed. On the other hand it might be crucial how large an amount of the structures we cut in the outer parts. We therefore took the structures which were both cut 'trustable' in the inner and outer part, and removed even more of the outer part (∼25 percent of each remaining structure was removed. See Fig. 3.2), to see whether this could bias our final conclusions or not. Again we saw that there is no clear indication that the extra cut of the structures make the parameters change significantly. In Table 3.2 we have listed the parameters for the different cut structures. In Table 3.2 we have also listed some Δs, which are just the difference between the estimated parameters for structures cut in two different ways. Plotting these values for each structure in Fig. 3.3 shows that the change in the parameters were more or less random, rather than showing a clear trend. If the parameters should either increase or decrease as a function of the various cuts, the majority of the points for each parameter should lie above or beneath 0, and not scatter around 0 as they do in Fig. 3.3. One might argue that some of the parameters show a (small) trend. For instance all the $\Delta\alpha_{o,io}$ values are below 0, but this can't be considered a significant trend because of the relatively small values. Thus the effect

of cutting the structures seems random. We therefore use the structures which we have cut in the inner and outer parts in the rest of the work, since these structures are the most 'physical' in the sense that they have a rather monotonic density slope throughout the whole structure. The obtained parameters for these structures are listed in Table 3.3.

3.5.1 The Choice of Error

Another thing that might affect the results from the MC code is the choice of error, $df_2(x_i)$, in Eq. (3.21). Since we are calculating the χ^2 between two assumed mathematical relations which 'error free' simulations are plugged into, we don't have any exact errors to use in the χ^2 calculations. As mentioned we solved this problem by using the 'static' error 0.05 for the γ-$\tilde{\beta}$ relation and $0.05\frac{\rho}{\sigma_r^3}$ in the phase space density relation. Before we did that we tested various error estimates to see how much this influenced the final results. In general we saw that the size of the error doesn't seem to affect the final results. In the $\frac{\rho}{\sigma_D^\epsilon}$ case it was rather the assumed values of ϵ and D. We tested relation (3.8) with different errors (see caption to Fig. 3.6) for various structures. Running the code with structure G0.W1 gave the plot shown in Fig. 3.6. The optimized values in this figure is shown as a function of the pre-factor and the chosen error in Fig. 3.7. In both figures wee see that the final estimate of the given parameter is more or less unaffected by the choice of error, in fact the variations are of the order a few percent and less. The χ^2 is determined by the pre-factor of the given error. The only thing that influences the estimated parameter, even though this effect is insignificant, is the choice of ϵ and D. This is illustrated in Fig. 3.7 by the fact that the black line in the top row is more 'stable' compared to the other lines where either D or ϵ (or both) have been fixed, i.e., the scatter in the bottom row plots is smallest for the ρ/σ_D^ϵ error. Thus we can conclude that choosing the error $0.05\frac{\rho}{\sigma_r^3}$ doesn't affect the estimates of the parameters significantly.
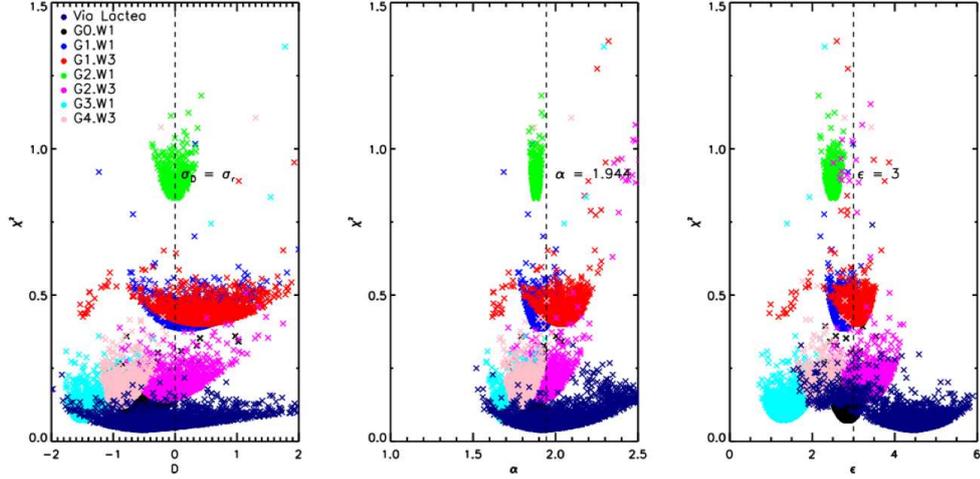
(a) *Structures cut both in the inner and outer part.*
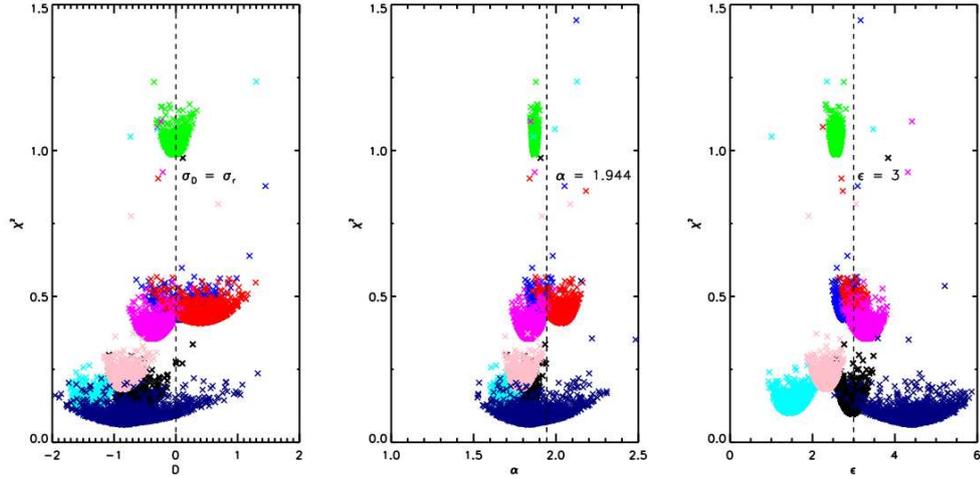
(b) *Structures only cut in the outer part.*

Figure 3.4: The optimized parameters from relation (3.8) calculated by the MC code for the galaxy sized objects. The dotted vertical lines correspond to the isotropic values from Dehnen & McLaughlin (2005), i.e., $D = 0$, $\alpha = \alpha_{crit} = 1.9\overline{4}$ and $\epsilon = 3$. The colors navy, black, blue, red, green, magenta, cyan and pink corresponds to the structures 'Via Lactea', G0.W1, G1.W1, G1.W3, G2.W1, G2.W3, G3.W1 and G4.W3 respectively.
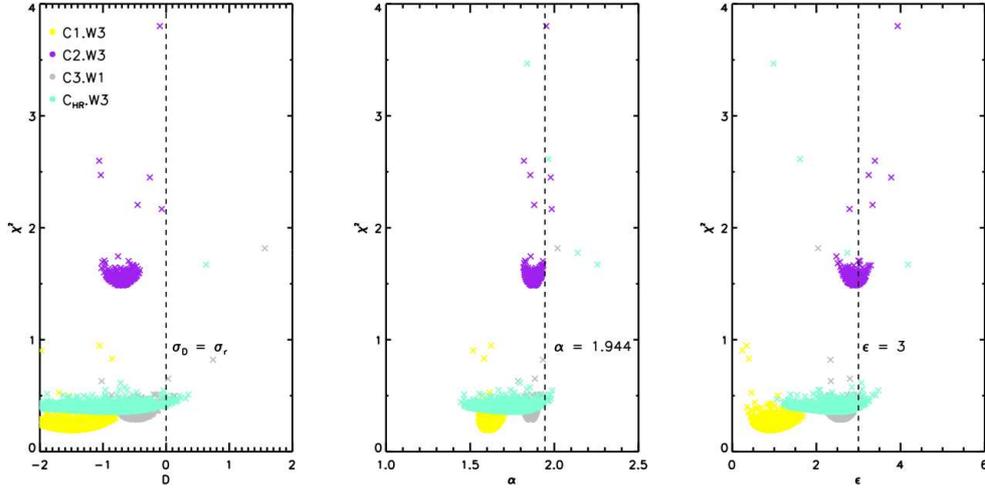
(a) *Structures cut both in the inner and outer part.*
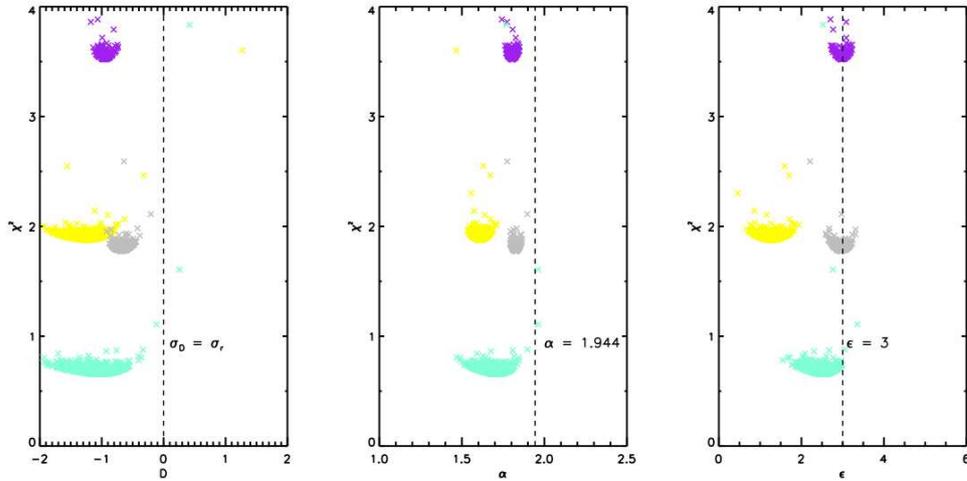
(b) *Structures only cut in the outer part.*

Figure 3.5: The same figure as Fig. 3.4 now showing the simulated cluster sized structures. Again the dotted vertical lines correspond to the isotropic values from Dehnen & McLaughlin (2005). The colors yellow, purple, grey and aqua correspond to the structures C1.W3, C2.W3, C3.W1 and C_{HR}.W3 respectively.
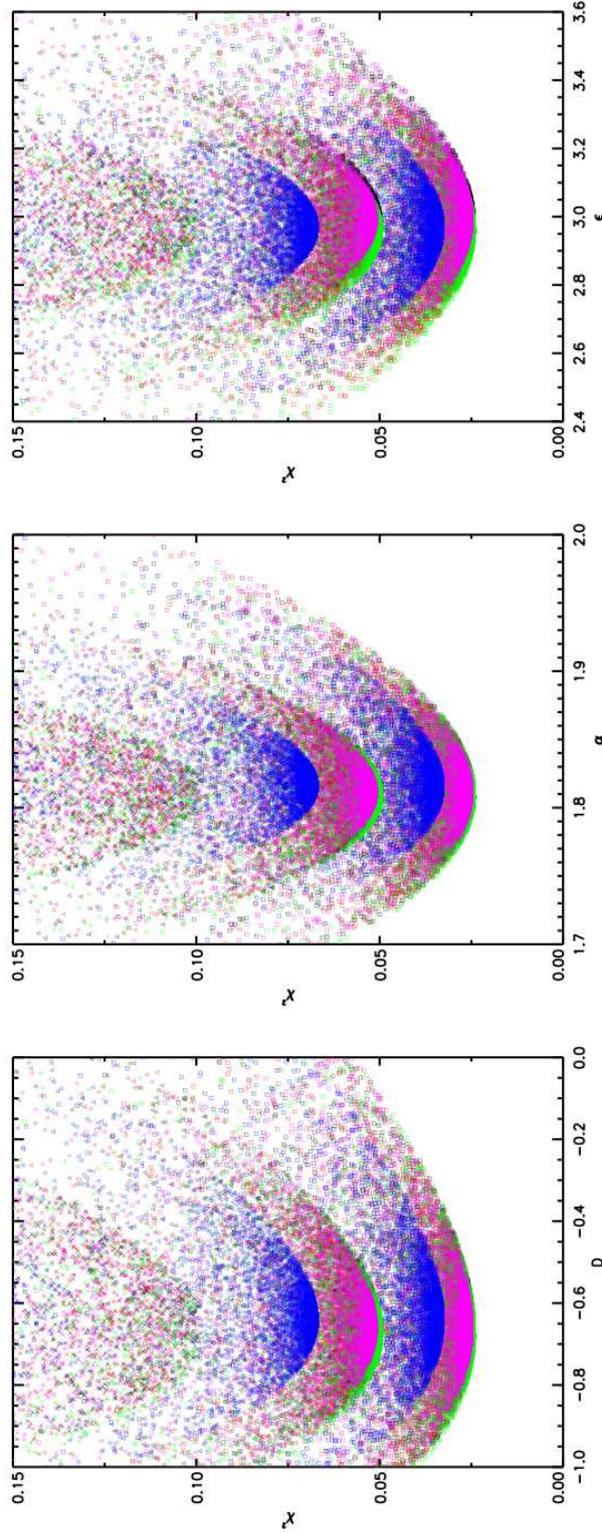
Figure 3.6: An example of the result using different errors when calculating χ^2 in the MC code. This plot is created by optimizing the structure G0.W1. We tested five different errors; $\frac{\rho}{\sigma_D^\epsilon}$ (black symbols), $\frac{\rho}{\sigma_r^3}$ (red symbols), $\frac{\rho}{\sigma_D^3}$ (green symbols), $\frac{\rho}{\sigma_r^\epsilon}$ (magenta symbols) and $r^{-\alpha}$ (blue symbols) in three different sizes; 0.05 (crosses), 0.07 (triangles) and 0.10 (squares). Thus the magenta squares (lower part of the plots) show the result from running the MC code with the error $0.10\frac{\rho}{\sigma_r^\epsilon}$. As can be seen the estimated parameter is more or less the same for all runs. The only thing that seems to influence the size of the estimated parameter is whether D and ϵ are constants or vary with the structure. The size of the χ^2 values depend on the pre-factor of the errors. The exact values of the estimated parameters for each error can be seen in Fig. 3.7.
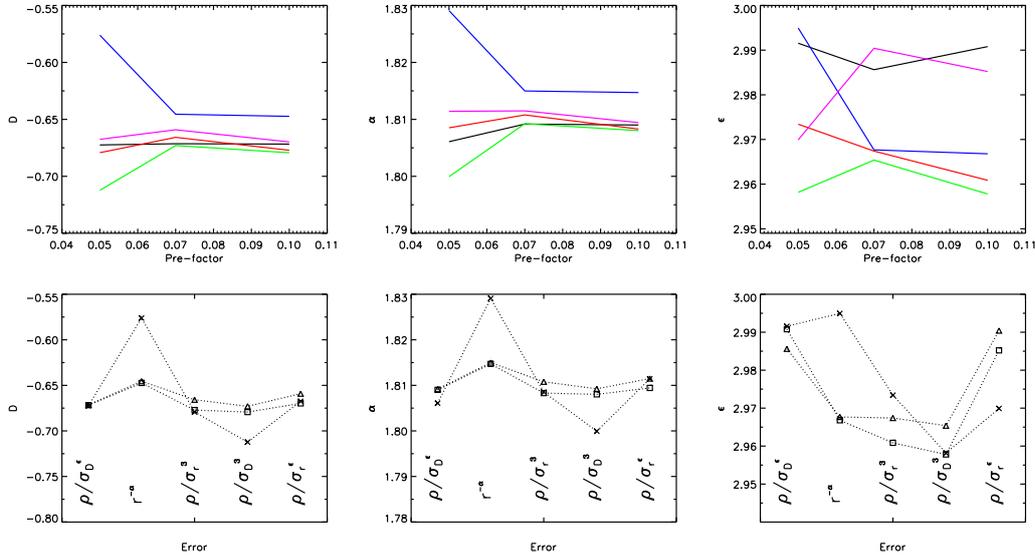
Figure 3.7: The estimated values of D, α and ε as a function of the different tried errors for the structure G0.W1. The colors in the top row and the symbols in the bottom row corresponds to the ones used in Fig. 3.6. The top row shows the evolution if you fix the 'error-kind' and change the pre-factor, and the bottom row shows the evolution when fixing the pre-factor and changing the 'error-kind'. We see (even more clearly than in Fig. 3.6) that the estimated parameters don't depend on the chosen error. In fact the difference in the estimated values is of the order 8, 1 and 1 percent for D, α and ε respectively. The scatter in the top and bottom rows are the same, since the plotted values are the same distributed/connected differently.

Now that we have an estimate of the effects of the chosen error and the cut in the structures on the estimated parameters, we can proceed to interpret the results from the MC code. As mentioned we used the structures which were both cut in the inner and outer regions. Running the part of the code using Eq. (3.8) for all the structures results in Figs. 3.4a and 3.5a. In these figures we have indicated the 'golden' values preferred by DM05 ($D = 0$, $\alpha = 1.9\overline{4}$ and $\epsilon = 3$) with dotted vertical lines for comparison. It is clear from these figures that the structures don't prefer the same value for the different parameters. In fact our data doesn't prefer single values but rather seems to pick different values for different structures. When running the second part of the code, using the relation in Eq. (3.14) to optimize the a and b values, we therefore used the different preferred values for D as input, instead of one universal D value. We furthermore needed to fix the D 'by hand' to avoid/ignore the solution $D = 0$, $a = 1$ and $b = 0$, since this solution is of no physical interest as will become clear in the next section. The results of these runs are shown in Fig. 3.8. We now had an optimized parameter set $(a_{\text{best}}, b_{\text{best}}, D_{\text{best}}, \alpha_{\text{best}}, \epsilon_{\text{best}})$ for each structure. It is these values which are listed in Table 3.3.

Simulation	z	a_{best}	b_{best}	D_{best}	α_{best}	ϵ_{best}	$norm_{\text{best}}$	α_{crit}
'Via Lactea'*	0.0	0.88	-0.13	-0.51	1.93	4.47	-2.45	1.16
G0.W1*	0.0	0.78	-0.21	-0.60	1.83	2.86	-0.93	2.32
G0.W1	0.2	0.90	-0.11	-0.43	1.85	2.76	-0.39	2.53
G0.W1	0.5	0.42	-0.51	-0.90	1.72	2.59	-0.40	2.30
G0.W1	1.0	0.87	-0.14	-0.56	1.83	2.95	0.15	2.38
G1.W1*	0.0	1.02	0.03	0.18	1.91	2.75	-0.39	0.90
G1.W1†	0.2	0.23	-0.64	-1.10	1.64	1.41	0.31	2.22
G1.W1	0.5	0.95	-0.06	-0.30	1.87	2.75	-0.02	2.95
G1.W1†	1.0	1.02	0.08	0.58	1.83	2.49	0.78	1.03
G1.W3*	0.0	1.07	0.09	0.43	2.04	3.08	-0.20	2.53
G2.W1*	0.0	1.00	0.56e-3	-0.02	1.88	2.50	-0.15	-232
G2.W1	0.2	0.82	-0.22	-0.78	1.79	1.67	0.62	2.78
G2.W1‡	0.5	-	-	-7.37	1.63	0.20	1.85	-
G2.W1†	1.0	0.99	0.04	0.46	1.70	1.25	1.44	-4.71
G2.W3*	0.0	0.95	-0.05	-0.15	1.91	3.32	-1.15	0.77
G3.W1*	0.0	-2.08	-2.29	-1.49	1.69	1.30	0.34	1.96
G3.W1	0.2	-1.63	-1.90	-1.38	1.72	1.43	0.52	1.96
G3.W1	0.5	-0.29	-0.98	-1.22	1.76	1.76	0.62	2.03
G3.W1†	1.0	0.48	-0.46	-1.07	1.76	1.88	0.87	2.11
G4.W3*	0.0	0.20	-0.65	-0.90	1.78	2.21	-0.37	2.28
Mean$_{\text{galaxies}}$	0.0	0.35	-0.40	-0.38	1.87	2.81	-0.66	1.70(-27.6)
Mean$_{\text{galaxies}}$	all	0.45	-0.43	-0.82	1.80	2.28	0.05	-
C1.W3*	0.0	1.03	-0.16	-1.50	1.61	0.90	0.43	3.03
C2.W1*	0.0	0.81	-0.18	-0.68	1.88	2.93	-0.08	2.41
C3.W1*	0.0	0.88	-0.12	-0.45	1.86	2.58	0.07	2.70
C$_{HR}$.W3*	0.0	0.68	-0.31	-0.86	1.75	2.48	-0.35	2.44
Mean$_{\text{clusters}}$	0.0	0.85	-0.19	-0.87	1.78	2.22	0.02	2.64
Mean$_{\text{total}}$	0.0	0.57	-0.36	-0.55	1.84	2.62	-0.44	2.05(-17.5)
Mean$_{\text{total}}$	all	0.52	-0.39	-0.83	1.80	2.27	0.05	-

*Table 3.3: The optimized/best values achieved from running the MC code described in the text with various simulations of DM structures. The structures were all cut in the outer and inner part (see text for further info on the reasons to cut the structures). The simulations with * were used in the section on the investigation of the rotation of DM structures, and are listed with some characteristics in Table 2.1. The simulations with $z \neq 0$ are extracted snapshots of the corresponding *-structures. The calculated mean of the estimated α_{crit} values for all the structures is given in parenthesis, the other number is the mean, where the outlier G2.W1 is excluded. All the runs are with $t = 0.6$ (see Eq. (3.22)) except the ones marked with † which have $t = 0.3$. The ‡ simulation can't be trusted, since the code wasn't able to run it if we cut off all the unrelaxed parts (most of the structure). This is probably due to a recent major merger.*
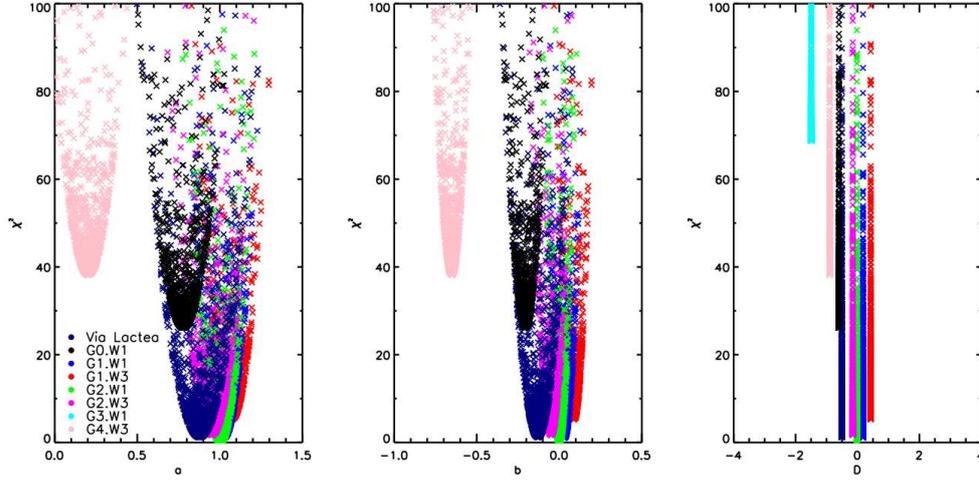
(a) *Galaxy sized structures.*
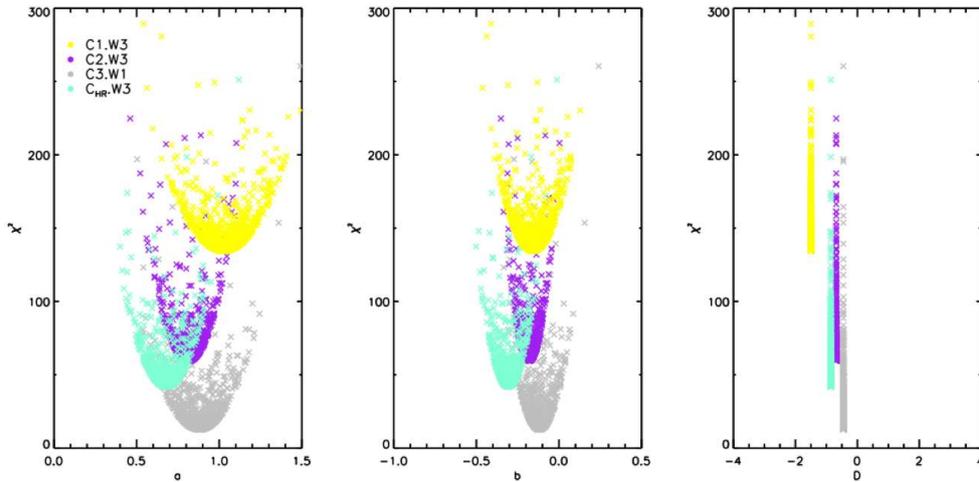
(b) *Cluster sized structures.*

Figure 3.8: The results from running the MC code optimizing Eq. (3.14) for the galaxy sized structures and the cluster sized structures which were both cut in the inner and outer regions. The colors represent the same structures as in Figs. 3.4 and 3.5. The cyan and pink galaxy and the yellow cluster, i.e., G3.W1, G4.W3 and C1.W3 are special in the sense that their χ^2 values have been subtracted 10340, 430 and 1300 respectively in order to drag them into the plotted ranges. However, the a and b values of G3.W1 are still outside the plotted ranges. See Table 3.3 for these values.

3.5.2 Interpreting the $(a_{\mathbf{best}}, b_{\mathbf{best}}, D_{\mathbf{best}}, \alpha_{\mathbf{best}}, \epsilon_{\mathbf{best}})$ Data Sets

The obtained parameters indicate that the assumption of $\epsilon = 3$ is a rather crude one (see right panel in Fig. 3.4). The error on the estimated values from the MC code is composed of several factors, but are in principle indicated by the curvature of the parabolic appearance of the data in the Figs. 3.4, 3.5 and 3.8. As discussed above the precision of the estimated parameters is governed by systematic errors like the choice of error in calculating the χ^2 values and cutting of the structures at the given points. Furthermore the choice of the relative size of the error in χ^2 (0.05, 0.07, 0.10) inflicts the error estimates. Thus it is only part of the error in the estimated parameters that refers to the actual structure, i.e., how well the parameters are estimated from the relations. Nevertheless the errors on the estimated parameters aren't so large that we can conclude that $\epsilon = 3$ is preferred, even though the estimated values are situated around 3.

As is also seen the Ds indicate other values than the $D = 0$ used by DM05 (see left panel in Fig. 3.4). The majority of the structures indicate that D might be smaller than 0, indicating that the velocity anisotropy of the phase space density is composed of both radial and tangential components. This illustrates the importance of extending the approach by DM05, as we have done in Sec. 3.2. The estimated value of α for the various structures show a similar picture, even though they seem to cluster a bit more around the empirically inferred/preferred value (for the isotropic case) 1.9 ± 0.05 (DM05). Concluding anything from the values of a and b is tempting but not justifiable, as will become clear in a moment

So in general we might conclude that our runs seem to at least agree with the results from DM05 regarding the parameters D, α and ϵ, even though we don't see any indication of 'golden' parameter values.

An obvious next step is to look for a connection between the calculated values of each parameter, since they don't seem to converge towards single 'golden' values. The easiest way to do that is to plot the various parameters against each other to look for any characteristic correlations. We have shown such plots for the various parameters in Fig. 3.9.

From Fig. 3.9c it is obvious that a and b are strongly correlated. In fact the relation is so strong that it indicates that something is wrong. What we see here is the MC code still trying to converge towards the trivial solution $a = 1$, $b = 0$ and $D = 0$ as mentioned earlier, i.e., making Eq. (3.14) to the relation $1 = 1$. This will of course minimize the χ^2 value as wanted, but it has no physical meaning. Thus what is happening is that the larger the fixed D the larger the χ^2, which then make a and b strongly related. This fact is clearly seen in Fig. 3.10 where we have plotted χ^2 as a function of D. Here it's obvious that to minimize χ^2 the code converges towards the solution that makes $D = 0$, which necessarily makes $a = 1$ and $b = 0$. Thus any conclusions and calculations using a and b should at best be used with care.

Instead Fig. 3.9a, showing the possible correlations between the three parameters in Eq. (3.8), is much more interesting. The figure indicates that the parameters are all correlated. The magenta vertical and horizontal lines in the plots indicate the
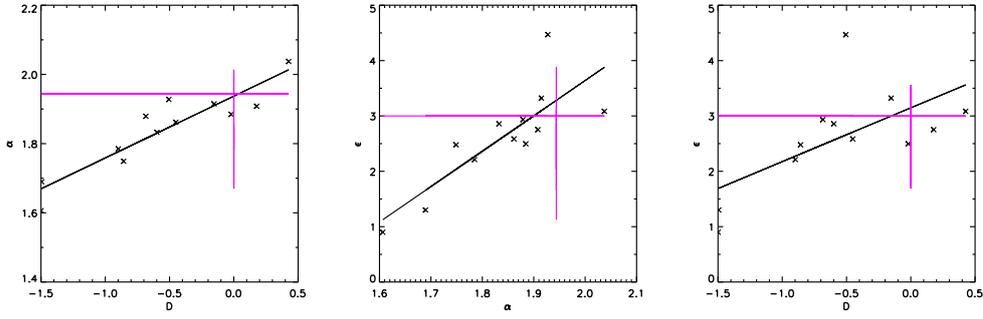
(a) *Correlations between the optimized values from relation (3.8).*
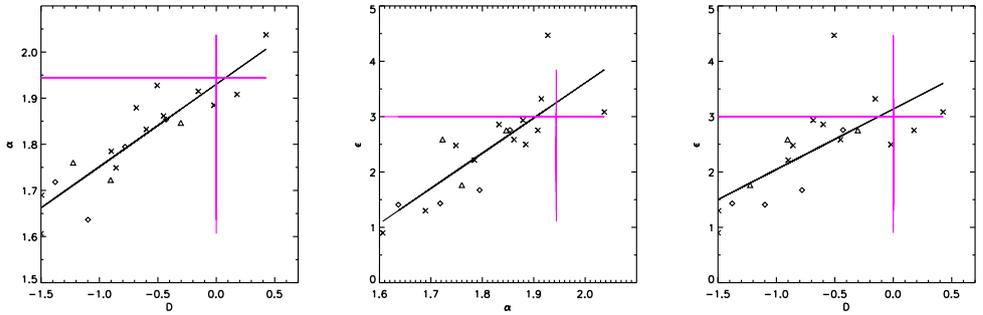
(b) *Correlations between the optimized values from relation (3.8) for all structures at $z = 0$ and the galaxy sized WMAP1 structures at $z = 0.2$ and 0.5.*
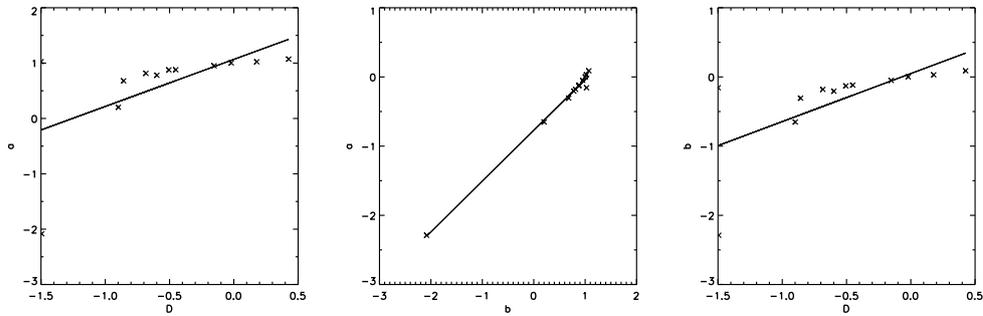
(c) *Correlations between the optimized values from relation (3.14).*

Figure 3.9: The optimized values for the simulated structures plotted against each other. The (magenta) vertical and horizontal lines in Figs. 3.9a and 3.9b which cross indicate the values preferred in Dehnen & McLaughlin (2005). The linear fits (black lines) from Fig. 3.9a are written for the D cases in Eqs. (3.25) and (3.26). The relation between α and ϵ is given by $\epsilon = (6.39 \pm 1.44) \times (\alpha - 1.94) + (3.26 \pm 3.85)$. Fig. 3.9b is the same as Fig. 3.9a where the optimized parameters for the galaxy sized WMAP1 structures at redshift 0.2 and 0.5 have been added (except for the G2.W1 outlier at $z = 0.5$). Diamonds, and triangles correspond to $z = 0.2$ and $z = 0.5$ respectively. The linear fits in Figs. 3.9a and 3.9b are not the same (fitted to data for $z = 0$ and $z = 0, 0.2, 0.5$ respectively) but we see that the trend is more or less the same when comparing the data at different redshifts.
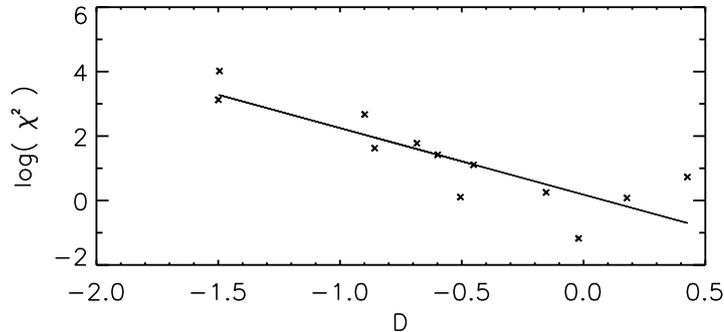
Figure 3.10: The artificial relation between the χ^2 values for the optimization of Eq. (3.14) and the D parameter for each simulated structure. As explained in the text, it seems that the code tries to optimize the relation by making $D = 0$ even-though we fixed the D values to avoid this. This gives that the further from 0 D is fixed the higher the χ^2 value becomes.

values preferred by DM05. We realize that the lines fitted to the data points from the MC code go through (more or less) the 'golden' values of the parameters suggested by DM05. This might indicate that if you choose $D = 0$ you will always get $\alpha \sim 1.9$ and $\epsilon \sim 3$, so the fact that DM05 get these values as a nice fit for $\frac{\rho}{\sigma_r^\epsilon}$ is not a surprise, but a consequence of the relations between the parameters shown in Fig. 3.9a. Writing down these obtained relations in general for all D, α and ϵ gives that

$$\alpha = (0.19 \pm 0.02) \times D + (1.94 \pm 0.02) \qquad (3.25)$$

$$\epsilon = (0.97 \pm 0.37) \times D + (3.15 \pm 0.29) \qquad (3.26)$$

Thus if we forced $D = 0$ we would have $\alpha = 1.94 \pm 0.02$ and $\epsilon = 3.15 \pm 0.29$, which is indeed in correspondence with the work by DM05. If we on the other hand look at a general phase space density, i.e., $\frac{\rho}{\sigma_D^\epsilon}$ for $D \neq 0$ we get the results listed in Table 3.4. Thus if one knows the appearance of the velocity dispersion which contributes to the phase space density, it is straightforward to write down the exact proportionality in Eq. (3.8) by using Eqs. (3.25) and (3.26).

3.5.3   Redshift and Mass Dependence

Having shown that the parameters are strongly correlated for DM structures at $z = 0$, it would be interesting to see whether these relations were affected by the redshift at which the structures were extracted from the simulations. For the WMAP1 galaxy simulations we also had data for the $z = 0.2$, $z = 0.5$ and $z = 1.0$ profiles. Extracting the structures at higher redshift would of course give the structures less time to relax. Hence the density slope profiles were much more non-monotonic for the structures

D	Phase Space Density	α	ϵ
1	$\dfrac{\rho}{\frac{1}{2}\left(\sigma_\phi^2+\sigma_\theta^2\right)^{\epsilon/2}}$	2.13 ± 0.03	4.12 ± 0.47
0*	$\dfrac{\rho}{\sigma_r^\epsilon}$	1.94 ± 0.02	3.15 ± 0.29
-1	$\dfrac{\rho}{\left(2\sigma_r^2-\frac{1}{2}\left(\sigma_\phi^2+\sigma_\theta^2\right)\right)^{\epsilon/2}}$	1.75 ± 0.03	2.18 ± 0.47
$-\frac{2}{3}$	$\dfrac{\rho}{\left(\frac{1}{3}\left(\sigma_r^2+\sigma_\phi^2+\sigma_\theta^2\right)\right)^{\epsilon/2}}$	1.81 ± 0.02	2.50 ± 0.38

*Table 3.4: The results for different phase space densities using the relations in Eqs. (3.25) and (3.26). The phase space densities are extracted from Eq. (3.6) using the corresponding D values. The case marked with an * is the one used in DM05.*

with $z \neq 0$. This lack of dynamical equilibrium resulted in a much larger amount of points removed in the outer parts of these structures before they were plugged into the MC code. Therefore the conclusions from dealing with $z \neq 0$ structures, should be taken with some caution, since the equations applied to the structures are thought to fit structures in dynamical equilibrium, in which some of the $z \neq 0$ structures were definitely not. Having this in mind, we ran the code with these structures and got the results listed (together with the $z = 0$ structures) in Table 3.3. To see whether there were any trends visible we plotted the parameters as a function of redshift for the different structures. This plot is shown in Fig. 3.11.
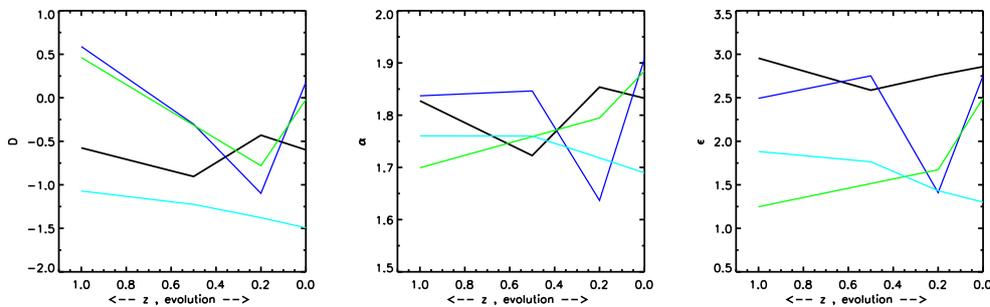
Figure 3.11: The evolution of the 3 parameters fitted with relation (3.8) as a function of redshift (values are listed in Table 3.3). We only had $z \neq 0$ for the WMAP1 galaxy structures which are the ones plotted here. The black, blue, green and cyan lines correspond to the structures G0.W1, G1.W1, G2.W1 and G3.W1 respectively (as in Fig. 3.4). The structure G2.W1 is plotted without the untrustworthy data point $z = 0.5$. We see that no general evolution of D, α and ϵ seems to be detectable.

As can be seen the only structure that shows any trend as a function of redshift is the G3.W1 structure (cyan line) where the size of the parameters seems to grow as the redshift increases. Nevertheless a general trend for all structures doesn't seem to exist. Since the estimated parameters are more or less constant as a function of

redshift this indicates that Eqs. (3.25) and (3.26) might also hold for structures at redshifts larger than 0 (still having in mind that the $z \neq 0$ structures are not as relaxed as the $z = 0$ structures).

Similarly it would also be interesting to see whether the parameters depend on the mass of the structure or not. We have plotted the parameters D, α and ϵ as a function of the virial mass of the structures in Fig. 3.12. We see that the parameters show a slight decrease with increasing mass. However, because of the relatively large scatter and no exact estimates of the errors in the obtained values we can't conclude whether this mass dependency is of physical origin or not.
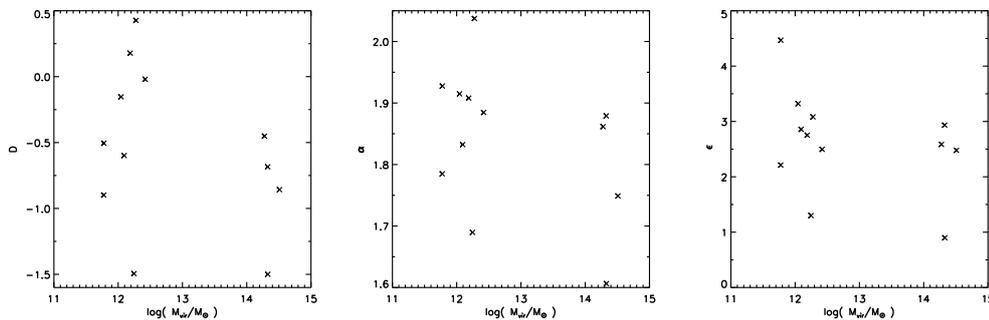
Figure 3.12: The evolution of the parameters D, α and ϵ as a function of the virial mass of the structures (parameters are listed in Table 3.3 and virial masses in Table 2.1). Due to the large scatter and no exact estimates of the errors we can't conclude whether a trend is present or not.

3.5.4   Conclusion on the Monte Carlo Runs

We have now optimized the unknowns in the master equation via the MC code. To sum up the conclusions we have shown that the choice of error when calculating χ^2 only affects the results very little, and we have therefore used a 'static' error in our calculations. Furthermore we have shown that cuts in the structures don't make the final results change significantly. We have performed all the calculations using structures which were cut in the inner and outer region, so that they could be trusted to be in dynamical equilibrium. The hope was to estimate the sizes of the potential 'golden' parameter values of DM structures. However, our results indicate that such values don't exist. Instead running the MC code with the simulated DM structures enabled us to write down relations between the D, α and ϵ parameters (Eqs. (3.25) and (3.26)). From these relations we were able to show why Austin et al. (2005) and DM05 find $\epsilon = 3$ and $\alpha = 1.94$ as good fits to their simulations when restricting themselves to the $D = 0$ case. The parameters don't seem to have any mass or redshift dependence, indicating that the found parameter relations might also be valid for higher redshifts (as long as the structures are relaxed).

3.6 Evaluating the Limiting γs

Now having quantified the unknown parameters in Eq. (3.11) by the MC code we will turn towards a more theoretical investigation of the master equation. In this section we will start by considering the master equation from a purely theoretical point of view. We will consider the convergence values of the master equation Eq. (3.11) (and its derivative Eq. (3.19)), γ_1, γ_3, γ_- and γ_+. Using these we can get an idea of how DM structures described by Eq. (3.11) behave in the inner and outer regions. 'Allowing' the limits as inner and/or outer slopes will then put some theoretical constraints on the parameters and the limits themselves. We will then compare these constraints with the optimized parameters from Table 3.3 calculated with the MC code. This enables us to determine which of the convergence values, i.e., expressions for the DM structure density slopes are most probable as inner and/or outer density slopes.

3.6.1 Theoretical Considerations

First we consider the theoretical considerations, which will be quantified using the MC code results in the next section and in Fig. 3.13. The goal is to get an idea of the restrictions the master equation puts on the limiting γs for them to be inner and/or outer slopes of the DM structure density profiles. As mentioned in the introduction the density profile of DM structures is fairly well describe by Eq. (1.2). This corresponds to having a (more or less) constant slope in the inner region, then a 'transition' phase and then a (more or less) constant outer slope. We will therefore assume that $\rho \sim r^{-\gamma}$ for a constant γ in the inner and outer region of the DM structures. Using this on the master equation gives us a LHS on the form

$$\text{LHS} = -\frac{\kappa}{b}x^{EXP} \qquad \text{with} \qquad EXP = 2 - \frac{2\alpha}{\epsilon} - \gamma\left(1 - \frac{2}{\epsilon}\right) . \tag{3.27}$$

As a reminder the RHS of the master equation looks like

$$\begin{aligned}
\text{RHS} &= \gamma'' - \gamma'\left[\frac{2}{\epsilon}(\gamma - \gamma_3) + \frac{2+\epsilon}{\epsilon}((\gamma - \gamma_-) + (\gamma - \gamma_+))\right] \\
&\quad + \frac{2(2+\epsilon)}{\epsilon}(\gamma - \gamma_3)(\gamma - \gamma_-)(\gamma - \gamma_+)
\end{aligned}$$

The idea is now to let the logarithmic density slope γ approach the limits of the master equation, γ_3, γ_+, and γ_-, and the extra limit appearing when differentiating the master equation, i.e., γ_1. This will hopefully give an overview of allowed inner and outer slopes of the density profile of the DM structure. Allowed limits in the outer and inner region must make the LHS converge.

   We start by inspecting the case where $r = r_0 x \to 0$. In this case the LHS will diverge if $EXP < 0$ and converge (slowly vanish) when $EXP > 0$. Thus when $r \to 0$ the limit is allowed as an inner density slope for the DM structure if $EXP > 0$. Considering the limits one at a time, we have that when γ goes towards:

γ_1 the RHS becomes constant for all parameter values, and

$$EXP_1 \to 4\frac{\alpha - 3\epsilon}{\epsilon(\epsilon - 2)} \tag{3.28}$$

γ_3 the RHS becomes 0 and the EXP reduces to

$$EXP_3 \to 3 - \alpha - \frac{\epsilon}{2} \ . \tag{3.29}$$

This implies that for $\alpha < 3 - \frac{\epsilon}{2}$ the value γ_3 is an allowed slope in the inner region, and the LHS will slowly vanish as $r \to 0$. Whereas $\alpha > 3 - \frac{\epsilon}{2}$ makes the LHS diverge and is therefore not a physically acceptable density slope in the inner region of DM structures.

γ_+ the RHS will become 0. Evaluating the EXP in this case gives that

$$EXP_+ \to 2 - \frac{2 - \alpha}{\epsilon} - \left(-\frac{a}{2b} + \frac{\alpha - \frac{a}{D}}{2 + \epsilon} + \frac{1}{2}\sqrt{\text{DISC}} \right) \left(1 - \frac{2}{\epsilon} \right) \tag{3.30}$$

where DISC is from Eq. (3.11) and is given in App. B.

γ_- the RHS will again become 0, and the EXP is similar to the γ_+ case

$$EXP_- \to 2 - \frac{2 - \alpha}{\epsilon} - \left(-\frac{a}{2b} + \frac{\alpha - \frac{a}{D}}{2 + \epsilon} - \frac{1}{2}\sqrt{\text{DISC}} \right) \left(1 - \frac{2}{\epsilon} \right) \tag{3.31}$$

where DISC is again from Eq. (3.11).

If we now turn to the outer limits, i.e., $r = r_0 x \to \infty$, we can use the same approach. Except from the four possible inner limits, we look at another possible interesting outer limit, the $\gamma \to \gamma_\infty$ limit, where γ_∞ refers to a density slope which approaches infinity, i.e., a sharp cutoff of the structure at a given radius. For the outer limits we then have that for γ approaching:

γ_1 the RHS becomes constant and EXP is still given as in Eq. (3.28).

γ_3 the RHS becomes 0 and EXP is given as in Eq. (3.29). This now implies that the LHS diverges if $\alpha < 3 - \frac{\epsilon}{2}$ and slowly vanishes for $\alpha > 3 - \frac{\epsilon}{2}$ making the limit acceptable.

$\gamma_\pm$ the case is similar to the $r \to 0$ case.

γ_∞ the RHS becomes constant and the EXP will approach

$$EXP_\infty \to -\gamma_\infty \left(1 - \frac{2}{\epsilon} \right) \ . \tag{3.32}$$

We have now put theoretical constraints on the possible density slopes, using the expression for EXP. These constraints can be quantified further by using the optimized parameter values calculated with the MC code, to separate the probable limits from the improbable ones.

3.6.2   Comparing with MC results

From the work by Navarro et al. (1996), Navarro et al. (1997) and Hernquist (1990) mentioned in the introduction we know that the slope of DM density profiles is larger in the outer than in the inner parts. The isothermal slope $\gamma = 2$ is a good estimate of the 'transition' slope between the inner and outer regions. The actual values of the different γs from the MC code are plotted in Fig. 3.13. Histrograms of how these γs are distributed are shown in Fig. 3.14. From these figures we see that within errors it seems that the γ_- is probably suitable as inner limit, whereas the γ_3 has the right size for being an outer limit. Such claims can be quantified further by combining the results from the MC code with the theoretical considerations from the previous subsection. Doing this enables us to conclude the following on the various limits.
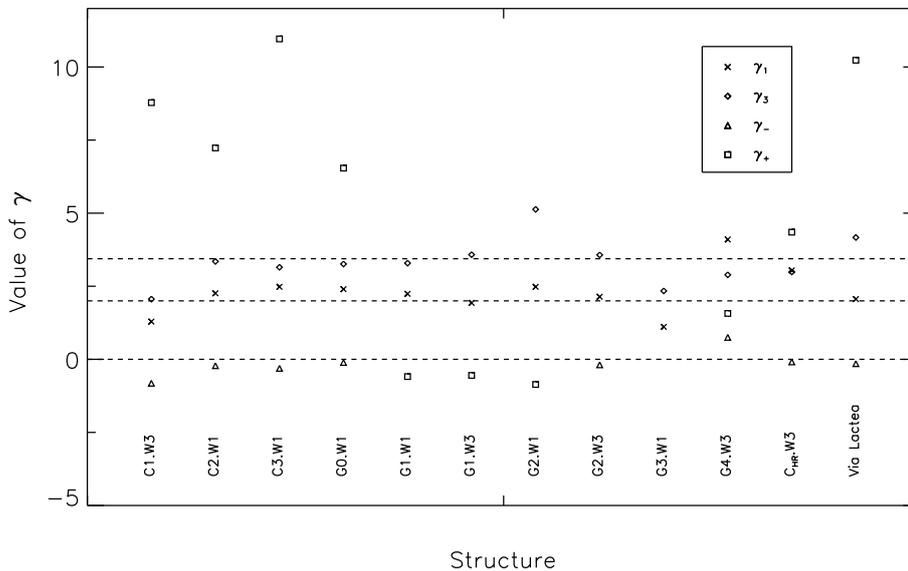
Figure 3.13: The calculated γ_1, γ_3, γ_- and γ_+ values for the structures marked with * in Table 3.3. The dashed lines indicate a probable outer limit value of about 3.44 (as suggested in DM05), the separation between probable inner and outer slopes (i.e., the isothermal slope $\gamma = 2$) and the separation between $\gamma > 0$ (physically valid) and $\gamma < 0$ (implying unphysical solutions). The optimized parameters for the structure G3.W1 implied complex $\gamma_\pm$ so these are not shown. Furthermore the values of $\gamma_+ = 28.2$ for G2.W3 and $\gamma_- = -39.04$, -13.4 and -1728.46 for G1.W1, G1.W3 and G2.W1 respectively are outside the shown range. From this plot it seems probable (within errors) that the $\gamma_\pm$ are inner slopes and the γ_3 is a preferred outer slope. In Fig. 3.14 we plotted the histograms for the γ values to make this point even more clear.

γ_1 Having γ_1 as inner limit would according to the theoretical considerations imply that $EXP_1 > 0$. Using the optimized parameters of the $z = 0$ structures listed
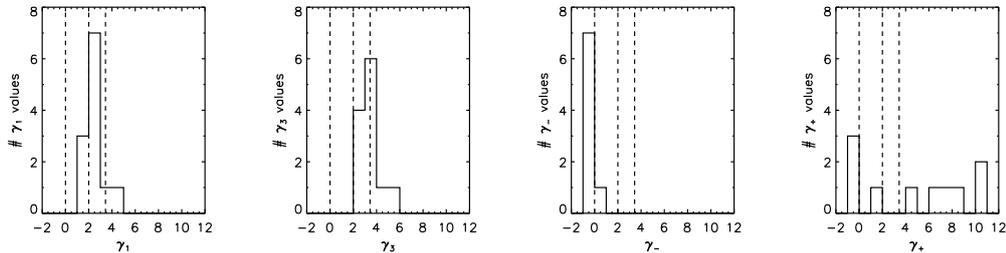
Figure 3.14: Histogram of the optimized γ values from Fig. 3.13. The vertical dashed lines are the same as the horizontal lines in fig Fig. 3.13, i.e., $\gamma = 0$, 2 and 3.44. The histograms clearly illustrate, as explained in the text, that the most probable outer limit is γ_3 and a possible inner limit is γ_- (assuming that it is positive within errors).

in Table 3.3 to calculate EXP_1 show that in $\sim 70\%$ of the cases $EXP_1 < 0$ and γ_1 would according to this be most probable as an outer limit. However, the fact that the value of γ_1 is more likely of the order 2 rather than the preferred outer slope value of ~ 3.44 (see Figs. 3.13 and 3.14) make γ_1 improbable as an outer as well as an inner limit in general.

γ_3 Looking at the values of γ_3 we realize that it's larger than 2 for all the simulated structures and of the order 3.44 for most of them indicating that γ_3 is only valid as an outer limit. This is supported by the fact that calculating $\alpha - 3 - \frac{\epsilon}{2}$ shows that the outer limit criteria of $\alpha > 3 - \frac{\epsilon}{2}$ is fulfilled in $\sim 70\%$ of the cases.

$\gamma_\pm$ How probable the $\gamma_\pm$ are as inner and outer limits is a bit more uncertain, since here we have to include a and b in the calculations, and as mentioned earlier all calculations including these optimized values should be used with care. However, doing similar calculations for the $\gamma_\pm$ and $EXP_\pm$ using the values for the $z = 0$ structures listed in Table 3.3 gives that most often, i.e., in $\sim 90\%$ of the cases EXP_- is larger than 0, indicating that it should be an inner limit. Unfortunately calculating the corresponding values of γ_- itself shows that it's less than 0 for 90% of the structures as well. This would imply a growing density in the inner region, which could be accomplished by a (unphysical) central hole in the DM structure. We might therefore conclude that γ_- is suitable as neither inner nor outer limit of the DM structures. However, as shown in Figs. 3.13 and 3.14 some of the γ_- values might be positive within errors and might therefore be suitable as inner limits.

Calculating EXP_+ shows that it's less than 0 about 55% of the times which does not indicate whether γ_+ should be an inner or an outer limit by itself. Looking at the actual value of γ_+ however, indicates that γ_+ is most likely suitable as an outer limit, since it is larger than 3 for most of the structures.

Some values of γ_+ might also be possible inner limits if we assume them to be positive within errors (e.g. the γ_+ values of G1.W1, G1.W3 and G2.W1). These values correspond to the only structures with $D > 0$ at $z = 0$. This might indicate that the chosen inner limit of the structure is related to whether $D > 0$ or not. Calculating γ_+ for the only structures with $D > 0$ for $z \neq 0$ (G1.W1 and G2.W1 both at $z = 1$) gives values (-0.76 and -1.08) most suitable as inner limits, supporting the possible existence of such a relation.

γ_∞ The evaluation of γ_∞ takes a bit more effort. The conclusion however, is that the estimated parameters from Table 3.3 indicate that γ_∞ is not suitable as an outer limit for DM structures in general. For the full description of the evaluation of the γ_∞ limit please refer to App. D.

Combining the above conclusions and assuming that the small negative $\gamma_\pm$ values are positive within errors, gives γ_- as the most probable inner slope and γ_3 as the most probable outer slope of DM structures. The γ_+ have values suitable as both inner and outer limits. On the contrary γ_1 seems to have a slope of the order 2 in most of the cases. And since the isothermal structure has an infinite mass, γ_1 is suitable as neither inner nor outer slope of DM structures. These conclusions are similar to the conclusion for the isotropic case in DM05, where they conclude that the only 'interesting option' for an inner slope is their isotropic γ_a. And since our $\gamma_\pm$ in a way correspond to the γ_a and γ_b of DM05 the conclusions are similar. However, we should still remind ourselves that we use a and b in the calculations of $\gamma_\pm$, which might change the picture if done with other more trustworthy values of a and b.

3.7 Estimating $\alpha_{\mathbf{crit}}$

Returning to the differentiation of the master equation (i.e., Eq. (3.19)) we are now able to estimate a critical value for the α parameter using the set of parameters optimized by the MC code. As in DM05 one could argue that there must be a critical α, which is defined as where the solutions that make the flow in Eq. (3.19) vanish are equally spaced in the $(\gamma, \gamma', \gamma'', \gamma''')$ space. This criteria can be expressed through the equation

$$\gamma_1 = \frac{1}{3}(\gamma_3 + \gamma_+ + \gamma_-) \tag{3.33}$$

Plugging in the various γs we're then left with

$$-\frac{2}{\epsilon - 2}\alpha_{\text{crit}} + \frac{2\epsilon}{\epsilon - 2} = \frac{1}{3}\alpha_{\text{crit}} + \frac{\epsilon}{6} - \frac{a}{3b} + \frac{2}{3(2 + \epsilon)}\alpha_{\text{crit}} - \frac{2\epsilon}{3D(2 + \epsilon)} \ . \tag{3.34}$$

Isolating α_{crit} we have the expression for the critical α value when combining an all general phase space density with the CJE

$$\alpha_{\text{crit}} = \frac{-\frac{1}{2}\epsilon^3 + \epsilon^2\left(6 + \frac{a}{b} + \frac{2}{D}\right) + \epsilon\left(14 - \frac{4}{b}\right) - \frac{4}{b}}{\epsilon^2 + 8\epsilon + 4} \tag{3.35}$$
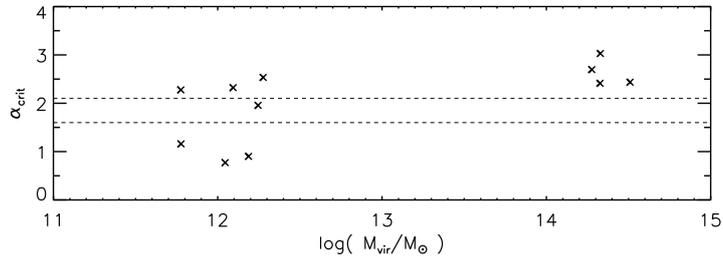
*Figure 3.15: The calculated α_{crit} values for the structures marked with * in Table 3.3 plotted as a function of the virial mass of the structure. The α_{crit} outlier of structure G2.W1 is not shown. A small increase of the α value as a function of the mass is visible. These values don't seem to agree with the optimized α values from the MC code (seen in the center panel of Fig. 3.12) which are of the order 1.6 to 2.1, indicated by the dashed lines. This might be because of using a and b when calculating α_{crit}.*

Combining the optimized parameters with this theoretically predicted expression for α_{crit} of DM structures, we are able to quantify the critical value for each structure in Table 3.3. We have plotted these values in Fig. 3.15 for the $z = 0$ structures as a function of the structures virial mass. Since the values of a and b are used in calculating α_{crit} the results should be taken with caution, because of the discussed relation between a and b. Unlike the parameters calculated via the MC code (shown in Fig. 3.12) there seems to be a slight increase in the predicted critical α value as a function of the mass of the structures. As explained above our results don't prefer 'golden' parameter values which agrees well with the observed slight increase in α_{crit}. According to this no 'golden' value of the critical α value seems to exist. Unfortunately we know that most of the γ_- limits are unphysical which indeed doesn't make the calculated α_{crit} values trustworthy. Thus we are unable to predict any physically valid trend in α_{crit}, but can only present the presumed form of it (Eq. (3.35)) when using a general phase space density in the CJE.

3.8   Flow Diagrams for Insight

Flow diagrams are often used to investigate and get insight into complex equations and to model actual physical systems. In the same way we will now use flow diagrams to evaluate Eq. (3.19) and hopefully gain more insight into the behavior of the density slopes of DM structures described by this equation.

In DM05 they create flow diagrams for the derivative of the isotropic master equation (the isotropic version of Eq. (3.3)) to get even more insight into DM structures in general. What they basically do is to look at how γ'' behaves in the (γ', γ) space by plotting the γ' against the convergences in the equation, i.e., $(\gamma - \gamma_a)(\gamma - \gamma_b)(\gamma - \gamma_1)$ (for the isotropic expressions of γ_a, γ_b and γ_1 please refer to DM05). In Fig. 3.16 we have reproduced the flow diagrams of DM05 for $\alpha = 15/8$, $35/18$ and 2. The

overplotted parabola corresponds to $\gamma' = \frac{2}{3}(\gamma - \gamma_a)(\gamma - \gamma_b)$. Only solutions above the parabola are physically valid since γ' below it would imply a negative reference density, ρ_0, in Eq.(3.3), which we can't allow. In each plot we see that only two of the γ values (where the flow vanishes) are connected. These are in principle physically valid solutions to the equations. However, solutions with $\gamma < 0$ or $\gamma' < 0$ at any point are unrealistic. If $\gamma < 0$ the density will increase with increasing radius and if $\gamma' < 0$ the γ profile must have some sort of a 'bump', i.e., some 'disturbance' in the otherwise smooth density profile. Both of these cases are unrealistic for relaxed DM structures. Thus the only realistic solutions occurs when $\alpha \leq \alpha_{\mathrm{crit}} = 35/18$ where flow patterns without $\gamma < 0$ or $\gamma' < 0$ are only possible.

(a) $\alpha = 15/8$ (b) $\alpha = 35/18$ (c) $\alpha = 2$

WEAK   FLOW STRENGTH   STRONG
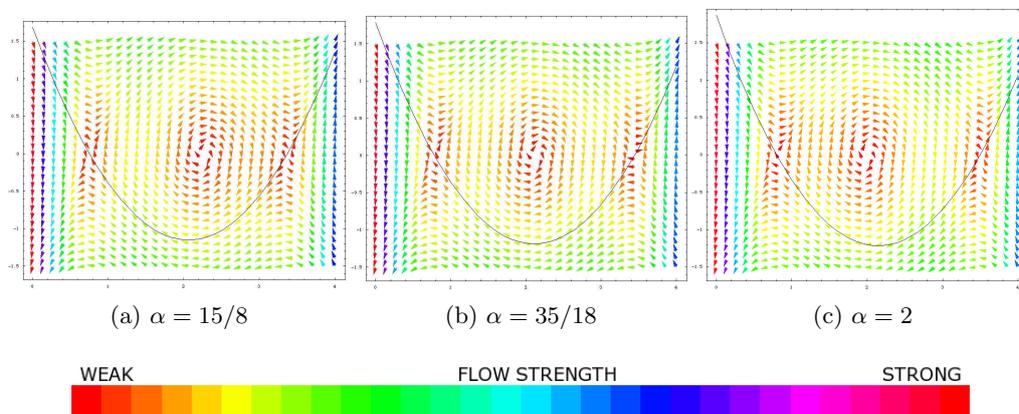
Figure 3.16: Reproduction of the flow diagrams from DM05. The parabola corresponds to $\gamma' = \frac{2}{3}(\gamma - \gamma_a)(\gamma - \gamma_b)$. The x-axis is γ in the range [0,4] and the y-axis is γ' in the range [-1.5,1.5]. Each vector in the diagrams are normalized for ease of reading, but the color scale (grey scale) indicates the strength of the flow (i.e., γ''). The flow vanishes at the γs (sources and sinks in red) and increases outwards. For a discussion of the figures please refer to the text or DM05.

Since DM05 only plot the convergences and the derivatives of the density slope in their flow diagrams, and not the actual equation, the flow diagrams are valid for *all* structures with the convergence values γ_a, γ_b and γ_1. Thus the flow diagrams in DM05 should tell us the same about the anisotropic case as they do about the isotropic case, since the only difference between the anisotropic and isotropic convergence values are 'numerical constants' as DM05 express it. They argue that because of this the topology of the isotropic and anisotropic flow diagrams are similar and hold in principle the same information. One might nevertheless expect that information is lost when looking at the anisotropic case. It is therefore questionable whether the plots in Fig. 3.16 contain at least the same information as do plots of the actual equation. If we plot the actual equation in the isotropic case from DM05 (as is done in Fig. 3.17 for the three different α values) we for instance get the information that for $\gamma \sim 2$ (depending on α) the γ' dependence is eliminated from the equation. This

information can't be seen in the flow diagrams of the convergences only. We also see that when imaging the whole equation we can't connect the solutions γ_a and γ_b because of the barrier near $\gamma = 2$. Thus the possible slope combinations seems to be limited by the critical α value $\alpha_{\mathrm{crit}} = 35/18$. For instance it is possible to create a solution in the flow by connecting γ_1 and γ_b only when $\alpha < \alpha_{crit}$. This behavior is also seen in Fig. 3.16 but is much more clear when plotting the whole equation as in Fig. 3.17. Because of this difference in the gained information between the two ways of evaluating the flow, we decided to use both kinds of plots when investigating the derivative of our master equation.
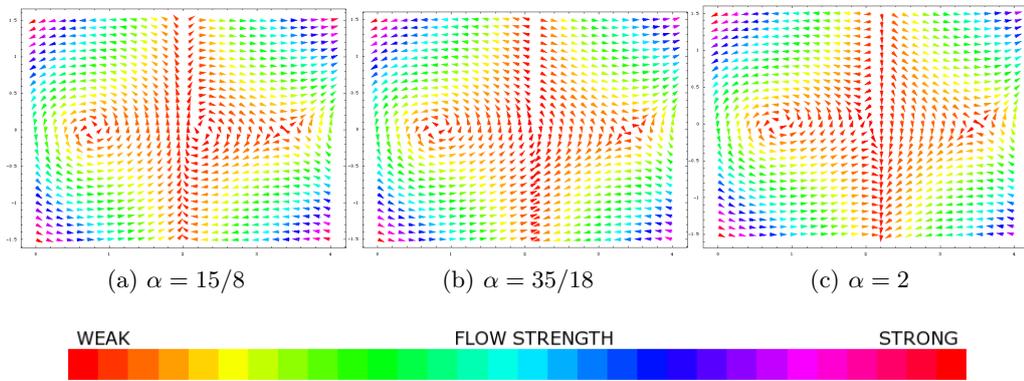
Figure 3.17: The flow diagrams of the actual derivative of the isotropic master equation from DM05 illustrating the extra information gained, compared to only plotting the limits as done in Fig. 3.16. The three sources and sinks in each plot correspond from left to right to DM05's γ_a, γ_1 and γ_b. The axes, normalization and color scale are similar to the ones in Fig. 3.16.

Before we did that we investigated the anisotropic flow diagrams of the actual equation appearing when taking the derivative of the 'master equation' in DM05. Compared to the isotropic case the limiting values γ_a, γ_b and γ_1 (given in Sec. 3.1 and Eq. (3.20)) now depend on more 'numerical constants' than just α, namely ϵ and β_0. The plots of the derivative of Eq. (3.3) (Eq. (27) in DM05) are similar to the isotropic ones except for the ϵ and β_0 dependences. In general as β_0 grows the points in which the flow disappears, i.e., the γs approach each other, and the barrier where the flow in the γ' direction almost disappears moves towards larger vales of γ. The value of ϵ changes the flow gradient and makes the convergence points move further away from one another as it grows. DM05 mention that $\beta_0 = -0.1$ and $\epsilon = 3$ fits their data the best. We see that the flow for small β_0 values produces a flow very similar to the isotropic case if $\epsilon = 3$. Furthermore if $\epsilon < 3$ the 'center convergence' (of the three values γ_a, γ_b and γ_1) is located left of the barrier and α_{crit} decreases with decreasing β_0. On the other hand $\epsilon > 3$ implies increasing α_{crit} with decreasing β_0 and a center convergence on the right of the barrier. So in order to have a connection between a probable inner and outer limit a suitable combination

of a relatively large β_0 (to move the barrier to the right of 2) and a $\epsilon \lesssim 3$ (to have the center convergence on the left side of the barrier) would be preferable in the anisotropic case of DM05. The plots of the actual anisotropic equation from DM05 and the plots of its convergences are shown for different values of α, ϵ and β_0 in App. E.

When investigating our approach (described in Sec. 3.2) we created similar flow diagrams for both the convergences of Eq. (3.19) and the equation itself. Looking at the convergence values, which in our case are γ_1, γ_3, γ_+, and γ_- (given in Eqs. (3.12), (3.13), and (3.20)), in $(\gamma, \gamma', \gamma'')$ space results in flow diagrams corresponding to the ones shown in DM05, except that instead of 2D ours are in 3D. An example of one of these 3D flow diagrams is shown in Fig. 3.18a. In this 3D plot there is virtually no flow dependence in the γ'' direction, so in order to investigate the flow we make a cut in the 3D cube at $\gamma'' = 0$. This is what is shown in Fig. 3.18b. To be able to plot the flow we need the parameter set $(a, b, D, \alpha, \epsilon)$ as input when calculating the γs. In Fig. 3.18 we have used the structure G0.W1 as numerical input. On Fig. 3.18b we see that the flow vanishing points aren't directly connected by the flow and no 'trajectories' with γ and $\gamma' > 0$ in all points are visible, which would be needed for a solution to be physically valid. The flow doesn't seem to create obvious connections between the convergence values, much in line with the theoretical evaluations of the limits in Sec. 3.6. It is also seen that the flow in the γ' direction changes sign on each side of a convergence unless two of these lie close enough to make the flow curl. Plotting the other structures gives similar results, with even more pronounced separation of the limiting values. These plots are shown in App. E. Furthermore the flow strengthens as one moves away from the 'curly' regions of the γs. This indicate that no solutions connect the $\gamma_\pm$ to the γ_1 and γ_3. In the specific case of G0.W1 $\gamma_1 = 2.40$, $\gamma_3 = 3.26$, $\gamma_- = -0.11$ (indicating an inner density hole or and infinitely large structure mass, both unphysical) and $\gamma_+ = 6.54$ (for all γ values see Fig. 3.13). As explained in Sec 3.6 the values of $\gamma_\pm$ should be used with care, because they depend on a and b.

Plotting the actual derivative of the master equation, i.e., Eq. (3.19) instead of just the convergences gives plots like Fig. 3.19a in $(\gamma, \gamma', \gamma'')$ space. We again use G0.W1 as the input when calculating the γs. Here there is a bit more dependence on γ'', but to be able to see the flow patterns more clearly we have again made a cut in the 3D plot at $\gamma'' = 0$. This cut is shown in Fig. 3.19b. The small γ'' dependence, cuts for the other structures, and cuts for G0.W1 with $\gamma'' \neq 0$ are shown in App. E.

Interpreting the information gained by flow diagrams of the actual equation gives more information (which is obvious when comparing Figs. 3.19b and Fig. 3.18b) and not quite the same conclusions compared to interpreting the flow from the convergence values. Therefore we would like to stress the importance of not just looking at the flow of the convergences, but also the flow of the actual equation. First of all we see that there is a possible connection between the two convergences to the left in Fig. 3.19a corresponding to γ_- and γ_1. Thus if we assume that γ_- is positive within errors we here have a possible inner and outer density slope connection. One could imagine that a possible connection to the next convergence could be made in
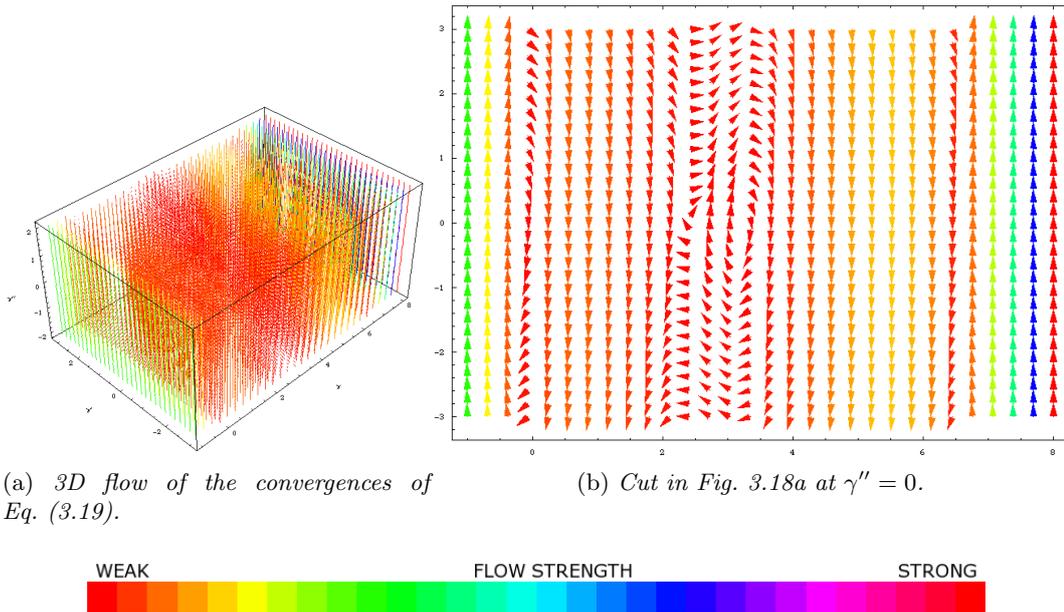
(a) *3D flow of the convergences of Eq. (3.19).*

(b) *Cut in Fig. 3.18a at $\gamma'' = 0$.*

Figure 3.18: *The flow diagram of the limiting γs in our approach. As seen in Fig. 3.18a there is virtually no change in the γ'' direction, so we have made a cut in the 3D picture at $\gamma'' = 0$, shown in Fig. 3.18b, in order to get a handle on the flow patterns. The values used to calculate the actual input to the equation, is from the G0.W1 simulation at $z = 0$ (see Table 3.3). In Fig. 3.18a the x-axis is γ in the range [-1,8], the y-axis is γ' in the range [-3,3] and the z-axis is γ'' in the range [-2,2]. In Fig. 3.18b the x-axis is also γ in the range[-1,8] and the y-axis is γ' in the range [-3,3]. The vectors have been normalized for ease of reading. The color scale (grey scale) in both figures indicates the strength of the flow (i.e., γ'''). Plots similar to 3.18b for the other simulated DM structures are shown in App. E.*

(a) *3D flow of Eq. (3.19) with G0.W1 as input.*

(b) *Cut in Fig. 3.19a at $\gamma'' = 0$.*

WEAK   FLOW STRENGTH   STRONG
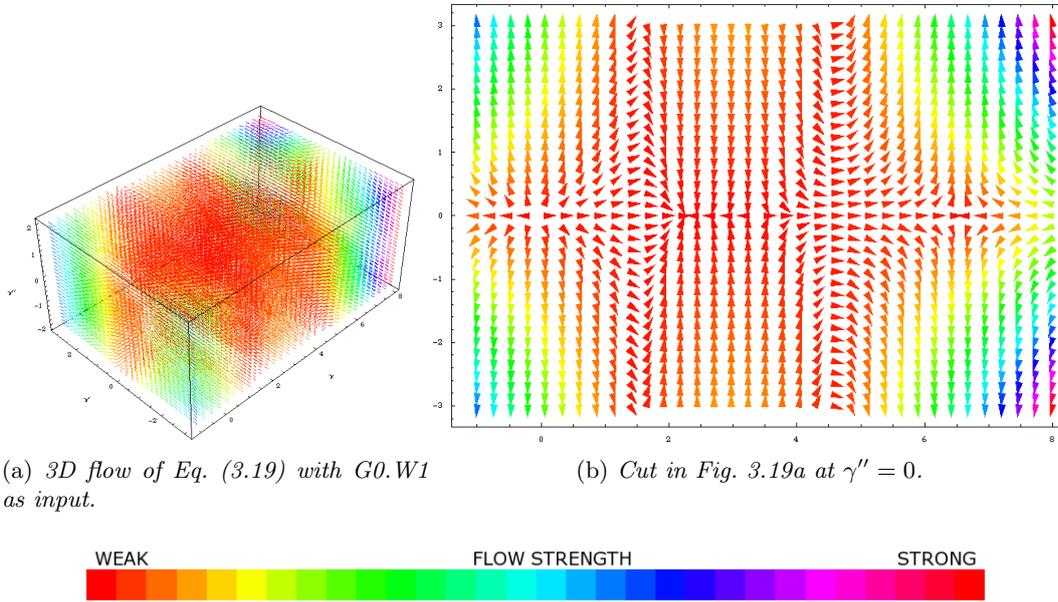
Figure 3.19: The flow diagram appearing when plotting the behavior of Eq. (3.19) in $(\gamma, \gamma', \gamma'')$ space. Similar to Fig. 3.18 we use the G0.W1 simulation at $z = 0$ as input. Fig. 3.19b is a cut in the 3D flow diagram in Fig. 3.19a at $\gamma'' = 0$. The axes, normalization and color scale are similar to the ones used in Fig. 3.18. Plots similar to 3.19b for the other simulated DM structures are shown in App. E.

3D but it seems that such a connection is not possible when looking at cuts for $\gamma'' \neq 0$ (see Fig. E.4 in App. E). The convergence at the right (γ_+) seems isolated from the other convergences. The same picture of one possible connection and isolated limits is also seen when looking at the flow diagrams of the other simulated structures (App. E).

Furthermore the flow seems to stagnate for given γs in the γ' direction. These barriers are similar to the ones seen in the anisotropic flows of DM05. Moving away from the convergence values the flow strength increases also similar to the DM05 case, which is not seen when only plotting the flow of the convergency values.

Thus in general the flow of the actual equation is much more rich on information than the flow from just the convergences.

3.9 Numerical Integration of the Master Equation

As mentioned earlier it would also have been interesting to numerically integrate the master equation from the inner parts of the DM structures and out, to see if this could give any estimates of the transition between the inner and the outer slopes of DM structures. Furthermore, such an approach might also predict possible outer slopes of structures where these couldn't be evaluated with some of the methods used in the previous sections. Integrating from some of the outer limits (e.g. γ_3) and inwards could possibly estimate the sizes of the inner slopes which we weren't able to do, because of the problematic relation between the a and b values. However, as we have argued for and shown there doesn't seem to be any preferred 'golden' values of the unknown parameters in Eq. (3.11). Thus a numerical integration would only be valid for the structure(s) for which the input parameter set $(a, b, D, \alpha, \epsilon)$ was valid. We have therefore not had this as a major priority, but it would definitely be interesting to look further into this in the future as noted in Sec. 5.

3.10 Conclusion

To sum up the conclusions in the 'Jeans investigation' part of the work we have generalized the studies by DM05 (Sec. 3.2). Instead of constraining ourselves by only using a velocity dispersion in the radial direction in the phase space density we use a general phase space density on the form given in Eq. (3.7). Combining this general phase space density with the single most important equation for collisionless matter, the Jeans equation, gives a new form of the CJE (Eq. (3.11)), which we have studied. The unknown parameters in this equation relates the density slope γ, the radius r, the phase space density and the velocity anisotropy β of DM structures to one another. By writing a Monte Carlo code to optimize these parameters we have shown the existence of two strong relations (Eqs. (3.25) and (3.26)) between D (determining the appearance of the velocity dispersion in the general phase space density used), α and ϵ. These relations are able to reproduce the results from DM05, which according to our investigation are not general but just a consequence of their choice of a specific phase space density (the $D = 0$ case). Furthermore these relations

give the preferred values of α and ϵ for other values of D, i.e., for other kinds of phase space densities (Table 3.4).

We have analyzed the analytical convergences of (the derivative of) Eq. (3.11), to get an overview of the allowed/preferred density slopes of DM structures in general. We have shown that γ_1, γ_3 and $\gamma_\pm$ are all theoretically valid as inner and outer slopes as long as certain criteria are fulfilled. However, combining these criteria with the optimized parameters obtained from the MC code indicates that γ_3 is the most probable outer density slope of DM structures. This is in agreement with the conclusions from DM05. The constraints on $\gamma_\pm$ are uncertain because of uncertainty in the optimized a and b values, but the optimized parameters nevertheless indicate that γ_- is most probable as inner limit (within errors). We have also derived the analogues of the α_{crit} from DM05 using our general phase space density. This expression of α_{crit} is shown in Eq. (3.35).

Finally we have investigated the flow of Eq. (3.19) in a way similar (but more general) to the flow investigation in DM05. Instead of just looking at the flow of the convergences we analyze the flow of the actual equation. Before doing it for our case we investigated Eq. (27) of DM05 in a similar way, finding that $\epsilon = 3$ and $\beta_0 = -0.1$ do indeed give a flow similar to the isotropic flow in DM05 and that $\epsilon \lesssim 3$ is most suitable for getting a connection between a probable outer and inner slope. The flow diagrams of our approach (shown in Figs. 3.18 and 3.19) show that we might be able to combine some of the convergence values (γs) in the flow if we assume γ_- to be positive within errors (in the specific case of G0.W1), which is much in line with the analytical study of the convergences of the equation. It also seems that some of the limits are fully isolated from the others since no path in 3D is detectable. However, the flow diagrams use a and b as input when calculating the $\gamma_\pm$ values and might therefore change using more reliable values of a and b.

4 Final Conclusion

The main goal of this work was to investigate and contribute to the understanding and knowledge about dark matter (DM) structures in general. We have focused on two different aspects linked by the most important equation when describing collisionless matter in general and DM in particular, namely the collisionless Jeans equation (CJE). We have investigated the effect of adding rotation to a DM system and described DM structures using a general phase space density inspired by the work of Dehnen & McLaughlin (2005) (DM05).

The results from the rotational investigation are achieved by assuming that the phase space velocity distribution function (DF) of DM structures is distorted and not just shifted when a small bulk rotation is added to a DM system. We have argued for a linear dependence on the added rotation in the new perturbed velocity dispersion. The actual distortion of the DF is shown to exist in high resolution simulations of galaxies, and must therefore be considered a reasonable assumption. The linear dependence is achieved assuming that higher order terms in the rotation can be ignored. We show that the part of the distortion of the DF, P, which depends on the rotation is approximately linear in a simulated galaxy. So as long as the added bulk rotation is assumed small, it is justified to assume P constant, and therefore the new velocity dispersion takes the form in Eq. (2.30). Using this expression combined with the CJE we get a new Jeans equation containing a new subdominant rotational term. By conjecturing that this new rotational term must follow the dominating terms in the CJE we suggest two relations (Eqs. (2.32) and (2.33)) between the rotation and mass and velocity anisotropy of DM structures respectively. These two relations are shown to fit very well with high resolution CDM simulations. This is not just a consequence of comparing a term of the right units with the terms in the Jeans equation, but seems to be of more physical origin. Whether it is connected to the merger history of the simulated structures, or is a consequence of the initial tidal torques is hard to say. We also show that the suggested relations are able to reproduce and agree with recent work on the radial dependence of the angular momentum of DM structures.

Furthermore we show that adding an all general phase space density to the CJE gives an even more general expression for the behavior of DM structures than the one presented in DM05 and Austin et al. (2005). Creating a MC code to extract the unknown parameters in this general CJE from CDM simulations, we show that the work by DM05 is not general, but just a consequence of choosing the parameter D (that makes the phase space density we use more general than the one in DM05) equal to 0. This we quantify in two linear relations (Eqs. (3.25) and (3.26)) between the parameters governing the general phase space density relation with radius. This imply that no 'golden' parameter values exist for DM structures. The parameters seem to depend on neither redshift nor mass, suggesting that Eqs. (3.25) and (3.26) might also hold for DM structures at other redshifts and with masses different from the ones used here.

Thus we have contributed to the unraveling of the 'DM mystery' by showing

how DM structures are in general affected by including a small bulk rotation in the equations governing DM systems and by showing how DM structures can (or cannot) be described when including a general phase space density in the Jeans equation.

5 Future Prospects

In this section we will list several ideas on how to improve and/or extend the work presented in this thesis. Some of the ideas are straight forward to do if one just have the time (and the data), whereas others might take a bit more effort since they might possibly move one into 'unknown DM terrain'.

- The first and most obvious way to extend our work is to extend the set of simulations used to compare our suggested relations to and to optimize the unknown parameters in Eq. (3.11). Especially comparing the suggested rotational relations with more high resolution data would be interesting. Furthermore it would be interesting to see whether more structures at different redshifts could change our conclusions when looking for redshift dependence in the optimized parameters. A better resolution of Fig. 3.11 would definitely strengthen any conclusion.

- Expanding the data set and resolution of 'real' simulated galaxies would definitely also be interesting. We only had the data from one simulated galaxy containing both gas, stars and DM. From this structure we see a linear dependence between the difference in the azimuthal velocity dispersion relative to the rotation as a function of the rotation. It would be interesting to see if this correlation hold for galaxies in general or if it is only true for the K15 galaxy used here. Furthermore, getting a larger data set with higher resolution, i.e., more particles in each structure for these galaxies would enable one to look for the suggested distortion of the DFs as we have done for K15. Is it true for all (simulated) galaxies that the DF containing rotation is indeed distorted? In general it would be very interesting to make plots similar to Figs. 2.1 and 2.2, containing more than just one structure.

- If one had more 'real' galaxies it would also be interesting to test if the actual *shape* of the perturbed velocity distribution function we predict is (or could be) reproduced in simulations. We have shown that a perturbation does indeed exist (at least in K15) but it would be interesting to see if the observed distortion (if general) resembles the form we suggest.

- Before one is able to investigate the different DFs one has to align the different numerical bins. The data we were provided for the K15 had been aligned using potential bins. It would be interesting to see if the DF analysis is affected by the chosen binning. Especially concerning the difference between using radial and potential bins.

- Another interesting way to improve the presented work is to look at the generalized phase space density we use in the evaluation of the Jeans equation. It could be interesting to see if this phase space density evolves in time, and if it does then figure out how.

- An improvement of the MC code would also be a good way to improve our work. The code is not near 'automatic' in the sense that it needs supervision an a lot of 'human interaction' in order to produce the results. If one makes the code more homogeneous and creates a program 'feeding' the data files to it, it would ease the process and enable the investigation of much larger sets of simulations, without to much extra effort. As mentioned in the text the part of the code optimizing relation (3.14) seems to prefer the (unwanted) trivial solution $a = 1$, $b = 0$ and $D = 0$. It would most certainly also be nice to improve the code so that this problem doesn't appear. Such an improvement would give more trustworthy results, when using the a and b parameters in calculations.

- It could also be very interesting to create a set of equations similar to Eq. (40) of DM05 resulting in expressions for $\rho(r)$, $M(r)$, $\sigma_r(r)$ etc. However these equations might not be analytically solvable for a general phase space density. Here a set of trustworthy optimized parameters $(a, b, D, \alpha, \epsilon)$ might give a helping hand. If we by improving the MC code could get such a set of parameters (and maybe relations between them like the ones presented in Eqs. (3.25) and (3.26)) they could be plugged into the equations, an hopefully make them solvable. Then comparing these equation with simulations like in DM05, might provide even more insight into DM structures.

- Last but not least it would as mentioned in the text be interesting to see whether a numerical integration of each of the simulated structures, could estimate the inner slope by assuming the suggested outer slopes in γ_3 or vice versa assuming some inner slope (e.g. γ_-). However for this to give convincing results, we would again need a better optimized set of a and b values.

A   The Spherical Collisionless Boltzmann Equation

The starting point for the derivation of the CBE is that the velocity distribution function, f, for the DM particle ensemble doesn't change in time. And since we are interested in the spherical version of the CBE, using the general form of the CBE Eq. (4-13a) in Binney & Tremaine (1987), we have that

$$0 = \frac{\partial f}{\partial t} + \dot{r}\frac{\partial f}{\partial r} + \dot{\theta}\frac{\partial f}{\partial \theta} + \dot{\phi}\frac{\partial f}{\partial \phi} + \dot{v}_r\frac{\partial f}{\partial v_r} + \dot{v}_\theta\frac{\partial f}{\partial \theta} + \dot{v}_\phi\frac{\partial f}{\partial v_\phi} \ . \tag{A.1}$$

Here a dot ($\cdot$) denotes a variation in time, i.e., we have both particle velocities and accelerations in the above equation. We know that the particle velocities for the different components in the spherical metric is given by $\dot{r} = v_r$, $\dot{\theta} = \frac{v_\theta}{r}$ and $\dot{\phi} = \frac{v_\phi}{r\sin\theta}$. If we let the total velocity be a vector $\overline{V}$ and project it onto the three spherical unit vectors $\hat{e}_r$, $\hat{e}_\theta$ and $\hat{e}_\phi$, such that

$$\overline{V} = v_r\hat{e}_r + v_\theta\hat{e}_\theta + v_\phi\hat{e}_\phi \tag{A.2}$$

we can differentiate to obtain

$$\frac{d\overline{V}}{dt} = \dot{v}_r\hat{e}_r + v_r\dot{\hat{e}}_r + \dot{v}_\theta\hat{e}_\theta + v_\theta\dot{\hat{e}}_\theta + \dot{v}_\phi\hat{e}_\phi + v_\phi\dot{\hat{e}}_\phi \ . \tag{A.3}$$

Using that the rate of change of the unit vectors in spherical coordinates is given by (Binney & Tremaine (1987) Eq. (1B-29))

$$\dot{\hat{e}}_r = \dot{\theta}\hat{e}_\theta + \dot{\phi}\sin\theta\hat{e}_\phi \tag{A.4}$$

$$\dot{\hat{e}}_\theta = -\dot{\theta}\hat{e}_r + \dot{\phi}\cos\theta\hat{e}_\phi \tag{A.5}$$

$$\dot{\hat{e}}_\phi = -\dot{\phi}\sin\theta\hat{e}_r - \dot{\phi}\cos\theta\hat{e}_\theta \tag{A.6}$$

we can write Eq. (A.3) as

$$\begin{aligned}\frac{d\overline{V}}{dt} = \ & \hat{e}_r(\dot{v}_r - v_\theta\dot{\theta} - v_\phi\dot{\phi}\sin\theta) + \\ & \hat{e}_\theta(v_r\dot{\theta} + \dot{v}_\theta - v_\phi\dot{\phi}\cos\theta) + \\ & \hat{e}_\phi(v_r\dot{\phi}\sin\theta + v_\theta\dot{\phi}\cos\theta + \dot{v}_\theta) \ .\end{aligned} \tag{A.7}$$

Combining the spherical poisson equation

$$\frac{d^2\overline{X}}{dt^2} = -\nabla\Phi(r,\theta,\phi) = -\left(\frac{\partial\Phi}{\partial r}\hat{e}_r + \frac{1}{r}\frac{\partial\Phi}{\partial\theta}\hat{e}_\theta + \frac{1}{r\sin\theta}\frac{\partial\Phi}{\partial\phi}\hat{e}_\phi\right) \tag{A.8}$$

where $\overline{X}$ is just $r\hat{e}_r$, with the expression for the total particle acceleration in Eq. (A.7) implies that

$$-\frac{\partial\Phi}{\partial r} = \dot{v}_r - v_\theta\dot{\theta} - v_\phi\sin\theta\dot{\phi} \tag{A.9}$$

$$-\frac{1}{r}\frac{\partial\Phi}{\partial\theta} = 2\frac{v_r v_\theta}{r} + \dot{v}_\theta - \dot{r}\dot{\theta} - v_\phi\cos\theta\dot{\phi} \tag{A.10}$$

$$\frac{1}{r\sin\theta}\frac{\partial\Phi}{\partial\phi} = 2\frac{v_r v_\phi}{r} + \dot{v}_\phi - (\dot{r}\sin\theta + r\cos\theta\dot{\theta})\dot{\phi} + 2v_\theta\dot{\phi}\cos\theta \ . \tag{A.11}$$

This can relatively simple be rewritten into expressions for the behaviour of the particle acceleration components such that

$$\dot{v}_r \;=\; \frac{v_\theta^2 + v_\phi^2}{r} + \frac{\partial \Phi}{\partial r} \tag{A.12}$$

$$\dot{v}_\theta \;=\; \frac{1}{r}\left(-v_r v_\theta + v_\phi^2 \frac{\cos\theta}{\sin\theta} + \frac{\partial \Phi}{\partial \phi}\right) \tag{A.13}$$

$$\dot{v}_\phi \;=\; \frac{1}{r}\left(-v_r v_\phi + v_\theta v_\phi \frac{\cos\theta}{\sin\theta} + \frac{1}{\sin\theta}\frac{\partial \Phi}{\partial \phi}\right) \; . \tag{A.14}$$

Finally plugging these expressions into Eq. (A.1) together with the expressions for the particle velocities $\dot{r}$, $\dot{\theta}$ and $\dot{\phi}$ gives the spherical CBE:

$$
\begin{aligned}
0 \;=\; & \frac{\partial f}{\partial t} + v_r \frac{\partial f}{\partial r} + \frac{v_\theta}{r}\frac{\partial f}{\partial \theta} + \frac{v_\phi}{r\sin\theta}\frac{\partial f}{\partial \phi} + \left(\frac{v_\theta^2 + v_\phi^2}{r} - \frac{\partial \Phi}{\partial r}\right)\frac{\partial f}{\partial v_r} \\
& + \frac{1}{r}\left(v_\phi^2 \cot\theta - v_r v_\theta - \frac{\partial \Phi}{\partial \theta}\right)\frac{\partial f}{\partial v_\theta} \\
& - \frac{1}{r}\left(v_\phi(v_r + v_\theta \cot\theta) + \frac{1}{\sin\theta}\frac{\partial \Phi}{\partial \phi}\right)\frac{\partial f}{\partial v_\phi} \; .
\end{aligned}
\tag{A.15}
$$

B Deriving the Master Equation

The starting point in deriving the 'master equation' is Eq. (3.10), which as a reminder looks like

$$-\kappa = \frac{1}{yx^3}\frac{d}{d\ln x}\left[\frac{x}{y}\frac{d}{d\ln x}\left(y^f x^g \tilde{\beta}\right)\right] + \frac{2}{Dyx^3}\frac{d}{d\ln x}\left[y^{f-1}x^{g+1}(1-\tilde{\beta})\right] \qquad \text{(B.1)}$$

where $x = \frac{r}{r_0}$, $y = \frac{\rho}{\rho_0}$, $f = \frac{2+\epsilon}{\epsilon}$ (not to be confused with the DF from Sec. 2), $g = \frac{2\alpha}{\epsilon}$, $\kappa = \frac{4\pi G\rho_0 r_0^2}{\sigma_{D,0}^2}$ and $\tilde{\beta} = (1+D\beta)^{-1}$. Splitting this equation into three parts, the part in the square brackets in the first term on the RHS and the first and second term on the RHS themselves, we get the following:

$$
\begin{aligned}
(1) \;\; &= \;\; \frac{x}{y}\frac{d}{d\ln x}\left(y^f x^g \tilde{\beta}\right) \\
&= \;\; y^{f-1}x^{g+1}\left((g-\gamma f)\tilde{\beta} + \tilde{\beta}'\right) \\
(2) \;\; &= \;\; \frac{1}{yx^3}\frac{d}{d\ln x}(1) \\
&= \;\; \frac{1}{yx^3}\Big[(g+1-\gamma(f-1))y^{f-1}x^{g+1}((g-\gamma f)\tilde{\beta}+\tilde{\beta}') \\
&\qquad + y^{f-1}x^{g+1}(-\gamma' f\tilde{\beta}+(g-\gamma f)\tilde{\beta}'+\tilde{\beta}'')\Big] \\
&= \;\; y^{f-2}x^{g-2}\Big[K_1((g-\gamma f)\tilde{\beta}+\tilde{\beta}')+(-\gamma' f\tilde{\beta}+(g-\gamma f)\tilde{\beta}'+\tilde{\beta}'')\Big] \\
(3) \;\; &= \;\; \frac{2}{Dyx^3}\frac{d}{d\ln x}\left[y^{f-1}x^{g+1}(1-\tilde{\beta})\right] \\
&= \;\; \frac{2}{Dyx^3}\left[-y^{f-1}x^{g+1}\tilde{\beta}'+(1-\tilde{\beta})K_1\,y^{f-1}x^{g+1}\right]
\end{aligned}
$$

Here we have used that $-\gamma = \frac{d\ln y}{d\ln x}$, $\gamma' = \frac{d\gamma}{d\ln x}$, $\gamma'' = \frac{d\gamma'}{d\ln x}$, $\tilde{\beta}' = \frac{d\tilde{\beta}}{d\ln x}$, $\tilde{\beta}'' = \frac{d\tilde{\beta}'}{d\ln x}$ and $\frac{dz}{d\ln x} = z\frac{d\ln z}{d\ln x}$ and introduced the constant $K_1 = (g+1-\gamma(f-1))$ for simplicity. Combining (2) and (3) from above then gives

$$
\begin{aligned}
-\kappa\, y^{2-f}x^{2-g} \;=\;\; &\tilde{\beta}'' + \tilde{\beta}'\left[K_1 + g - \gamma f - \frac{2}{D}\right] \\
&+ \tilde{\beta}\left[K_1(g-\gamma f)-\gamma' f - \frac{2}{D}K_1\right] + \frac{2}{D}K_1\,. \qquad \text{(B.2)}
\end{aligned}
$$

Realizing that K_1 can be expressed through the $\gamma_3 = \alpha + \frac{\epsilon}{2}$ similar to the γ_b used in Dehnen & McLaughlin (2005) as $K_1 = -(f-1)(\gamma-\gamma_3)$ we get from Eq. (B.2) that

$$
\begin{aligned}
-\kappa\, y^{2-\frac{2+\epsilon}{\epsilon}}x^{2-\frac{2\alpha}{\epsilon}} \;=\;\; &\tilde{\beta}'' + \tilde{\beta}'\left[-\frac{2}{\epsilon}(\gamma-\gamma_3)-\frac{2+\epsilon}{\epsilon}\gamma+2\left(\frac{\alpha}{\epsilon}-\frac{1}{D}\right)\right] \\
&+ \tilde{\beta}\left[-\frac{2+\epsilon}{\epsilon}\gamma'+(\gamma-\gamma_3)\left(\frac{2(2+\epsilon)}{\epsilon^2}\gamma-\frac{4}{\epsilon}\left(\frac{\alpha}{\epsilon}-\frac{1}{D}\right)\right)\right] \\
&- \frac{4}{D\epsilon}(\gamma-\gamma_3)\,. \qquad \text{(B.3)}
\end{aligned}
$$

Here we have plugged in f and g again and reduced.

    Now we assume that there is a linear relationship between the new modified velocity anisotropy $\tilde{\beta}$ and the density slope γ, i.e.,

$$\tilde{\beta} = \frac{1}{1 + D\beta} = a + b\gamma \; , \; \text{for } D \neq 0 \tag{B.4}$$

where a and b are some unknown constants. This assumption corresponds to the assumption that $\beta = \beta_0 + b_{\mathrm{DM}}\gamma$ in Dehnen & McLaughlin (2005). Substituting Eq. (B.4) into Eq. (B.3) we are left with

$$
\begin{aligned}
-\kappa\, y^{2-\frac{2+\epsilon}{\epsilon}} x^{2-\frac{2\alpha}{\epsilon}} \;=\;& b\gamma'' + b\gamma'\left[-\frac{2}{\epsilon}(\gamma - \gamma_3) - \frac{2+\epsilon}{\epsilon}\gamma + 2\left(\frac{\alpha}{\epsilon} - \frac{1}{D}\right)\right] \\
& + (a + b\gamma)\left[-\frac{2+\epsilon}{\epsilon}\gamma' + (\gamma - \gamma_3)\left(\frac{2(2+\epsilon)}{\epsilon^2}\gamma - \frac{4}{\epsilon}\left(\frac{\alpha}{\epsilon} - \frac{1}{D}\right)\right)\right] \\
& - \frac{4}{D\epsilon}(\gamma - \gamma_3)
\end{aligned}
\tag{B.5}
$$

Using that b is in general not equal to zero, since then the linear relation mentioned above would be nonexistent this implies that

$$
\begin{aligned}
-\frac{\kappa}{b} y^{2-\frac{2+\epsilon}{\epsilon}} x^{2-\frac{2\alpha}{\epsilon}} \;=\;& \gamma'' + \gamma'\left[-\frac{2}{\epsilon}(\gamma - \gamma_3) - \left(\frac{2+\epsilon}{\epsilon} + \frac{2+\epsilon}{\epsilon}\right)\gamma + 2\left(\frac{\alpha}{\epsilon} - \frac{1}{D}\right) - \frac{a}{b}\frac{2+\epsilon}{\epsilon}\right] \\
& + \gamma\left[(\gamma - \gamma_3)\left(\frac{2(2+\epsilon)}{\epsilon^2}\gamma - \frac{4}{\epsilon}\left(\frac{\alpha}{\epsilon} - \frac{1}{D}\right) + \frac{a}{b}\frac{2(2+\epsilon)}{\epsilon^2}\right)\right] \\
& + (\gamma - \gamma_3)\left[\frac{4a}{\epsilon b}\left(\frac{\alpha}{\epsilon} - \frac{1}{D}\right) - \frac{4}{D\epsilon b}\right] \tag{B.6} \\
\;=\;& \gamma'' - \gamma'\left[\frac{2}{\epsilon}(\gamma - \gamma_3) + 2\frac{2+\epsilon}{\epsilon}\gamma - 2\left(\frac{\alpha}{\epsilon} - \frac{1}{D}\right) + \frac{a}{b}\frac{2+\epsilon}{\epsilon}\right] \\
& + (\gamma - \gamma_3)\left[\frac{2(2+\epsilon)}{\epsilon^2}\gamma^2 + \left(\frac{a}{b}\frac{2(2+\epsilon)}{\epsilon^2} - \frac{4}{\epsilon}\left(\frac{\alpha}{\epsilon} - \frac{1}{D}\right)\right)\gamma\right. \\
& \left. + \frac{4}{\epsilon b}\left(a\left(\frac{\alpha}{\epsilon} - \frac{1}{D}\right) - \frac{1}{D}\right)\right] \; . \tag{B.7}
\end{aligned}
$$

We see that the last square bracket is a second order polynomial in gamma which we can put equal to 0 and solve for its roots. Solving the polynomial gives

$$
\begin{aligned}
\gamma_{\pm} \;=\;& \frac{-m \pm \sqrt{m^2 - 4\,l\,n}}{2\,l} \quad \text{with} \\
l \;=\;& 1 \\
m \;=\;& \frac{a}{b} - \frac{2\epsilon}{2+\epsilon}\left(\frac{\alpha}{\epsilon} - \frac{1}{D}\right) \\
n \;=\;& \frac{2\epsilon}{(2+\epsilon)b}\left(a\left(\frac{\alpha}{\epsilon} - \frac{1}{D}\right) - \frac{1}{D}\right)
\end{aligned}
$$

which implies that

$$
\gamma_\pm = -\frac{a}{2b} + \frac{\alpha - \frac{\epsilon}{D}}{2 + \epsilon} \pm \frac{1}{2}\sqrt{\text{DISC}} \qquad \text{with} \tag{B.8}
$$

$$
\text{DISC} = \left(\frac{a}{b}\right)^2 + \frac{4\epsilon^2}{(2+\epsilon)^2}\left(\frac{\alpha}{\epsilon} - \frac{1}{D}\right)^2 - \frac{4\epsilon}{(2+\epsilon)b}\left(3a\left(\frac{\alpha}{\epsilon} - \frac{1}{D}\right) + \frac{2}{D}\right)
$$

Noticing that

$$
(\gamma - \gamma_-) + (\gamma - \gamma_-) = 2\gamma + \frac{a}{b} - \frac{2\left(\alpha - \frac{\epsilon}{D}\right)}{2 + \epsilon} \tag{B.9}
$$

we can substitute this and the roots for the 2nd order polynomial into Eq. (B.7) to get the 'master equation' used in the text. The 'master equation' has the form

$$
-\frac{\kappa}{b}y^{1-2/\epsilon}x^{2-2\alpha/\epsilon} = \gamma'' - \gamma'\left[\frac{2}{\epsilon}(\gamma - \gamma_3) + \frac{2+\epsilon}{\epsilon}((\gamma - \gamma_-) + (\gamma - \gamma+))\right]
$$

$$
+\frac{2(2+\epsilon)}{\epsilon^2}(\gamma - \gamma_3)(\gamma - \gamma_-)(\gamma - \gamma_++) \tag{B.10}
$$

where $\gamma_3 = \alpha + \frac{\epsilon}{2}$ and $\gamma_\pm$ is defined in Eq. (B.8).

C The MC code

In this appendix we will describe the content of the Monte Carlo (MC) code we have written to optimize the unknown parameters in the master equation Eq. (3.11). This we will do by giving a short description of all the written programs and subroutines which the overall MC code consists of. The actual code(s) can by found at
`www.dark-cosmology.dk/∼kschmidt/thesisMCcode.html`

C.1 chi2.f

This is a short subroutine calculating the χ^2 value between two quantities using Eq. (3.21).

C.2 chi2gambet.f

This subroutine calculates the χ^2 value of the relation (3.14). It combines the data from a given simulation with the actual relation, and then compares the LHS and RHS with each other using the subroutine `chi2.f`. It is also in this subroutine in which the error of the relation is defined.

C.3 chi2rhopow.f

Subroutine similar to `chi2gambet.f` except that this routine calculates the χ^2 value of relation (3.8), and calls `meanchi2.f` instead of `chi2.f` when doing that. The error of relation (3.8) is defined here.

C.4 datetime.f

A simple subroutine creating a string used for naming the output files when running the code. It takes the time (`hhmm`), day (`dd`), month (`MM`) and year (`yyyy`), turns them into character strings and combine them to a string on the form `yyyyMMddhhmm`. This string is unique for each run and combined with an indication of which relation and simulation was used, it provides a suitable name for the output of the MC code, which is easy to find and classify.

C.5 instep.f

This Subroutine ask for the initial step size, i.e., t from Eq. (3.22). This value is then lowered when the χ^2 values are improved to make the code converge.

C.6 maingambet.f

This is the main program for optimizing the relation (3.14). It is here the overall MC loop is. First it calls `range.f`, `startpoint.f`, `readdata.f` and `instep.f` to set up the initial conditions for the run. Then it calculates the χ^2 of the starting point using `chi2gambet.f`. This point is then saved to the output file by calling

`savegam.f`. Now the code enters the overall MC loop. First it creates a new point by jumping from the old one (using `ran1.f` from Press et al. (1992)) as explained in the text. Then it calculates the χ^2 values of these to points using `chi2gambet.f` again. These to χ^2 values are then compared to each other. If the new χ^2 is the smallest it is saved in the output file together with the parameters giving it, using `savegam.f` and the size of the jumps (t) is lowered. If χ^2 is larger than the old one the code tests if it fulfills the 'metropolis' choice in Eq. (3.24). If the 'metropolis' choice is fulfilled the point is kept and the loop starts over (without saving the point in the output file). If the new point fulfill neither of the above it is ignored and the code takes a new jump from the initial point. This continues until a certain jump size or the total number of loops allowed is reached.

C.7 mainrhopow.f

This code is the main program for optimizing the relation (3.8). It does the same as `maingambet.f` except that it optimizes the relation (3.8) instead of (3.14), and uses `saverho.f` and `chi2rhopow.f` instead of the corresponding ones for the γ-$\tilde{\beta}$ relation.

C.8 maxval.f

This subroutine determines the maximum value in an arbitrary array.

C.9 meanchi2.f

When optimizing the relation (3.8) we had to estimate the normalization as discussed in the text. This is what this code does. It takes the input data and creates two new data sets by changing the normalization for the input data. Estimating the χ^2 value for each of these data sets, provides the code with three points in the ($\chi^2, norm$) space. These points are then fitted to a parabola using `parfit.f` and the minimum of this parabola is estimated using `minpar.f`. Thus the minimum value of the parabola returns the smallest χ^2 and the corresponding normalization. It is this χ^2 which the `meanchi2.f` subroutine returns.

C.10 minpar.f

A small subroutine giving the turnaround (minimum/maximum depending on constants) of a parabola

C.11 minval.f

The same as `maxval.f` except that here it is the minimum value in the array which is determined.

C.12 parfit.f

This subroutine takes three points in a given space, fits the best parabola to them, and returns the coefficients for the second order polynomial that describes this parabola.

C.13 range.f

The `range.f` subroutine contains the initial range of the parameters, as the name indicates.

C.14 readdata.f

Before we can compare the relations with each other and optimize the parameters we need some data input. The `readdata.f` subroutine reads the data from the simulation data files and stores it in the array `d` so that it can easily be used in the overall MC loop.

C.15 savegam.f

This subroutine is called every time a given set of parameters improve the χ^2 value when optimizing the relation (3.14). It saves the relevant results to the output file.

C.16 saverho.f

In the same way as `savegam.f` this code saves the relevant data to the output file for the relation (3.8).

C.17 startpoint.f

As indicated by the name this subroutine generates the starting point for the MC code. It calls the `range.f` subroutine and then creates a random point in the allowed parameter space using the `ran1.f` random generator from Press et al. (1992).

D   Evaluating The Density Slope γ_∞

In this appendix we will give the full evaluation of the possible outer limit γ_∞, which as mentioned in the text results in the conclusion that it is not suitable as an outer density slope for the density profiles of DM structures in general. The γ_∞ limit can be thought of as a sharp cutoff of the structure at a given radius, where the density slope approaches infinity, i.e., a vertical cut in the density profile.
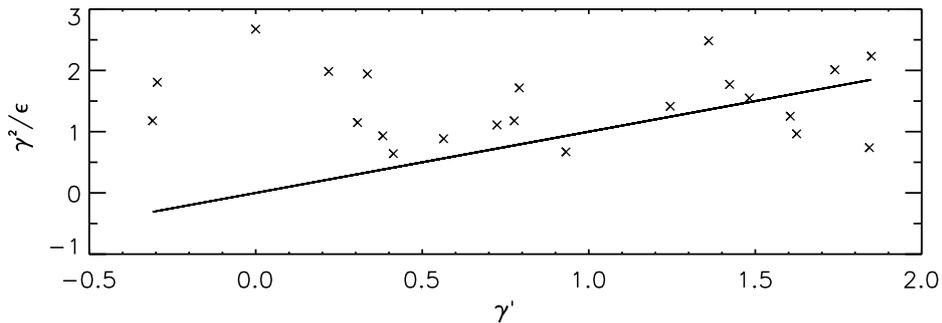
Figure D.1: The relation suggested by equations (full line), which needs to be valid in order for γ_∞ to be a valid outer slope, plotted for the structure G1.W3. Each point corresponds to a bin of data for the structure, in which γ was calculated and compared with $C = \frac{1}{\epsilon}$ using the optimized ϵ from the MC code. Similar plots appear using the $C = \frac{2+\epsilon}{\epsilon}$. It is obvious that the relation (full line) is not followed by the data from the simulated structure. The conclusion is the same when plotting the relations for the other DM structures.

Evaluating the exponent on the LHS of the master equation (Eq. (3.11)) after using that $\rho \sim r^{-\gamma}$ from the introduction assuming γ constant gives

$$EXP_\infty \rightarrow -\gamma_\infty \left(1 - \frac{2}{\epsilon}\right) . \tag{D.1}$$

Thus if γ_∞ would be an outer limit, i.e., $EXP < 0$ then ϵ should be larger than 2. Furthermore the RHS for γ_∞ would in principle converge to a (infinite) constant. One could now be tempted to conclude that γ_∞ is a possible outer limit since the ϵ values in Table 3.3 are larger than 2 for more than 80% of the structures at $z = 0$. This is however not the case. That $\gamma \rightarrow \gamma_\infty$ implies that γ will dominate the values γ_3 and $\gamma_\pm$ on the RHS of the master equation, Eq. (3.11). Thus in the γ_∞ limit the RHS reduces to the second order nonlinear differential equation (assuming that the limit is valid and the LHS therefore slowly vanishes)

$$0 = \gamma'' - K_1 \gamma' \gamma + K_2 \gamma^3 , \tag{D.2}$$

with $K_1 = 2\frac{3+\epsilon}{\epsilon}$ and $K_2 = 2\frac{2+\epsilon}{\epsilon^2}$. This equation can't be solved analytically, but the

equation itself naturally suggests that

$$\gamma' = C\gamma^2 \, , \tag{D.3}$$

which enables one to solve the differential equation assuming that

$$2C^2 - CK_1 + K_2 = 0 \qquad \text{or} \qquad \gamma^3 = 0 \, . \tag{D.4}$$

Since γ is definitely not 0 in the outer parts of the structure we are left with the constraint (solving the second order polynomial in C) that

$$C = \frac{2 + \epsilon}{\epsilon} \qquad \text{or} \qquad C = \frac{1}{\epsilon} \tag{D.5}$$

in order for the differential equation to be solvable. Thus if γ_∞ should be an outer slope of the DM density profile we would need $\frac{\gamma'}{\gamma^2}$ to be either of the order $\frac{2+\epsilon}{\epsilon}$ or of the order $\frac{1}{\epsilon}$. This is rather easy to test using the estimated values of ϵ from Table 3.3. Plotting $\frac{\gamma^2}{\epsilon}$ and $\frac{\gamma^2(2+\epsilon)}{\epsilon}$ against γ' for the simulated structures clearly shows that there is no traceable relation. An example of the plots created is shown for the $\frac{1}{\epsilon}$ case in Fig. D.1. Similar plots appear when using $\frac{2+\epsilon}{\epsilon}$.

From this we can conclude that γ_∞ is not a probable outer limit for the density profiles of the DM structures used in Sec. 3.3. Even though the optimized ϵ values calculated with our MC code listed in Table 3.3 seem to fulfill the restriction that they should be larger than 2, they are clearly not able to solve the differential equation in Eq. (D.2), and hence γ_∞ can't be an outer limit.

E Flowdiagrams

In this appendix we show some of the flow diagrams used in the study of the flow of Eq. (27) from Dehnen & McLaughlin (2005) and our Eq. (3.19). The color scale (grey scale) in all the flow diagrams in this section refers to the flow strength as shown in Fig. E.1. When we plot Eq. (3.19) it is the strength of γ''' the colors show, whereas in the plots for DM05 Eq. (27) the colors refer to the flow strength of γ''.
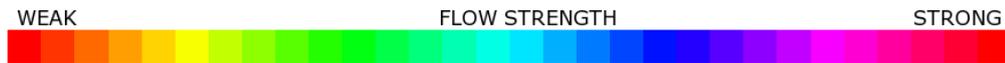
Figure E.1: The color legend for the flow diagrams in this section.

E.1 Flow of the Derivative of the Master Equation

Fig. E.2 shows the cuts in the 3D flows when evaluating Eq. (3.19) for the 12 simulated structures in Table 3.3. Fig. E.3 shows the cuts for $\gamma'' = 0$ when plotting the flow of the convergences only. It is obvious when looking at these figures that the flow diagrams from plotting the actual equation contains more, or at least different information as compared to the flows from the convergences. In Fig. E.4 we have shown some cuts in the 3D flow for various values of γ'' for the structure G0.W1. This illustrates the insignificant γ'' dependence claimed in Sec. 3.8.

E.2 Flow of Eq. (27) in Dehnen & McLaughlin (2005)

Fig. E.5 shows the flow diagrams of Eq. (27) in DM05 for different values of ϵ and β_0. The values of α are calculated using (which corresponds to Eq. (3.5))

$$\alpha_{\text{crit}} = \eta + 2 - \frac{4\eta}{4 - \eta - 2\beta_0} \tag{E.1}$$

with

$$\eta = 2\frac{(\epsilon - 2)(2 - \beta_0)}{6 + \epsilon} \tag{E.2}$$

This is the form of α_{crit} for the anisotropic case with a phase space density on the form $\frac{\rho}{\sigma_r^\epsilon}$ given in DM05 Eq. (36c). The η quantity governs the speed of the transition between the inner and the outer density slopes, and β_0 corresponds to the velcoity anisotropy in the center of the structure. Fig. E.6 shows the flow diagrams when only considering the convergences of Eq. (27) in DM05.

(a) *Via Lactea, 2.06, 4.17, -0.15, 10.23*

(b) *G0W1, 2.40, 3.26, -0.11, 6.54*

(c) *G1W1, 2.24, 3.29, -39.04, -0.59*

(d) *G1W3, 1.93, 3.58, -13.4, -0.55*

(e) *G2W1, 2.48, 3.13, -1728.46, -0.86*

(f) *G2W3, 2.14, 3.57, -0.19, 28.2*

(g) *G4W3, 4.10, 2.89, 0.75, 1.57*

(h) *C1W3, 1.29, 2.06, -0.82, 8.78*

(i) *C2W1, 2.26, 3.35, -0.22, 7.23*

(j) *C3W1, 2.48, 3.15, -0.31, 10.96*

(k) *$C_{HR}.W3$, 3.04, 2.99, -0.09, 4.35*
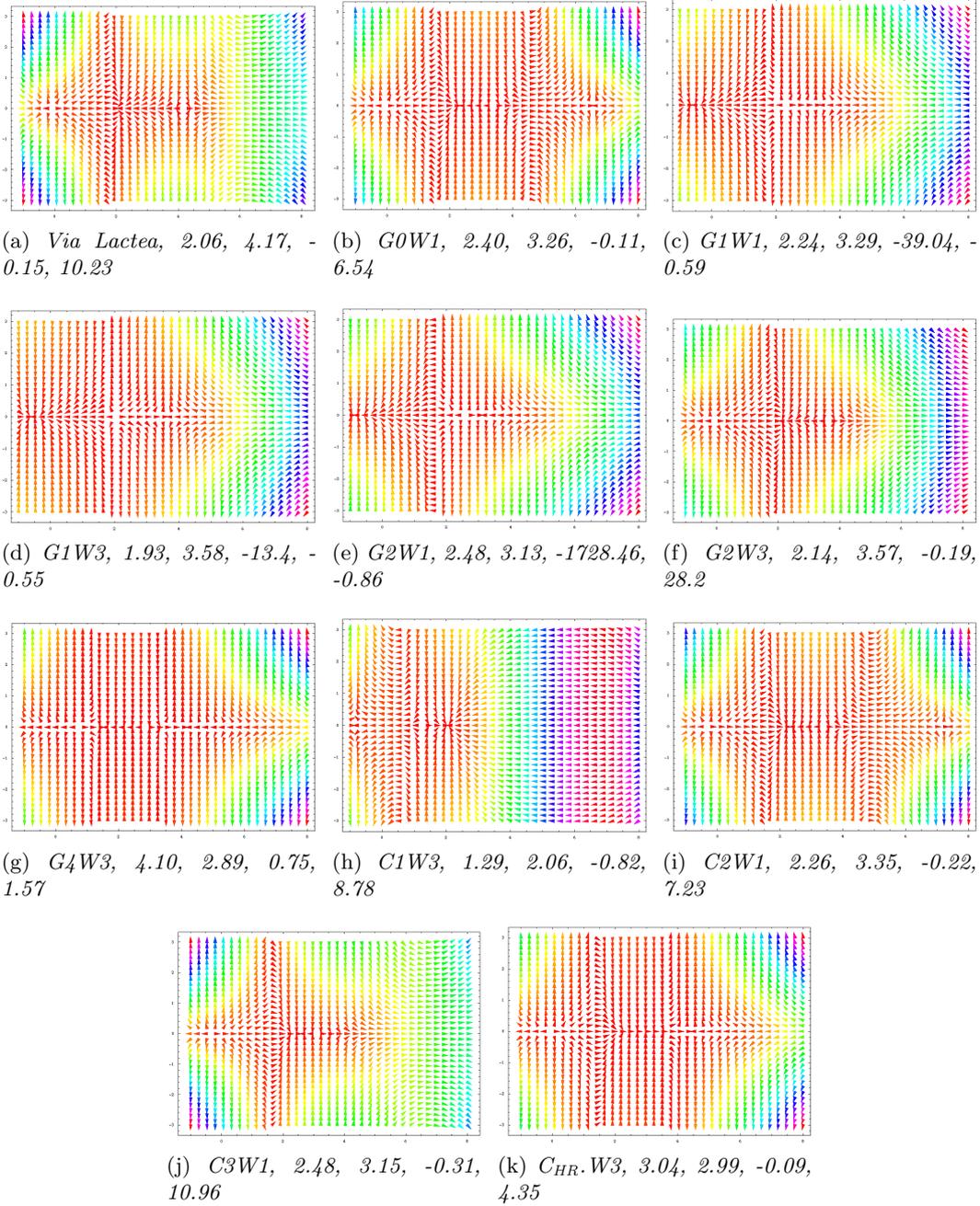
Figure E.2: Cut at $\gamma'' = 0$ in the 3D flow diagrams appearing when plotting Eq. (3.19). The values from Table 3.3 are used to calculate the 4 γs. The caption to each plot shows: Simulation name, γ_1, γ_3, γ_- and γ_+. The x-axis is γ in the range[-1,8] and the y-axis is γ' in the range [-3,3]. The optimized values of G3.W1 implied complex $\gamma_\pm$ and its flow is therefore not plotted above.

(a) *Via Lactea, 2.06, 4.17, -0.15, 10.23*

(b) *G0W1, 2.40, 3.26, -0.11, 6.54*

(c) *G1W1, 2.24, 3.29, -39.04, -0.59*

(d) *G1W3, 1.93, 3.58, -13.4, -0.55*

(e) *G2W1, 2.48, 3.13, -1728.46, -0.86*

(f) *G2W3, 2.14, 3.57, -0.19, 28.2*

(g) *G4W3, 4.10, 2.89, 0.75, 1.57*

(h) *C1W3, 1.29, 2.06, -0.82, 8.78*

(i) *C2W1, 2.26, 3.35, -0.22, 7.23*

(j) *C3W1, 2.48, 3.15, -0.31, 10.96*

(k) *$C_{HR}.W3$, 3.04, 2.99, -0.09, 4.35*
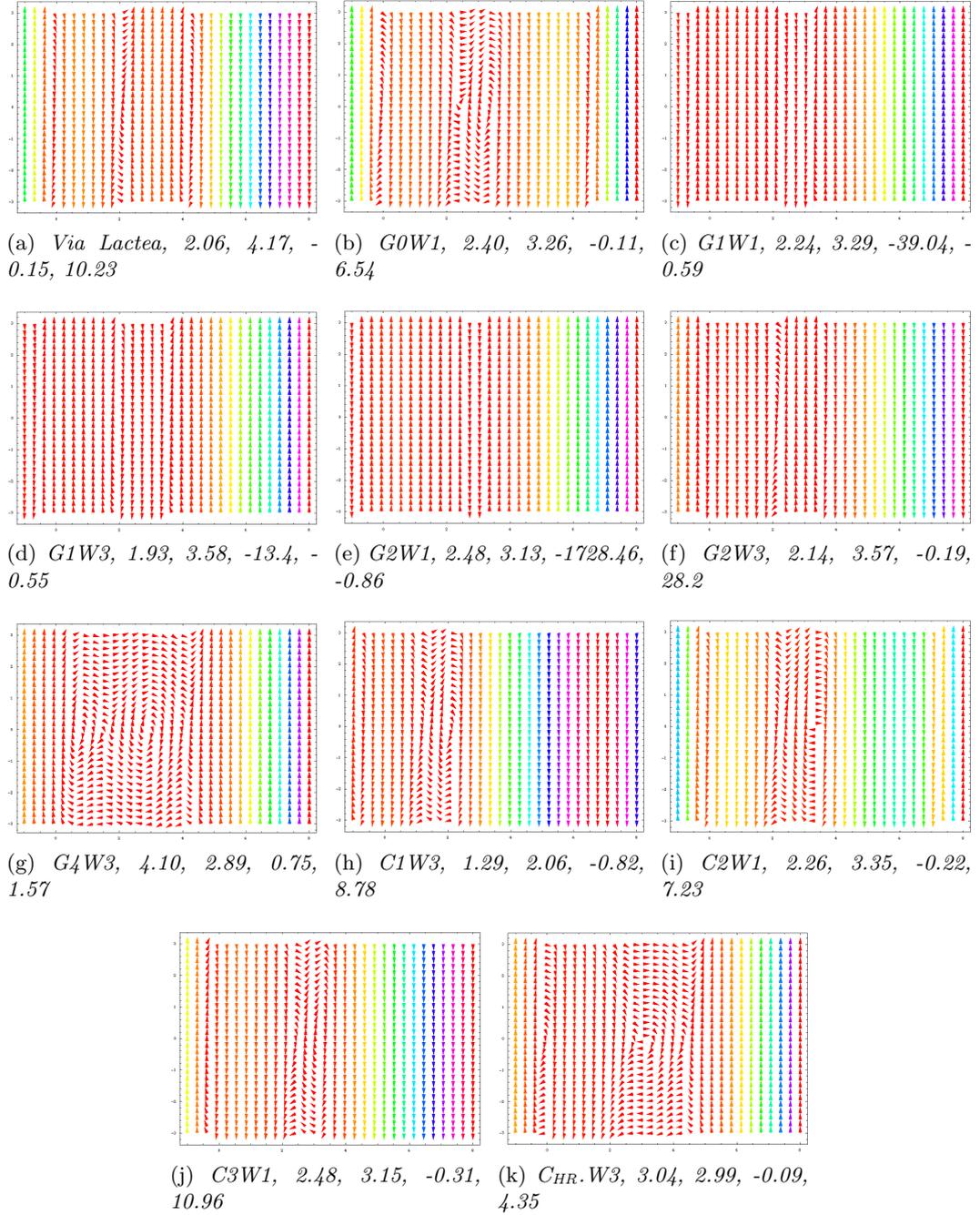
Figure E.3: Cut at $\gamma'' = 0$ in the 3D flow diagrams appearing when plotting only the convergences of Eq. (3.19). The values from Table 3.3 are used to calculate the 4 γs. The caption to each plot shows: Simulation name, γ_1, γ_3, γ_- and γ_+. The x-axis is γ in the range[-1,8] and the y-axis is γ' in the range [-3,3]. The optimized values of G3.W1 implied complex $\gamma_\pm$ and its flow is therefore not plotted above.

(a) $\gamma'' = 0.0$

(b) $\gamma'' = 0.1$

(c) $\gamma'' = -0.1$

(d) $\gamma'' = 0.5$

(e) $\gamma'' = -0.5$

(f) $\gamma'' = 1.0$

(g) $\gamma'' = -1.0$
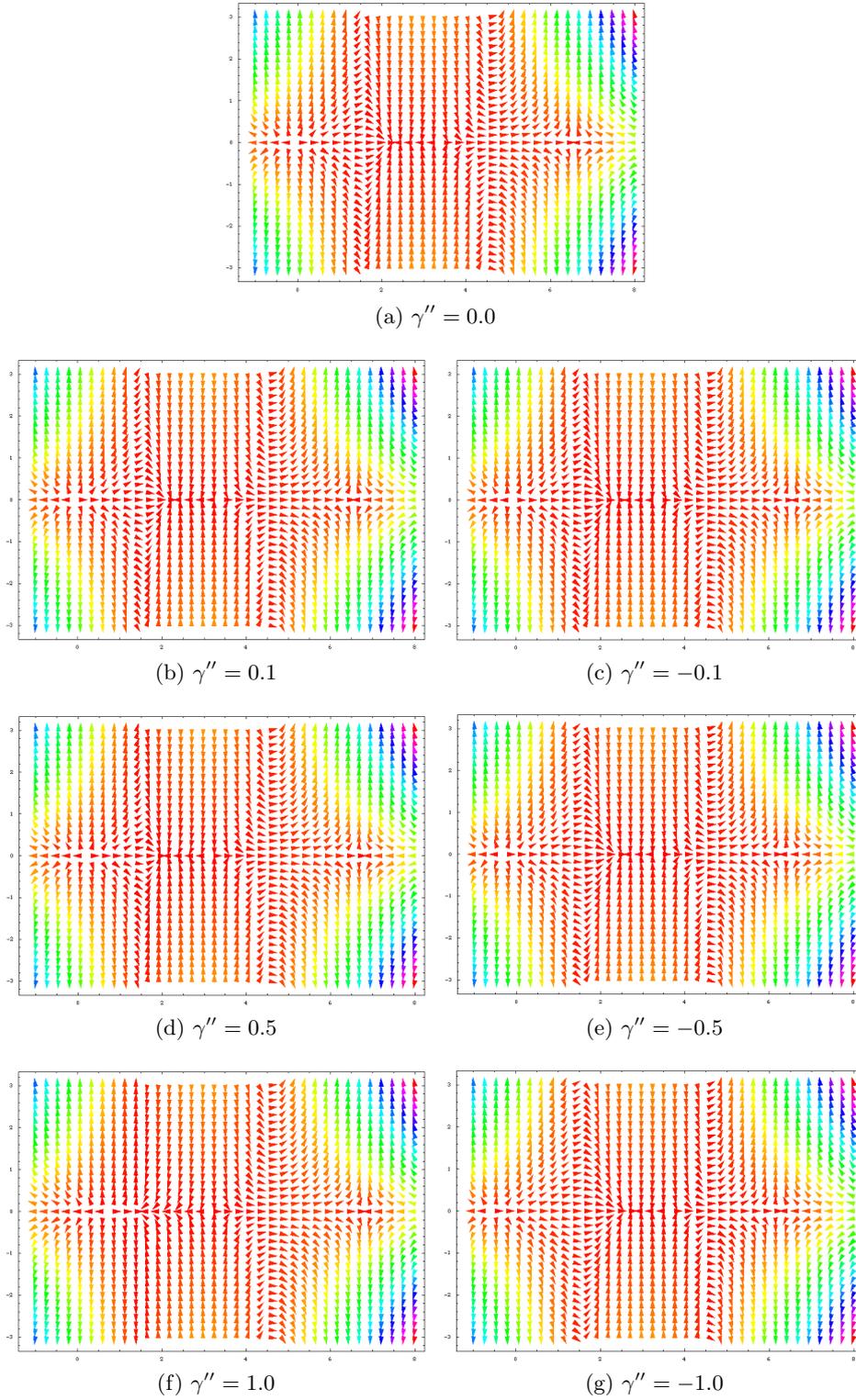
Figure E.4: Cuts for the structure G0.W1 in the 3D flow of Eq. (3.19) (shown in Fig. 3.19a) for different values of γ''. It is clear that the change in the γ'' direction is minimal, as claimed in the text.

(a) $\beta_0 = 0.8$ and $\alpha = 2.16$ (b) $\beta_0 = 0.8$ and $\alpha = 1.76$ (c) $\beta_0 = 0.8$ and $\alpha = 1.15$

(d) $\beta_0 = 0.1$ and $\alpha = 1.96$ (e) $\beta_0 = 0.1$ and $\alpha = 1.92$ (f) $\beta_0 = 0.1$ and $\alpha = 1.54$

(g) $\beta_0 = 0.0$ and $\alpha = 1.93$ (h) $\beta_0 = 0.0$ and $\alpha = 1.94$ (i) $\beta_0 = 0.0$ and $\alpha = 1.59$

(j) $\beta_0 = -0.1$ and $\alpha = 1.90$ (k) $\beta_0 = -0.1$ and $\alpha = 1.96$ (l) $\beta_0 = -0.1$ and $\alpha = 1.65$

(m) $\beta_0 = -0.8$ and $\alpha = 1.70$ (n) $\beta_0 = -0.8$ and $\alpha = 2.12$ (o) $\beta_0 = -0.8$ and $\alpha = 2.03$
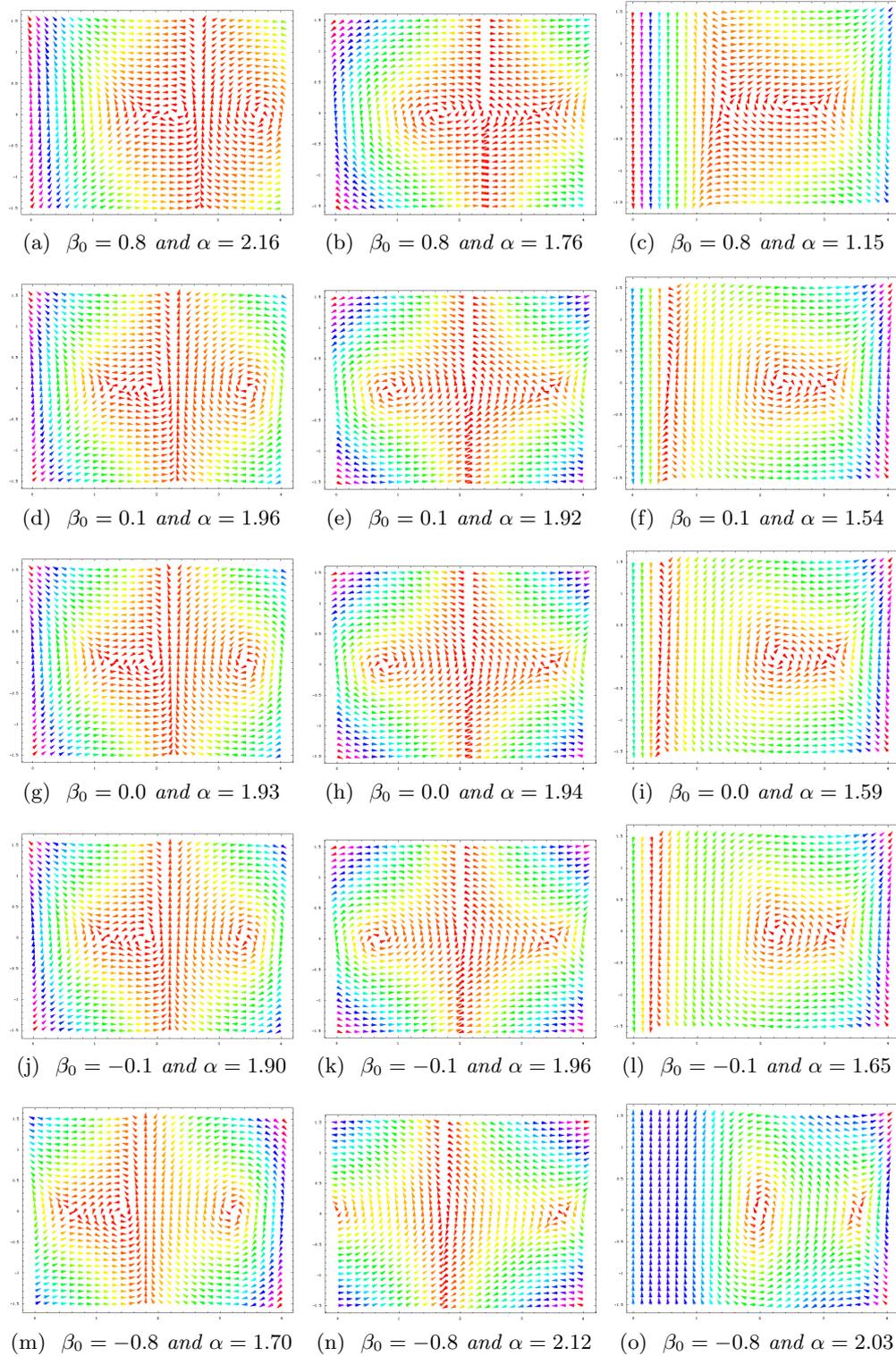
Figure E.5: Flow diagrams for DM05 Eq. (27). Left, center and right columns correspond to $\epsilon = 1$, 3 and 5. X-axes are γ in the range [0,4] and y-axes are γ' in the range [-1.5,1.5].

(a) $\beta_0 = 0.8$ and $\alpha = 2.16$ (b) $\beta_0 = 0.8$ and $\alpha = 1.76$ (c) $\beta_0 = 0.8$ and $\alpha = 1.15$

(d) $\beta_0 = 0.1$ and $\alpha = 1.96$ (e) $\beta_0 = 0.1$ and $\alpha = 1.92$ (f) $\beta_0 = 0.1$ and $\alpha = 1.54$

(g) $\beta_0 = 0.0$ and $\alpha = 1.93$ (h) $\beta_0 = 0.0$ and $\alpha = 1.94$ (i) $\beta_0 = 0.0$ and $\alpha = 1.59$

(j) $\beta_0 = -0.1$ and $\alpha = 1.90$ (k) $\beta_0 = -0.1$ and $\alpha = 1.96$ (l) $\beta_0 = -0.1$ and $\alpha = 1.65$

(m) $\beta_0 = -0.8$ and $\alpha = 1.70$ (n) $\beta_0 = -0.8$ and $\alpha = 2.12$ (o) $\beta_0 = -0.8$ and $\alpha = 2.03$
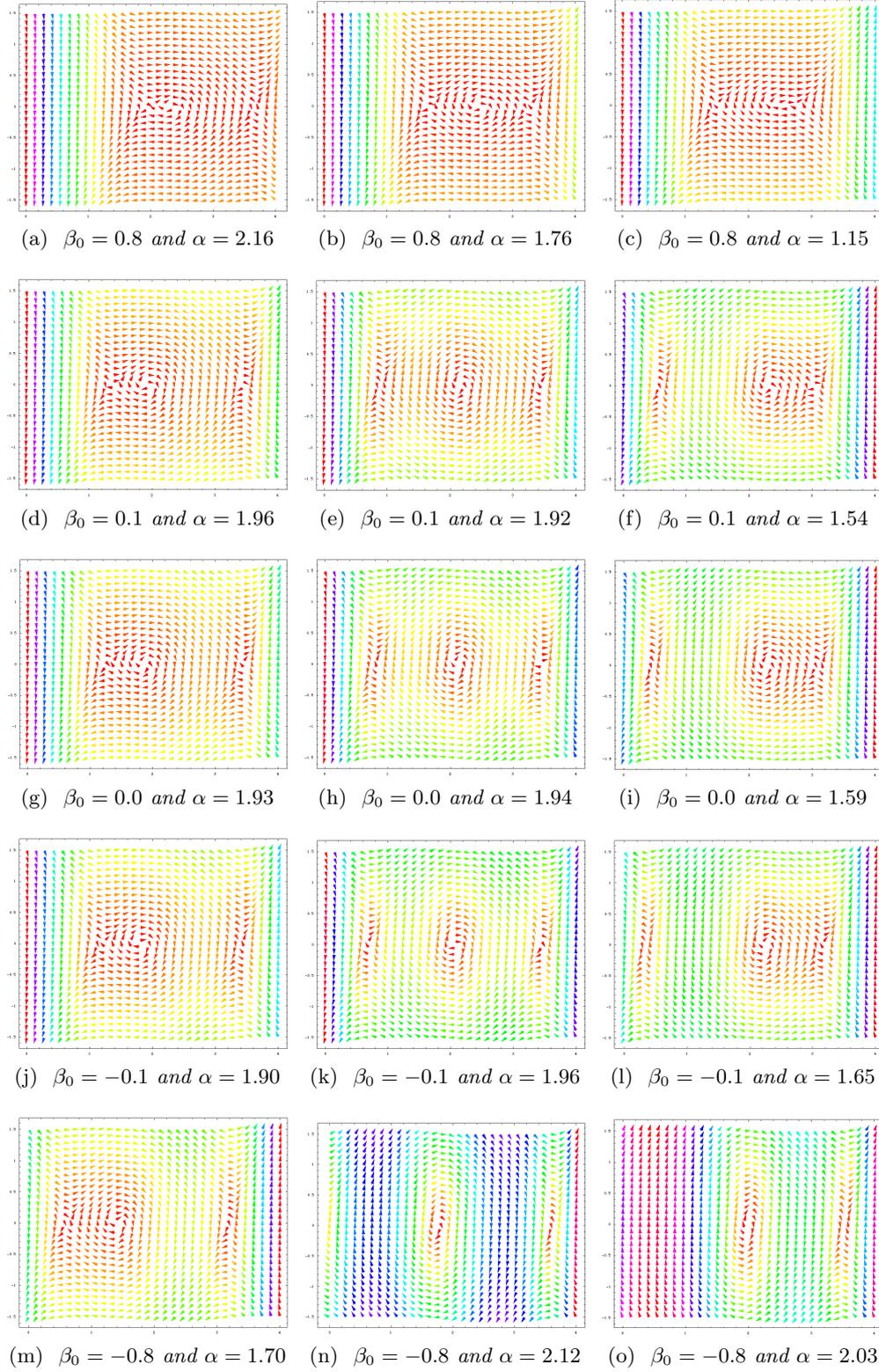
Figure E.6: Flow diagrams for the convergence values of DM05 Eq. (27). Left, center and right columns correspond to $\epsilon = 1$, 3 and 5. X-axes are γ in the range[0,4] and y-axes are γ' in the range [-1.5,1.5].

References

Allgood, B., Flores, R. A., Primack, J. R., Kravtsov, A. V., Wechsler, R. H., Faltenbacher, A., & Bullock, J. S., 2006, MNRAS, 367, 1781

Altay, G., Colberg, J. M., & Croft, R. A. C., 2006, MNRAS, 370, 1422

Ascasibar, Y., Gottlöber, S., 2008, ArXiv Astrophysics e-prints, arXiv:astro-ph/0802.4348

Austin C. G. et al. 2005, ApJ, 634, 756

Bertschinger, E., 2001, ApJ, 137, 1

Binney, J., & Tremaine, S. 1987, Princeton, NJ, Princeton University Press, 1987, 747 p.

Bullock J. S., Dekel A., Kolatt T. S., Kravtsov A. V., Klypin A. A., Porciani C., & Primack J. R. 2001, ApJ, 555, 240

Dehnen W and McLaughlin D, 2005 MNRAS, 363, 1057, ——— DM05

Diemand, J., Kuhlen, M., & Madau, P. 2007, ApJ, 657, 262

Diemand, J., Kuhlen, M., & Madau, P. 2007, ApJ, 667, 859

D'Onghia E. and Navarro J. F., 2007 MNRAS, 380, L58

Doroshkevich, A. G. 1970, Astrophysics, 6, 320

González-Casado, G., Salvador-Solé, E., Manrique, A., & Hansen, S. H. 2007, ArXiv Astrophysics e-prints, arXiv:astro-ph/0702368

Graham, A. W., Merritt, D., Moore, B., Diemand, J., & Terzić, B. 2006, AJ, 132, 2701

Hansen S. H. & Moore B, 2006, New Astronomy 11, 333-338 New Astron., 11, 333

Hansen, S. H., Moore, B., Zemp, M., & Stadel, J. 2006, Journal of Cosmology and Astro-Particle Physics, 1, 14

Hansen, S. H., Sommer-Larsen, J., 2006, ApJ, 653, L17-L20

Hansen, S. H., & Stadel, J. 2006, Journal of Cosmology and Astro-Particle Physics, 5, 14

Hansen S. H., 2004 MNRAS, 352, L41

Hansen, S. H. 2003, ArXiv Astrophysics e-prints, arXiv:astro-ph/0310149v1

Henriksen, R. N. 2007, ArXiv Astrophysics e-prints, 709, arXiv:0709.0434

Hernquist, L. 1990, ApJ, 356, 359

Højsgaard Mads, Gregersen K, Krogstrup P, 2007, Bacehlor thesis, University of Copenhagen

Kolb, E. W., & Turner, M. S. 1994, The Early Universe (Frontiers in Physics, Paperback edition), Perseus Books, Westview Press

Lee, J., Jing, Y. P., & Suto, Y., 2005, ApJ, 632, 706

Longair, M. S. 1998, Galaxy formation, New York : Springer, 1998. (Astronomy and astrophysics library)

Macciò, A. V., Dutton, A. A., van den Bosch, F. C., Moore, B., Potter, D. & Stadel, J., 2007, MNRAS, 378, 55

Maller A. H., Dekel A. and Somerville R., 2002, MNRAS, 329, 423

Manrique A., Raig A., Salvador-Solé E., Sanchis T., & Solanes J. M. 2003, ApJ, 593, 26

Markevitch, M., Gonzalez, A. H., Clowe, D., Vikhlinin, A., Forman, W., Jones, C., Murray, S., & Tucker, W., 2004, ApJ, 606, 819

Merritt, D., Graham, A. W., Moore, B., Diemand, J., & Terzić, B. 2006, AJ, 132, 2685

Metropolis, N., Rosenbluth, A. W., Rosenbluth, M. N., Teller, E., & Teller, E., 1953, J. Chem. Phys., 21, 1087

Moore, B., Quinn, T., Governato, F., Stadel, J., & Lake, G., 1999, MNRAS, 310, 1147

Moore, B., Governato, F., Quinn, T., Stadel, J. & Lake G. 1998 ApJ, 499, 5

Navarro, J. F., Frenk, C. S., & White, S. D. M. 1997, ApJ, 490, 493

Navarro, J. F., Frenk, C. S., & White, S. D. M. 1996, ApJ, 462, 563

Peebles, P. J. E. 1969, ApJ, 155, 393

Press, W. H., Teukolsky, S. A., Vetterling, W. T., & Flannery, B. P., 1992, Numerical Recipes in Fortran 77, Second Edition, The Art of Scientific Computing, Cambridge University Press

Randall, S. W., Markevitch, M., Clowe, D., Gonzalez, A. H., & Brada c, M., 2008, ApJ, 679, 1173

Salvador-Solé E., Solanes J. M., & Manrique A. 1998, ApJ, 499, 542

Salvador-Solé E., Manrique A., González-Casado G., & Hansen, S. H. 2007, ApJ, 666, 181

Schmidt, K. B., Hansen, S. H., An, J. H., Williams, L. L. R., & Macciò, A. V., 2008, submitted to ApJ

Sommer-Larsen, J., Götz, M., & Portinari, L., 2003, ApJ, 596, 46

Sommer-Larsen, J., 2006, ApJ, 644, L1-L4

Stadel, J. G., 2001, Thesis (PhD), University of Washington

Taylor J E & Navarro J F, 2001 ApJ, 563, 483

Vitvitska M., Klypin A. A., Kravtsov A. V., Wechsler R. H., Primack J. R., & Bullock J. S., 2002, ApJ, 499, 542

Wojtak, R., Lokas, E. L., Mamon, G. A., Gottlöber, S., Klypin, A., & Yehuda Hoffman, 2008, ArXiv Astrophysics e-prints, arXiv:astro-ph/0802.0429